Phosphor Coated UV-Responsive CCD Image Sensors

by

Stefan J. Alexander

A thesis

presented to the University of Waterloo

in fulfillment of the

thesis requirement for the degree of

Master of Applied Science

in

Electrical and Computer Engineering

Waterloo, Ontario, 2002

I hereby declare that I am the sole author of this thesis. This is a true copy of the thesis, including any required final revisions, as accepted by my examiners.

I understand that my thesis may be made electronically available to the public.

Stefan J. Alexander

Abstract

Typical CCD image sensors are not sensitive to Ultra-Violet (UV) radiation, because the UV photons have a penetration depth of 2nm in the ~1μm thick polysilicon gate material.

An inorganic phosphor coating was developed previously (by Wendy Franks et al [1, 2]) that was shown to be a viable solution to creating a UV-sensitive CCD image sensor. The coating absorbs incident UV radiation (250nm) and re-emits it in the visible (550-611nm) where it can penetrate the gate material. This coating was deposited using a settle-coat type deposition.

Improved coating techniques are presented here. These include a commercial coating from Applied Scintillation Technologies (AST), a Doctor-Blade coating, e-beam deposition, and laser ablation.

The properties of the coating, and of the coated sensors are presented here. Tests performed on the sensors include Quantum Efficiency, Photo-Response Non-Uniformity, Contrast Transfer Function, and Lifetime.

The AST coating is a viable method for commercial UV-responsive CCD image sensors. The Doctor-Blade coatings show promise, but issues with clustering of the coating need to be resolved before the sensors can be used commercially. E-beam deposition and laser ablation need further research to provide a viable coating.

Acknowledgements

To my supervisor, Dr. Arokia Nathan, for trusting me to take this research in whatever direction I wanted, and always finding a way to take care of everything that came up, no matter how big or how small.

To those at DALSA: Most importantly Dr. Martin Kiik, my DALSA supervisor, for dealing with the myriad day-to-day questions and problems as calmly and effectively as the major roadblocks that arose. To Bob Sabilla for helping me to locate nearly every piece of equipment in the lab, and working in the dark for hours on end as I was making measurements in his lab. And to Larry Kruse for the procurement and protection of desirable equipment.

To my parents, for giving me the ability, encouragement and desire to pursue what I wanted.

And last, but most importantly, to my wife Michelle, for giving me all the time I needed to work on this, and putting up with all the setbacks and delays. And my children, Jacob and Charlotte, for putting up with me and providing a purpose for much-needed breaks.

Stefan J. Alexander

Waterloo, ON

Table of Contents

List of Figures

List of Tables

1 Introduction

The light-sensitive part of most digital cameras is a CCD image sensor. Typical CCD image sensors are insensitive to Ultra-Violet (UV) radiation, 10 to 400nm, since the photons get absorbed in the gate material. The absorption depth of UV radiation in the polysilicon gate material is 2nm, whereas the typical gate thickness is 1000nm. This is shown in Figure 1.

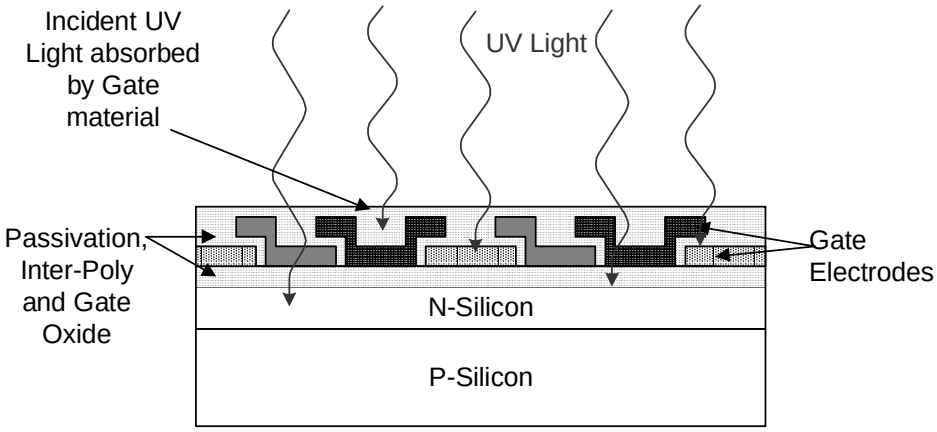

Figure 1 - Diagram of incident UV light absorbed in the polysilicon gate material of an uncoated CCD image sensor (Adapted from [2])

While digital cameras for consumers have little use for UV sensitivity, there are many uses for UV imaging in industry and manufacturing, described in the following section. This is driving the continual development of methods to make CCD image sensor sensitive to UV.

1.1 Motivation

There is a need for UV-sensitive CCDs for applications such as monitoring of UV lithography, monitoring of flames that emit UV light, UV spectroscopy, and stress inspection.

Present UV sensors use either a structural modification, or an external coating. Some structural modifications include back-side thinned devices, replacing the polysilicon with ITO, and using photodiodes instead of photogates [26, 27, 28].

Back-side thinning involves etching the backside of the wafer to reduce its thickness. A thin film is deposited to repel photo-generated charge towards the top of the device, and an anti-reflection coating is deposited to improve Quantum Efficiency. The QE can be as high as 90% at 254nm. Out of all the methods, backside-thinned devices exhibit the highest responsivity, but are very expensive solutions.

The polysilicon gate material can also be replaced with Indium-Tin Oxide (ITO), a transparent conductor. The efficiency can be slightly improved (20% at 265nm) [29, 30]. However, ITO gated sensors are also a very complicated, expensive solution.

Photodiodes are more responsive to UV, however the photodiode requires an extra transistor per pixel to read out the signal. This is acceptable for line-scan sensors where the transistor can be positioned above or below the array. With area array devices, this extra transistor would reduce the fill factor.

A less expensive, less complicated approach to create an inexpensive UV-sensitive CCD is to coat the sensor with a UV phosphor which will absorb the UV and emit visible light which can penetrate the gate material [31, 32, 33, 34, 35, 36], as shown in Figure 2.

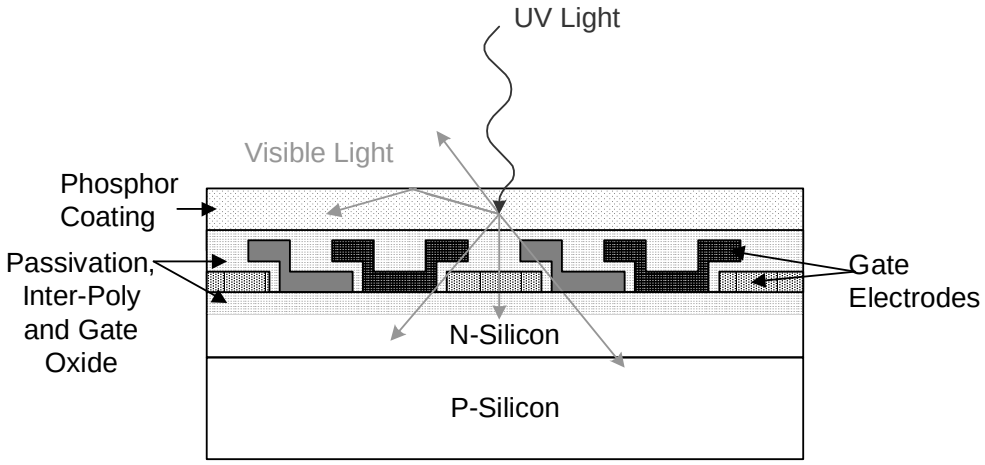

Figure 2 - Diagram of incident UV light incident on a phosphor-coated CCD image sensor (Adapted from [2])

In this situation, the UV photons get absorbed by the phosphor coating. The phosphor down-converts the UV photons to visible photons, and isotropically re-emits them. The visible photons can more easily penetrate the gate material, and therefore generate a signal from the sensor.

For area array devices, phosphor coatings look promising for a low-cost UV solution. This also has an advantage over structural modifications, because the coating can be applied to a wide range of previously tested sensors.

Existing UV phosphor coatings for CCD image sensors are mostly organic coatings, such as Metachrome II. These are deposited in a vacuum, and while it can increase the QE in the UV to up to 25%, their stability is poor. According to the datasheet, they can last up to 2 years, but the coating must be in a vacuum and cooled to -40ºC [19].

Inorganic phosphors are much more stable than organic ones. A typical application is the phosphor in fluorescent lights. Their efficiency is stable for up to 55,000 hours [39].

1.2 Settle Coating

A coating using inorganic phosphors was first demonstrated using simple settling technique by Franks et al. [1, 2], who demonstrated a QE of 12% at 265nm, a 3.5x improvement over the uncoated sensor. A suspension was formed with plastic, phosphor and solvent. The plastic must be transmissive in the UV, and the index of refraction must be less than the index of refraction of the top passivation layer of sensor to get high optical coupling that will reduce internal reflections. The solvent should be volatile, so it evaporates completely away. In this case, toluene was used. The sensor was placed in the suspension, and the suspension was allowed to evaporate, depositing a coating of plastic and phosphor onto the sensor.

The best results obtained with a settle coating deposition are shown in Figure 3. Osram Sylvania 2212 phosphor was used in this experiment. The details of the phosphor are explained in Chapter 2.

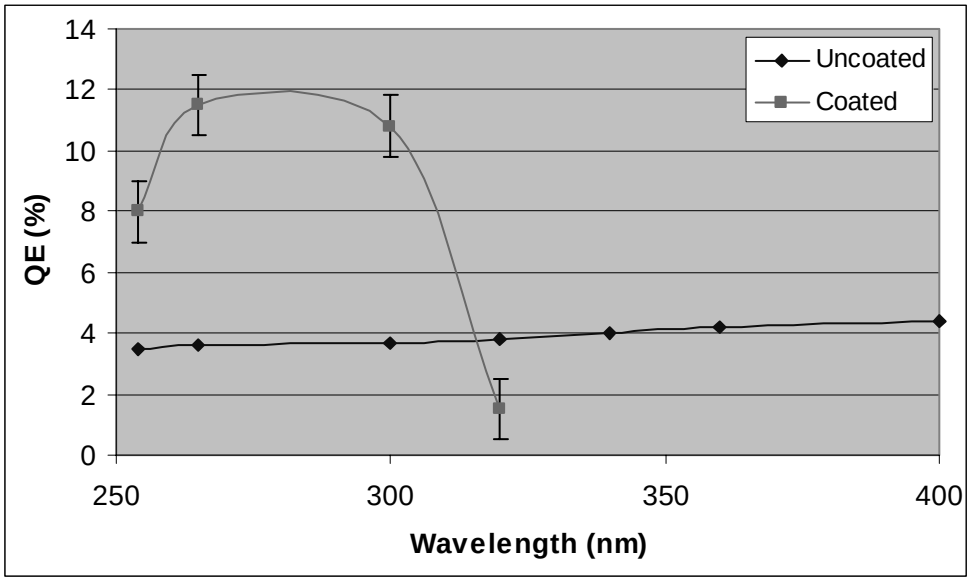

Figure 3 – Quantum Efficiency Spectrum of DALSA IA-D1-0256 Sensor coated with Osram Sylvania 2212 Phosphor using the Settle-Coat Method

The QE of the coated sensor peaks at 265nm, then gets lower as the phosphor is less responsive at longer wavelengths. Once the phosphor is no longer converting the UV photons, it actually interferes with the normal absorption, and the QE goes below that of the uncoated sensor. The PRNU results, only tested at 254nm, show a minimum degradation of 160%.

The work presented in this thesis builds on the settle-coat technique. More advanced processing techniques are used, and the coatings are examined in more detail to provide greater insight into what affects the performance of the coatings. The tests on the sensor have been expanded to provide a clearer picture of their performance. A numerical simulation using MATLAB was also developed, and is presented here. The simulation aids in determining how the properties of the coating will affect the properties of the sensor.

2 Phosphors

2.1 Phosphor Criteria

Phosphors work by absorbing photons of one energy, and emitting them at a different energy. There are various properties that describe how this happens, and these properties will be used to select the optimal phosphor for this application.

The phosphor conversion efficiency is defined simply as the percentage of absorbed photons that are subsequently re-emitted. Since this is a theoretical limit, many phosphors are rated to have a 100% conversion efficiency. However due to imperfections, impurities, re-absorption and reflection, this is often much lower once the phosphor is incorporated into a coating. As well, some of the deposition techniques may damage the phosphor, reducing the conversion efficiency. These effects are examined in more detail in the chapters dealing with the coating techniques.

The **e**xcitation peak is the relationship of conversion efficiency to wavelength. This is where the conversion efficiency is a maximum. The target wavelength for this application is 250nm UV, so we will want the excitation peak to be as close to that as possible.

There is also an emission spectrum for each phosphor, showing the relative number of photons that are emitted at each wavelength. Again, the quoted emission peak is usually the peak value of the emission spectrum. Ideally, the emission peak should match the peak responsivity of the CCD.

The absorption and emission spectra of the phosphor should remain unchanged during deposition. Electrical devices must be specifically calibrated to emit or absorb the correct wavelength of light, so the spectrum of the

phosphor must be preserved. If it must be changed, then it must be a characterisable and repeatable change, so that the device can be designed for the new spectrum. However, since the target here is to coat devices without requiring structural modification, the deposition method should leave this as unchanged as possible.

The decay time is the time for the emission of the phosphor to decrease to a certain value of its maximum, it can be rated as time to 1% or time to 1/e. Lag will result if the decay time is slower than the sensor integration time.

Photostability (or lifetime) is how the efficiency changes over time and with exposure to light. We wanted an extremely long lifetime, since it is planned to deposit the phosphor directly on the sensor. Short lifetime would therefore result in frequent replacement of the sensor. Many inorganic phosphors will start out at 100% QE, then drop rapidly to 50% within a few hours, where they can stay stable for hundreds or thousands of hours. Other phosphors may have a continuous linear or exponential drop until they reach zero conversion efficiency. This is a very important property to consider during phosphor selection, but equally important to note how it is changed during deposition. Techniques such as laser ablation expose the phosphor to extremely high light levels, which may be the equivalent of hundreds of hours of normal use.

Organic phosphors are made of ring-shaped molecules, and can be evaporated and re-grown without much loss in their conversion efficiency. These are commonly used as laser dyes. Unfortunately, they usually have poor lifetimes, and they must usually be deposited in a vacuum. Most phosphor-coated UV image sensors have been made with organic phosphors. Inorganic phosphors are often made of rare earth oxides with an activator (an element such as Yttrium of Europium). They are often used as lamp phosphors. They come in crystals of various shapes, as shown in Figure 4, and the crystals are

typically in the 1-50 micron range. Although deposition is harder because the crystals cannot be altered, the lifetime is extremely long (up to 55,000 hours [39]).

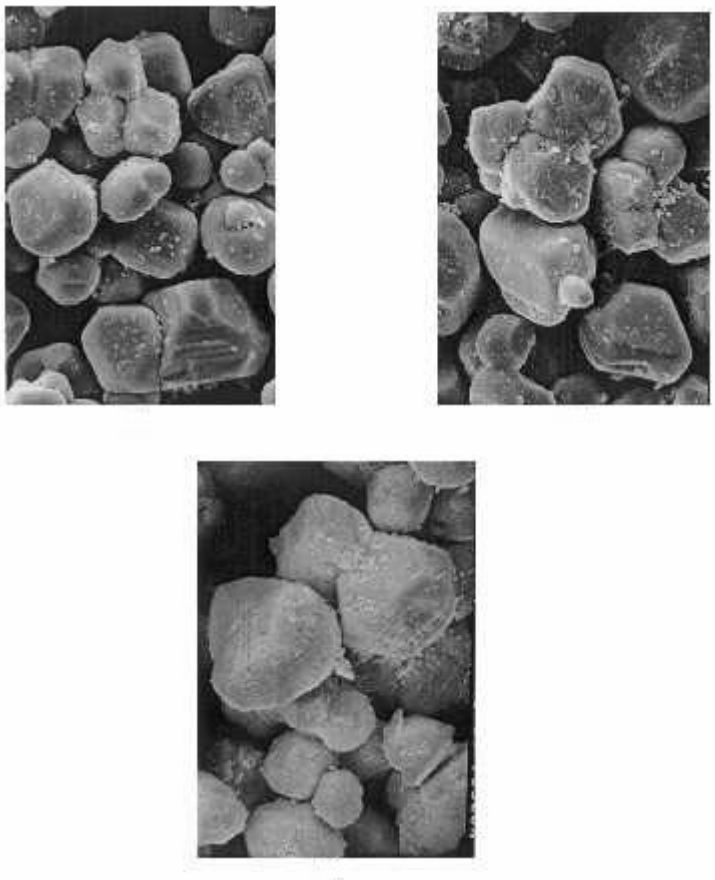

Figure 4 - SEM photographs of Yttrium Oxide Inorganic Phosphor Crystals [11]

These crystals cannot be melted or evaporated; if their structure is changed at all they will cease to function. Hence the deposition techniques must preserve the structure of the crystal, which limits what one can do with them. If their structure is destroyed, it would be necessary to re-activate them. The process for this depends on the phosphor. When the phosphor is made, elements are crystallized in a certain pressure, temperature, and ambient

environment. The phosphor would have to be re-crystallized in exactly the same environment, for it to still be active.

2.2 Phosphor Selection

In earlier work by Franks et. al. [1, 2] two inorganic phosphors from Osram Sylvania were chosen because of their high efficiency, their absorption peak at 265nm, and their short decay time (which must be much shorter than the integration time of the sensor) [40, 41]. The 2212 phosphor has maximum absorption from 200 nm to 280 nm, and an emission peak at 544 nm. The 2345 phosphor has an absorption peak at 225 nm and an emission peak at 611 nm. The main requirements which made most phosphors ineligible was long decay time – it had to be an extremely "fast" phosphor so that it would emit photons only during the frame when it absorbed them – otherwise lag would result. Table 1 shows the criteria from the datasheet.

Table 1 - Comparison of properties of Osram Sylvania type 2212 and 2345 phosphors [40,41]

	Osram Sylvania 2212	Osram Sylvania 2345
Chemical Formula	(LaCeTb)PO_4:Ce,Tb	Y_2O_2:Eu
Conversion Efficiency (%)	86% at 254nm	100% at 254nm
Decay Time	1ms to 1/e	1ms to 1/e
Typical Use	Lamp Phosphor	Lamp Phosphor
Peak λExcitation (nm)	254	254
Peak λEmission (nm)	546	611
Average Particle Size (μm)	6	4.2

The conversion efficiency was different for each wavelength, but numerical measurements were only made at 254nm, which is the target wavelength for this phosphor.

Since the typical application for these phosphors is in fluorescent lamps, this means long lifetime, typically up to 55,000 hours. Most of decay happens after first 100 hours, and efficiencies are typically quoted after that time.

The Peak Emission wavelength for 2212 is in the green (550nm), and 2345 is in the red (611nm). The green emission is preferred, since the CCD is more responsive to this wavelength. The 2212 phosphor has a larger particle size, but as will be shown has a shape that is preferable for this type of coating.

3 Experimental Description

In order to determine the characteristics of each of the coating methods, some quantitative tests had to be developed. This would give a practical comparison among all the types of coatings. The tests that performed were Quantum Efficiency, Photo-Response Non-Uniformity, Contrast Transfer Function, and Lifetime.

3.1 Quantum Efficiency

The Quantum Efficiency is a measure of the sensitivity of the CCD to the incident radiation. It is calculated using the number of electrons *collected* per incident photon. This way we take into account reflection losses where photons don't even make it into the silicon, the conversion from photons to electrons, the change transfer efficiency, and the charge conversion efficiency, where the charge is converted to a potential.

Because the camera has internal gain, it is best to measure the QE right off the sensor. The sensor (DALSA IA-D1-0256) was placed into the camera (CA-D1-0256), but with the VOD pin lifted. The electrons collected by the image sensor are fed into a charge amp, where the current is read out. The VOD pin should be connected to -15V which will sweep away the charge at the input (gate) of the charge amp. So by examining the current through the VOD pin, the amount of charge collected by the sensor can be obtained. A 1 MΩ resistor was connected in series between -15V and the VOD pin. The voltage drop across this resistor, measured with a Keithley 2000 Multimeter can be used to calculate the Quantum Efficiency. In order for this to be accurate, though,

the sensor must be clocked in TDI mode. This means the charge packets must be transferred from one line to the next at a constant rate. As well, one must be careful not to let the sensor enter saturation, in which case charge packets will be lost and the Quantum Efficiency measurement will be artificially low.

The formula used for the photocurrent is:

$$J_{Photo} = \frac{V_{Photo} - V_{Dark}}{qRf_{Data}} \qquad \textbf{(Equation 1)}$$

Where V_{Photo} is the voltage drop across the resistor under illumination, V_{Dark} is the drop across the resistor under zero illumination, and f_{Data} is the data rate, the number of times per second that the lines of the CCD are read out. q is the charge of an electron, and R is the value of the resistor used in the measurement (in this case, 1 MΩ).

In order to determine the amount of photons incident on the sensor, an Oriel optical power meter was used. This meter was calibrated to the incident wavelength, and operates under the assumption that all the light incident upon the meter is of that wavelength. The light meter was put into the path of the incident light before each reading. The rate of photons incident on each pixel is calculated as:

$$I_{Incident} = \frac{PA_{Pixel}N}{E_{\lambda Inc}f_{Line}} \qquad \textbf{(Equation 2)}$$

Where P is the reading on the optical power meter, A_{Pixel} is the active area of each pixel, N is the number of rows in the active area of the sensor,

$E_{\lambda Inc}$ is the energy per photon (calculated for each wavelength), and f_{Line} is the line rate.

The final formula for the Quantum Efficiency is:

$$Quantum\_Efficiency = \frac{J_{Photo}}{I_{Incident}} \qquad \textbf{(Equation 3)}$$

To ensure the most accurate results, the voltage across the resistor was measured at 4 different light intensities, and the slope of J_{Photo} versus $I_{Incident}$ gives the final Quantum Efficiency.

The Quantum Efficiency was calculated at 254nm, 265nm, 300nm, 320nm, 340nm, and 365nm, for the uncoated sensors, and again after coating. The UV light source used was an arc lamp with a 200W Hg bulb from Oriel (PN 6283). The light was collimated and passed through a liquid IR filter. Mercury line filters and narrow band filters were used to create a narrow band spectrum. As well, a "Visible Block" filter was used to block out any longer-wavelength light (400-1000nm) that may have got through the filters.

3.2 Photo-Response Non-Uniformity

The previous test was concerned with the efficiency of the phosphor coating. In contrast, the photo-response non-uniformity (PRNU) is a measure of the quality of the phosphor coating. It is a measure of the pixel-to-pixel variations in responsivity. Under uniform illumination, not all pixels will have the same electrical output. An uncoated sensor will have a PRNU value due to process differences. The phosphor coating will further degrade the PRNU, due to

variations in coating thickness and phosphor density. The goal is to minimize this degradation.

In order to properly characterise the PRNU, every pixel was used in the calculation. Since the PRNU is a spatial characteristic, all temporal distortions should be removed. To do this, the DALSA IA-D1-0256 area array image sensor was put into a DALSA CA-D1 camera, and connected to a frame grabber to capture the video frames. This consisted of an array of 256x256 numbers, each representing the light intensity as an integer from 0 to 255. Using the video average feature in Image Pro Plus 1.3, 100 frames were captured and averaged. This removed the temporal error, due to variations in the lamp's intensity, and photon shot noise. Then, the average pixel brightness μ was obtained by averaging all pixels. Each pixel x_i was compared to the average pixel signal μ and using the formula shown below, the standard deviation was obtained.

$$\sigma^2 = \frac{1}{N}\sum (x_i - \mu)^2 \qquad \textbf{(Equation 4)}$$

The final PRNU was then calculated as the ratio of the standard deviation to the average pixel signal, as shown below.

$$PRNU = \frac{\sigma}{\mu} \times 100\% \qquad \textbf{(Equation 5)}$$

The PRNU test was performed at 3 wavelengths, 254nm, the absorption peak for the phosphor and the expected operating wavelength, 550nm, the emission peak for the 2212 phosphor, and 620nm, the emission peak for the 2345 phosphor. The same 200W HG Oriel lamp combined with narrow band

filters were used to generate the three wavelengths. These tests were conducted for each uncoated sensor, then repeated once the sensor was coated.

Since the coating absorbs the UV photons and re-emits them at longer wavelengths (540nm in the case of 2212 and 611nm in the case of 2345), it makes sense to compare the coated result at 254nm with the uncoated result at the wavelength of peak emission. These are the two values that are presented for each sensor. The difference can be considered the PRNU of the coating alone.

3.3 Contrast Transfer Function

Like the PRNU, the Contrast Transfer Function (CTF) is a measure of the quality of the coating. It is a measure of how accurately the sensor can reproduce square waves of increasing frequency [37, 38].

A test pattern, consisting of lines of different spatial frequency, was printed onto quartz slides by Applied Image, Inc.

Once projected and focused onto the sensor, the pattern looked like the one shown in Figure 5. Note this is with a phosphor coating, which adds a certain “grainyness” to the background.

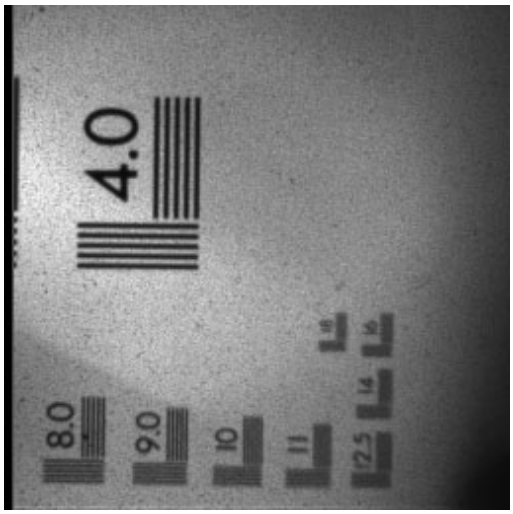

Figure 5 – Image capture of CTF Pattern, taken with IA-D1-0256 Sensor coated with 2212 phosphor, with 254nm incident light

Using a Nikkor UV lens with a focal length of 105mm, and the Oriel UV source mentioned previously, this image was projected onto the sensor before and after coating. The CCD camera was mounted on a 3-axis translational stage. This allowed for precision movement horizontally, vertically, and towards/away from the camera, for precise focus. A diagram of the experimental setup is shown in Figure 6.

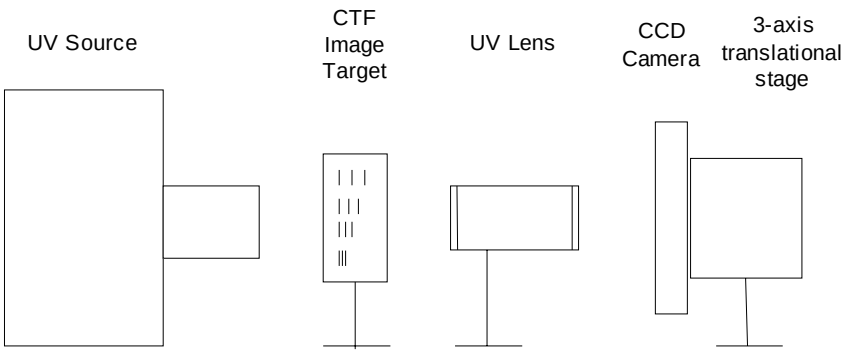

Figure 6 - Schematic Diagram of Experimental Setup for CTF test

The light was adjusted so that each pixel, if fully illuminated, would get half its saturation light intensity (a DN of 128). As with the PRNU test, the camera was connected to the frame grabber so that the images could be recorded electronically. The images were displayed and manipulated in Image Pro Plus version 1.3.

The UV lens and CCD camera were positioned to get the image approximately in focus. Using the micrometer, and looking at the test pattern focused on the screen, the focus was adjusted to make the image as clear as possible. Further, the digital numbers representing brightness were extracted and plotted in a line profile, as shown in Figure 7, Figure 8 and Figure 9. This allowed one to see the background brightness, the darkness of the lines, and the brightness of the spaces between the lines, plotted as a function of distance. The focus was adjusted until the peaks and valleys were at their maximum, then the horizontal translation was adjusted until the lines lined up with the pixels as much as possible. Figure 7 shows a partially aligned line profile. There are some definite peaks and valleys, but there is also a “smear” on the right side where one of the lines is overlapping two pixels almost completely evenly.

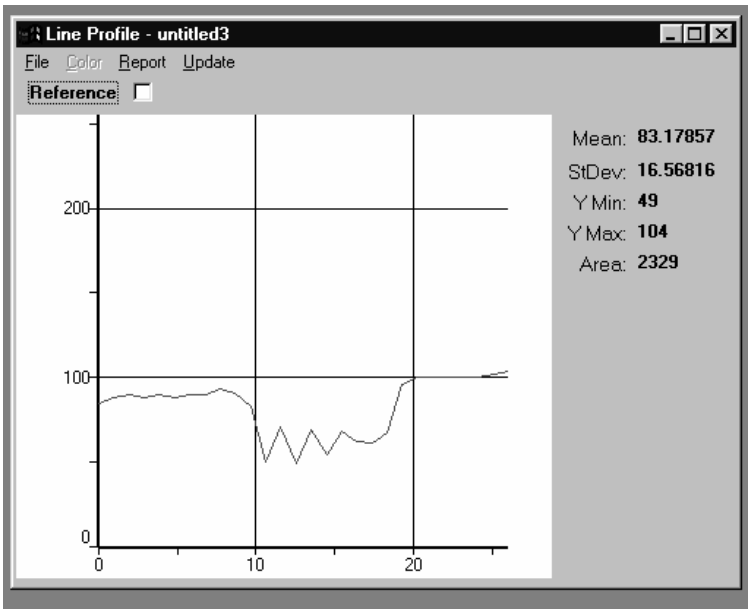

Figure 7 - Line profile of CTF pattern at 0.627 lines/pixel - Partially lined up

Figure 8 shows an even worse case; most of these pixels are overlapping, and it's evident that the one peak and valley that can be seen are not as large as they can be.

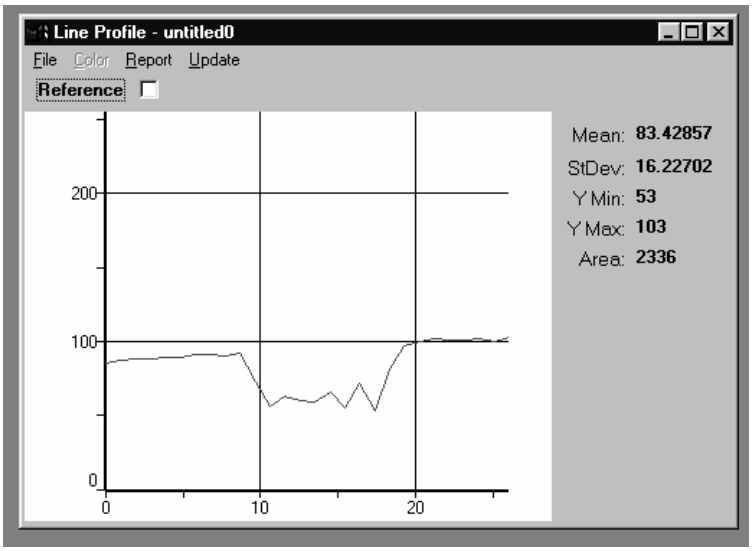

Figure 8 - Line profile of CTF pattern at 0.627 lines/pixel - Not lined up

Figure 9 shows a line profile that has been perfectly lined up, the peaks and valleys are as large as they can be, and the largest peak and valley are located in the middle.

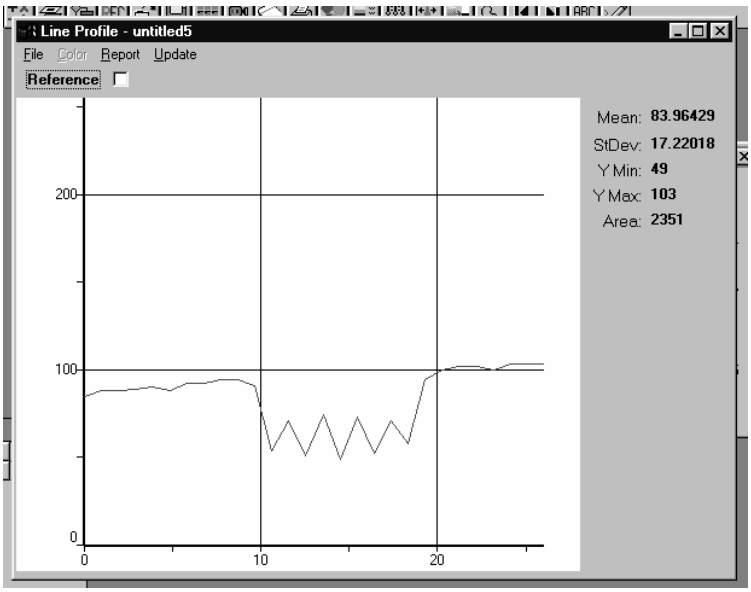

Figure 9 - Line profile of CTF pattern at 0.627 lines/pixel - Perfectly lined up

Figure 7, Figure 8 and Figure 9 show a typical problem with this test at higher spatial frequencies – except at multiples of the Nyquist frequency, the frequency of the lines did not match up with the frequency of the pixels. So even in a pattern that is lines up ideally, some peaks and valleys will be higher or lower than others.

The CTF test was repeated several times on the same uncoated sensor, each time resetting the location of all the equipment and moving it into its proper place. This way the error involved in the CTF test could be approximated. Initially, the error was found to be very large, as much as 30% in some situations. Through much experimentation, experimental techniques for performing this test were developed to vastly reduced the error.

In order to make the tests as accurate and consistent as possible, the horizontal micrometer would be adjusted so that the highest peak and lowest valley was located in the centre. For spatial frequencies above 0.5 lines/pixel (corresponding to "10" and higher on the image target), the highest peak and lowest valley were used for the CTF measurement. For spatial frequencies below 0.5 lines/pixel (corresponding to "9.0" and lower on the image target) all the peaks and valleys were visible, and the highest peak and lowest valley that were adjacent to each other were chosen.

Using these methods, it was found that the error was reduced to below 8%. This was found by repeatedly performing the same test on the same sensor, 20 times, each time re-setting all the equipment involved and aligning it again, including all the light levels. Since both the maximum AND minimum were involved in the final CTF measurement, each time a measurement was taken, the value (max-min) was calculated. Out of the 20 values, the highest and lowest values of (max-min) were recorded. The % error was calculated using the following formula, shown in Equation 6.

$$\%\_Error = \frac{(Max - Min)_{Highest} - (Max - Min)_{Lowest}}{Average\_Background\_Light\_Level} \times 100\% \qquad \textbf{(Equation 6)}$$

The formula was then plotted for each spatial frequency, as shown in Figure 10.

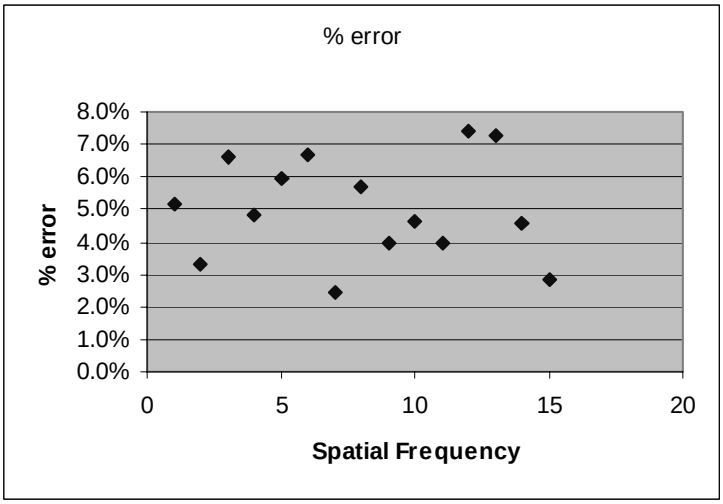

Figure 10 – Percent Error in CTF test, averaged over 20 tests of the same sensor for different spatial frequencies

Figure 10 shows that using the methods mentioned above, the error can be kept under 8%.

For performing the actual CTF test on each sensor, each pattern of lines (of different spatial frequency) was examined, the light intensity numbers were extracted, and put into Microsoft Excel, so that they could be analysed.

First, the minimum background light level was measured. The scattered light was measured by taking a measurement from a large black spot on the slide, that was projected onto the sensor. This gave a measure of the darkest that anything could be. This dark spot was over 50 pixels wide, so it can be assumed any signal is due entirely to scattered light. Then, for each set of lines, the background light level was measured, close to that area and where there were no lines, to give an indication of the brightest that it should be in that area. Then, the minimum valley and maximum peak were measured, using the rules set out above. The CTF was then calculated using:

$$CTF = \frac{(Highest\_Peak) - (Lowest\_Valley)}{(Background\_Light\_Level) - (Min\_Dark\_Level)} \quad \textbf{(Equation 7)}$$

A plot was then obtained for all spatial frequencies available on the test image. This was done for three different wavelengths; 254nm, the peak absorption of the phosphors and the expected use of the sensor, 550nm, the emission of the green phosphor, and 610nm, the emission of the red phosphor. The 200W Hg lamp from Oriel and narrow band filters used in all other tests were used to create the different wavelengths. In this way, a plot of the CTF was obtained. A sample is shown in Figure 11.

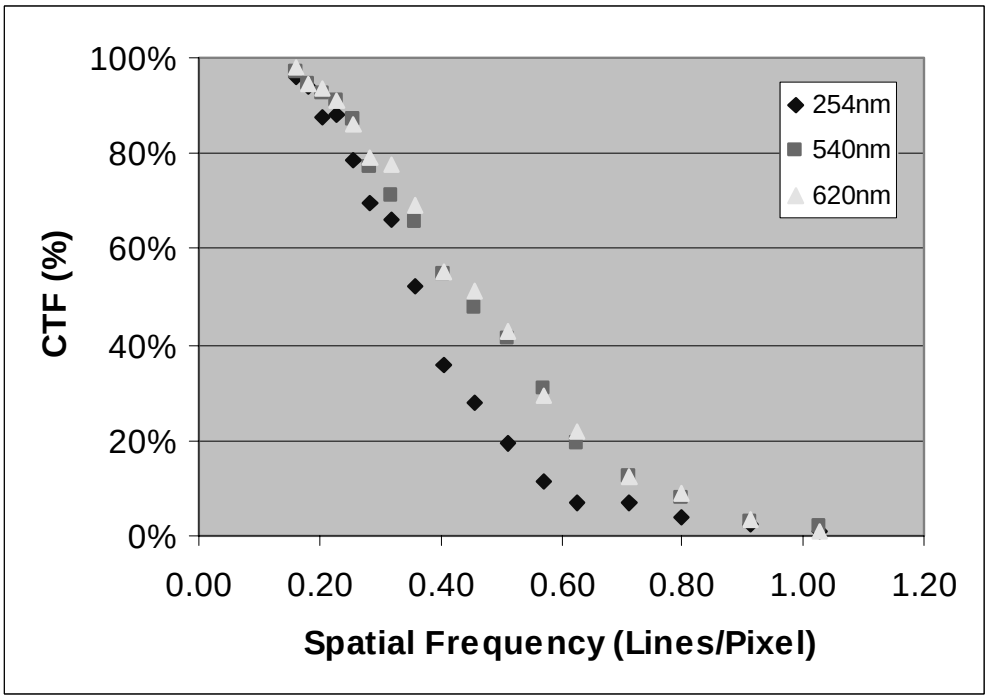

Figure 11 - Sample CTF Results, taken on an uncoated IA-D1-0256 Sensor with 254nm incident light

When the phosphor absorbs UV photons, it re-emits them at a longer wavelength. The peak emission is 540nm in the case of 2212 phosphor and

611nm in the case of 2345 phosphor. So it makes sense to compare the coated results at 254nm with the uncoated results at the peak emission wavelength. These are the two curves that are displayed for each sensor.

The Nyquist frequency is 1 Line/pixel, where the frequency of the lines matches up perfectly with the frequency of the pixels. The CTF curves are usually most different in the middle, so the CTF value at ½ Nyquist frequency is used as a single figure of merit for the CTF value, although the entire curves are displayed.

3.4 Lifetime

Having examined the efficiency and the quality of the coating, this test examines the stability of the coating when exposed to large amounts of UV photons. Most inorganic phosphor materials degrade to about half of their conversion efficiency after about 100 hours of use, after which they are stable for up to 55,000 hours. However, when these phosphors are used in an actual coating, with binders, impurities, a different surface and far different lighting conditions than in a fluorescent lamp, average stability data for the coating cannot be extracted from that of the phosphor. Each type of coating was subjected to increasing numbers of UV photons (up to 10^{14} per cm^2), after which the Quantum Efficiency was measured. This was used to obtain a plot over time of the degradation in QE.

With an uncoated sensor, there has been degradation reported [26], due to hot electrons trapped in the oxide coating over the photo gate. This reduces the charge transfer efficiency of the sensor, lowering the QE. So the degradation of the coating will be normalized with respect to the degradation of an uncoated sensor.

A sensor was placed in the camera, turned on, and then light with a wavelength of 254nm was projected onto it. This was done for several hours, however in order to expose the sensor to more than 10^{12} photons in under 8 hours (due to safety concerns the lamp could not be left on overnight), the filters (such as the visible light block filter and the 254nm narrow band filter) could not be used. In these cases the unfiltered light from the lamp was focused onto the sensor for several hours. The results, shown in Figure 12, show no substantial degradation in QE. There is no change that is greater than the error involved in the test, so no QE degradation could be observed.

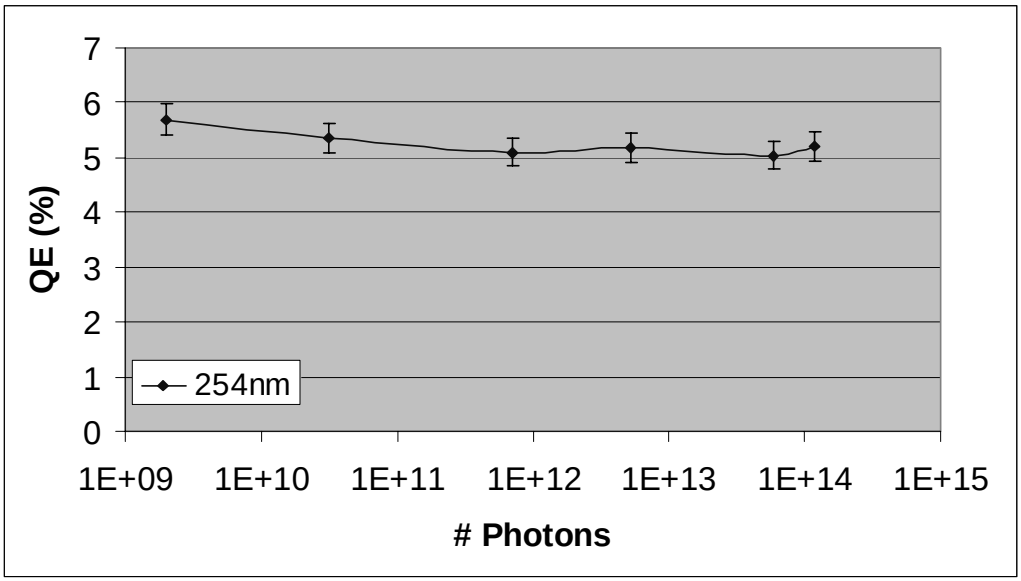

Figure 12 – QE change at 254nm of uncoated DALSA IA-D1-0256 Sensor due to UV degradation

Results for the coated sensors were similar, showing no change greater than the error involved in the tests. In order to perform proper UV degradation tests, a UV laser would be required, that could provide the required number of UV photons in a short enough time period to make the test practical. Further exposure with the present equipment was not practical, in fact, as can be seen in the figure above, the 6^{th} exposure was unfiltered light focused with a lens, for 7

hours. This showed no degradation at all. For this reason, the QE degradation test was not performed on any of the coated sensors reported here, and will not be discussed.

Although the QE did not degrade upon exposure to UV, there was evidence of UV damage to the sensor. During a CTF test, an uncoated sensor was placed in the path of focused, unfiltered light from the Oriel source for 60 seconds. The reading on the optical power meter was 110,000 uW/cm2 (however the light meter assumes one wavelength and the lamp was emitting multiple wavelengths so it's not entirely accurate). The output of the sensor was saturated – this is far beyond the operating conditions of the sensor. After only 60 seconds, there was evidence of UV damage, as can be seen in a photo taken with the damaged sensor in Figure 13.

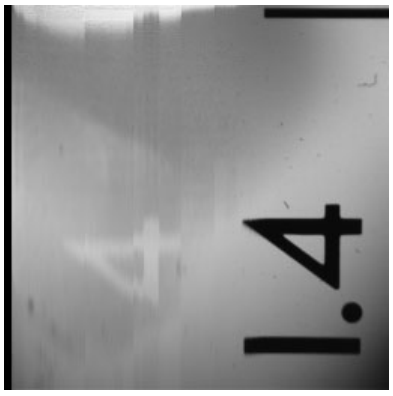

Figure 13 – Image taken with IA-D1-0256 Sensor showing a "burn-in" of an image due to UV damage

The image of the number "4" can be seen burned into the sensor on the left side of the picture. When that 1.4 is moved over to the damaged region, shown below in Figure 14, the damage to the sensor can be seen.

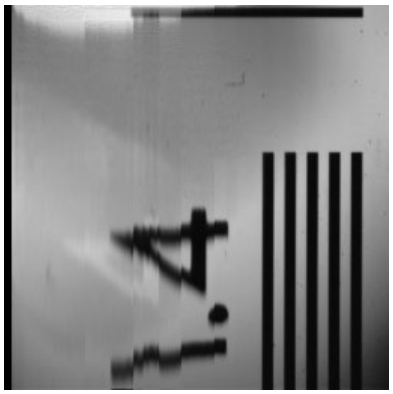

Figure 14 - Image taken with IA-D1-0256 Sensor showing an image in the UV-damaged region

This was repeated several times with uncoated sensors and the results were similar. However, when repeated with all sensors coated by AST and the doctor blading method, there was no damage evident after 60 seconds, or even 5 minutes. The coating on the Laser-Ablated sensors was too thin to be viable so these were not tested.

Although this is not the normal operation of a sensor, it appears the phosphor coating, in all cases, was able to protect the sensor from an over-exposure of UV radiation. While it could not be shown that the phosphor coating extended the lifetime of the sensor under normal operating conditions, it does seem that the coating can protect the sensor from an accidental exposure of high light levels that would normally damage the sensor.

4 Simulation

This chapter describes the MATLAB simulation that was created to simulate the inorganic phosphor coatings performed in this research. Actual simulation results, and the parameters used to perform those simulations, will be presented with the individual coating methods in Chapters 5, 6, 7, and 8. That MATLAB source code is shown in Appendix A.

4.1 Introduction

The simulation is a MATLAB function that can help to show the trends involved with changing various aspects of the coating, and how they affect the properties of the coated sensor. It is not the purpose of this simulation to be able to predict the results of a coated sensor. Instead, it is more an analysis tool to show what the simple theory predicts. Where the experimental results deviate from theory, this gives us insight as to other factors that might be at work that were unaccounted for (contaminations, non-uniformities, etc.). In fact, for each type of coating there are four empirical parameters that must be calibrated to make the curve "fit" the experimental results. These empirical parameters, once set for a specific type of coating, can be used to predict results for small changes in parameters (but only with that same coating technique). However the real benefit lies more in seeing what values of coefficients are needed to fit the experimental results, and then using the values of those empirical parameters to understand more about the coating.

The input is an array of 256 by 256 floating point numbers, the same size as the image sensor array. This array is used to represent the intensity of incoming photons at each pixel. The coating thickness is represented by a 256

by 256 matrix, each entry corresponding to the thickness directly over top of a given pixel. In this way almost any coating topology can be represented.

The other input variables are the number of slices the coating will be divided into, the absorption coefficient and scattering coefficient of UV light in the coating, the absorption coefficient and scattering coefficient of re-emitted light in the coating, the pixel size, and the phosphor efficiency.

The output is an array of 256 by 256 floating point numbers that represent the photons collected by the array. Since the input was 100 for each pixel, each number in this output array can be considered a percentage of the incident photons that arrive at the surface of the sensor.

4.2 Simulation Functionality

A Schematic representation of the coating simulation is shown below in Figure 15.

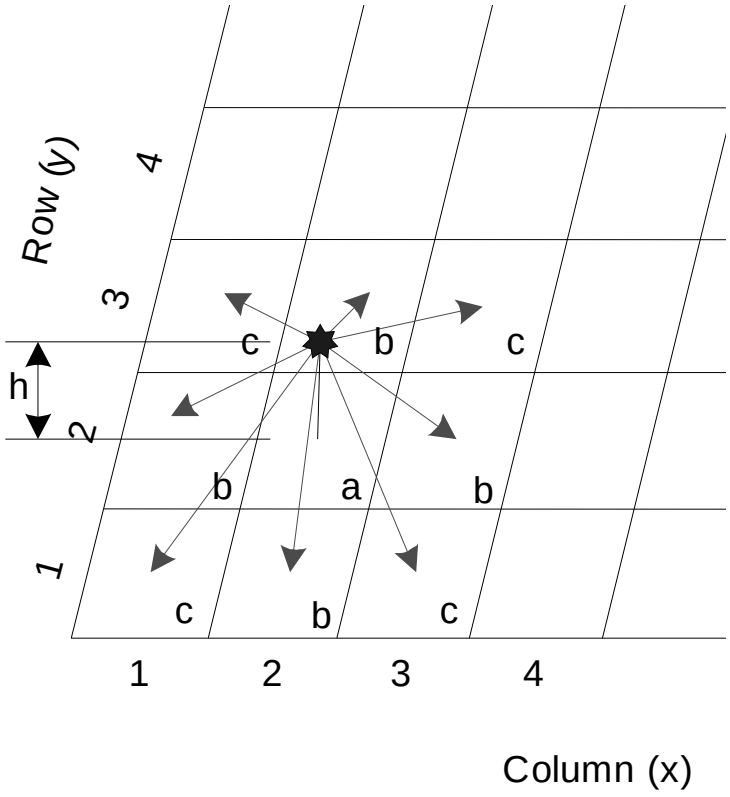

Figure 15 - Schematic Representation of MATLAB coating simulation

The simulation takes the incident light, assumed to be collimated, over a certain pixel (in this example, (2,2)). As the light travels through each "slice" of the coating, some of it gets absorbed, specified by Equation 8, Beer's Law [23].

$$I(t) = I_0 e^{-\alpha_{abs} t} \qquad \textbf{(Equation 8)}$$

Where I_0 is the intensity of incident light traveling through the coating, towards pixel (2,2) before the slice, and $I(t)$ is the intensity of the light after traveling through the slice. α_{abs} is the absorption coefficient of UV photons in the coating, and t is the thickness of the slice of coating the photons have just traveled through.

As well as getting absorbed, some of the light gets scattered, specified by Equation 9 below. This is the same as Equation 8, but with α_{sca} representing the scattering coefficient of UV photons in the coating.

$$I(t) = I_0 e^{-\alpha_{sca} t} \qquad \textbf{(Equation 9)}$$

It is assumed that any photons scattered in the coating will be lost, and not received by the sensor. Since most photons are probably scattered at least once as they make their way through the coating, it would be impossible to simulate it fully. Instead, this scattering coefficient is more a measure of the *loss* due to scattering, which is a small fraction of the actual amount of scattering that goes on.

The UV photons absorbed by the phosphor are subsequently re-emitted as visible photons, the percentage re-emitted is determined by the phosphor efficiency. Unlike the incident photons, these photons are emitted isotropically. So to calculate the amount of photons that are traveling towards each pixel, a solid angle correction must be applied. This is essentially the percentage of total emitted photons that are traveling towards the given pixel. The actual solid angle correction is extremely complicated, and since the simulation is not meant to duplicate exact results, but rather to show trends, an approximation is appropriate.

The approximation involves treating the geometry as two-dimensional instead of three-dimensional. As can be seen in the previous figure, the simulation only calculates the re-emitted photons that travel towards the adjacent pixels, so 9 pixels in total. Of those 9 different pixels, there will be 3 values of solid angle correction; the pixel directly underneath (a), the pixels that differ by one column OR one row (b), and the pixels that differ by one column AND one row (c).

Figure 16 shows the schematic representation for this two-dimensional approximation of these three kinds of pixels.

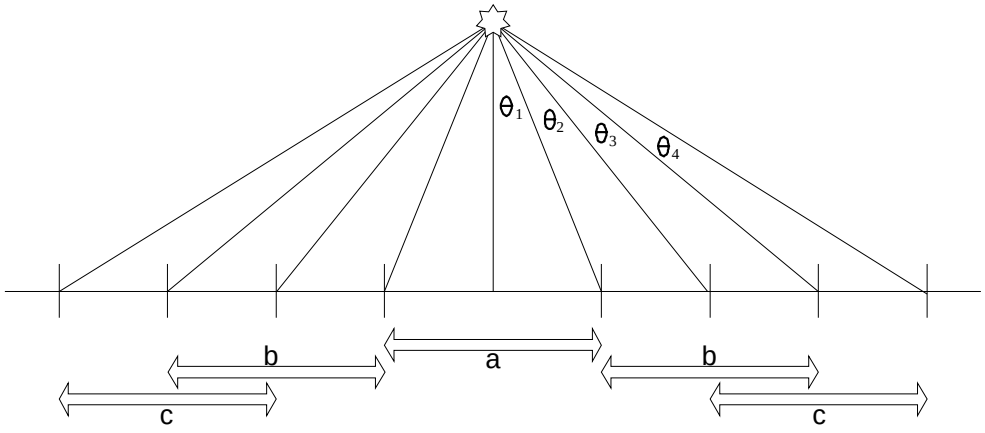

Figure 16 - Schematic representation of 2-D approximation

Here, the type a pixel is directly underneath the point source of photons, the type b pixels are adjacent to that, and the type c pixels are further still, their location slightly overlapping the type b pixels to represent the three-dimensional geometry. The calculation of the angles follows below in Equations 10 to 13:

$$\theta_1 = \tan^{-1}\left(\frac{\frac{1}{2}\,pixel\_size}{h}\right) \qquad \textbf{(Equation 10)}$$

$$\theta_2 = -\theta_1 + \tan^{-1}\left(\frac{pixel\_size}{h}\right) \qquad \textbf{(Equation 11)}$$

$$\theta_3 = -(\theta_1 + \theta_2) + \tan^{-1}\left(\frac{\frac{3}{2}\,pixel\_size}{h}\right) \qquad \textbf{(Equation 12)}$$

$$\theta_4 = -(\theta_1 + \theta_2 + \theta_3) + \tan^{-1}\left(\frac{2\,pixel\_size}{h}\right) \qquad \textbf{(Equation 13)}$$

Finally, the solid angle is simply the percentage of the angle taken up by the pixel, compared to the entire circle centered around the emission point, as shown below:

Solid Angle Correction for Pixel Type a: $\frac{2\theta_1}{2\pi}$

Solid Angle Correction for Pixel Type b: $\frac{\theta_2 + \theta_3}{2\pi}$

Solid Angle Correction for Pixel Type c: $\frac{\theta_3 + \theta_4}{2\pi}$

The simulation then applies the solid angle correction to determine how much of the emitted light is traveling towards a given pixel. It then calculates the three-dimensional distance from the emission point to the middle of the pixel, then applies the scattering and absorption equations over that distance. The scattering and absorption coefficients must be different, however, since now this is re-emitted light, at a different wavelength that the incident light. These were represented as absorption_coeff_2 and scattering_coeff_2. As well, the phosphor efficiency is virtually zero at this wavelength so any photons absorbed are considered lost.

After applying those losses, the photons are considered to have arrived at the pixel, and so are added to the element in the output array for that pixel. This is repeated for the pixel directly underneath and all eight pixels adjacent to the emission point.

The amount of scattered and absorbed photons, calculated using Equations 8 and 9, are subtracted from the light traveling through the coating, and the calculations are then repeated for the next slice down. All sensors have approximately 5% Quantum efficiency at the UV wavelength of 254nm, so 5% of any light remaining (not scattered or absorbed as it went through the coating) is added into the matrix for that pixel. Then the calculations are repeated for each pixel.

4.3 QE Simulation

Simulating the QE is the simplest application of the coating simulator. Using an incident matrix of uniform values (representing incident light intensity), and a uniform thickness matrix, the simulation produces an output with each pixel getting the exact same amount of light. In order to create a QE spectrum (QE values for different wavelengths) the phosphor efficiency was changed. The datasheets for the phosphor listed the efficiency of the phosphor at each wavelength, and this was used in the simulation. The simulator does not, however, take into account changes in the absorption or scattering coefficients due to wavelength.

The QE simulation was also used to "calibrate" the simulator for a given coating technique. The coefficients were changed until the curve matched the experimental results as closely as possible. The values of the coefficients and how they changed with different coating parameters is quite useful in indirectly determining some of the properties of the coating.

4.4 PRNU Simulation

Simulating the PRNU involves passing the coating simulator an incident matrix, containing elements of all constant value (representing flat-field illumination) and a thickness matrix with a range of values, representing an uneven coating. The values used for the four coefficients will be the same as the calibrated values determined during the QE simulation.

This simulation can take into account the PRNU caused by different thicknesses within the coating. It does not take into account differences in density of the coating, or differences in phosphor efficiency within the coating.

Generating the thickness matrix is the most involved part of this simulation. The first step was to look at the SEM photographs of the cross-section and top view of the coating in question. From this, a visual inspection was made of four different factors; the average thickness, the thickness variation, the amount of uncoated space, and the size of clusters (if present). The four factors were used to create an approximation of the coating, using random numbers (fitting a Gaussian distribution) within that range. Each coating had a different thickness matrix, and the generation of that matrix is explained when simulation results are presented.

It is also important for the PRNU simulation that the average illumination of the sensor be the same. All of the sensors were measured with an illumination yielding a DN (digital number) of 128 ± 10. To make the PRNU calculated of the simulated coating the same, an illumination was used that yielded a brightness of 128 ± 10.

The PRNU of the coating is calculated using the photons that have passed through the coating. The PRNU of the sensor (this is what was measured experimentally) must be found by combining the coating PRNU and the uncoated PRNU at the wavelength of peak emission of the phosphor. The different signal levels seen at the surface of the sensor (after passing through the coating) and after being read by the sensor are represented by normal distributions. The PRNU comes directly from the standard deviation of that normal function. To incorporate both PRNUs, the normal functions must be convolved. The convolution of two normal functions results in a third normal function, with a mean equal to the sum of the two original means, and a standard deviation equal to the sum of the two original standard deviations [21]. Therefore *adding* the PRNUs will yield the sensor PRNU. For example, if the phosphor emits green (540nm), the simulated PRNU would be the results from the simulation *plus* the uncoated PRNU at 540nm.

4.5 CTF Simulation

Simulating the CTF involves giving the simulator an incident matrix of black and white lines (0's and 100's) of increasing spatial frequency. The thickness matrix is made up of constant values. Since the simulator only operates on a resolution of one pixel, when making the incident matrix the number of spatial frequencies was limited. The spatial frequencies chosen were 1, 1.5, 2, and 2.5 pixels/line. 3 pixels/line would have yielded 100% CTF because the simulator does not calculate light scattered beyond adjacent pixels, so this was not included in the simulation. To represent the fractional values, for example 1.5 pixels/line, one pixel was set to 100% and the next pixel to 50%, then repeated. The simulation was performed only at 254nm, since the only spreading involved comes from the isotropic re-emission of photons. At longer wavelengths the phosphor has 0% efficiency so simulating the CTF would not reveal any useful results.

5 AST Coating

5.1 Theoretical Explanation

Applied Scintillation Technologies (AST) is a company that specializes in imaging and detection solutions using the latest phosphor and scintillation technology. They have proprietary deposition techniques that enabled them to deposit inorganic phosphor on DALSA's CCD image sensors. One of their techniques, which can be performed on packaged unwindowed sensors, enabled the phosphor to be deposited in an extremely thin layer, only 1-2 crystals thick, yet extremely uniform over the entire sensor. This is the coating method that is examined here. Unfortunately, this thickness was not controllable, and was a function only of the crystal size and shape.

Another method, which could not be performed on a packaged sensor (and would therefore require a bare die) allowed the thickness to be controlled, but AST did not have the resources to perform this coating within the timeframe of this research.

5.1.1 2212 Phosphor Coating

AST coated fused silica slides at the same time as the sensors, so that the coating could be examined in a Scanning Electron Microscope (SEM). Photographs taken from the SEM are shown in Figure 17, Figure 18, and Figure 19. As can be seen, the phosphor is composed of smooth, spherical-shaped crystals. In the creation of this phosphor, each crystal was formed individually, causing the round shape [22]. The coating is quite even, even across large areas. The thickness of this coating is approximately 10 microns.

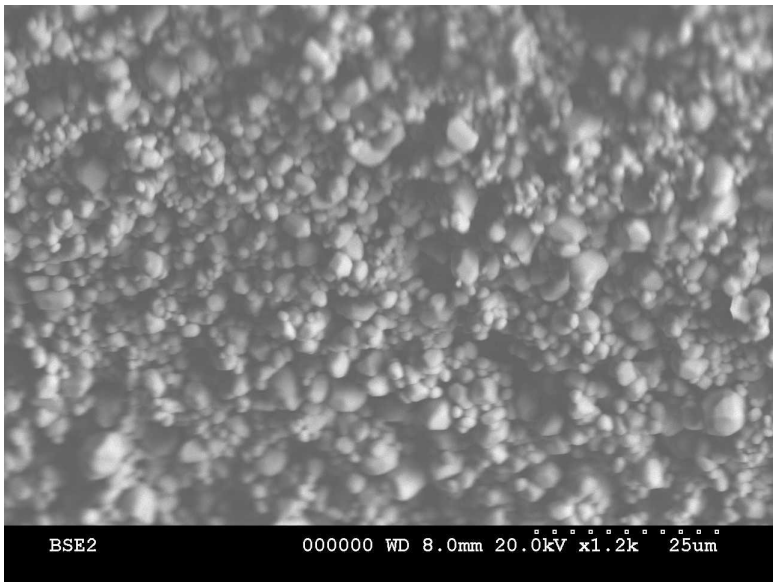

Figure 17 - Overhead SEM photograph of AST 2212-phosphor coating on glass slide, showing coating uniformity

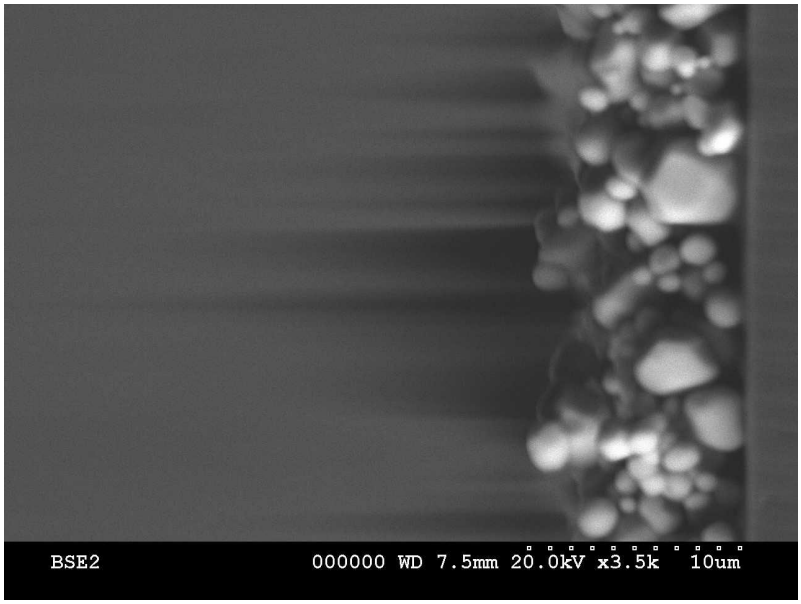

Figure 18 – SEM photograph of cross section of AST 2212-phosphor coating on glass slide, showing phosphor size and shape

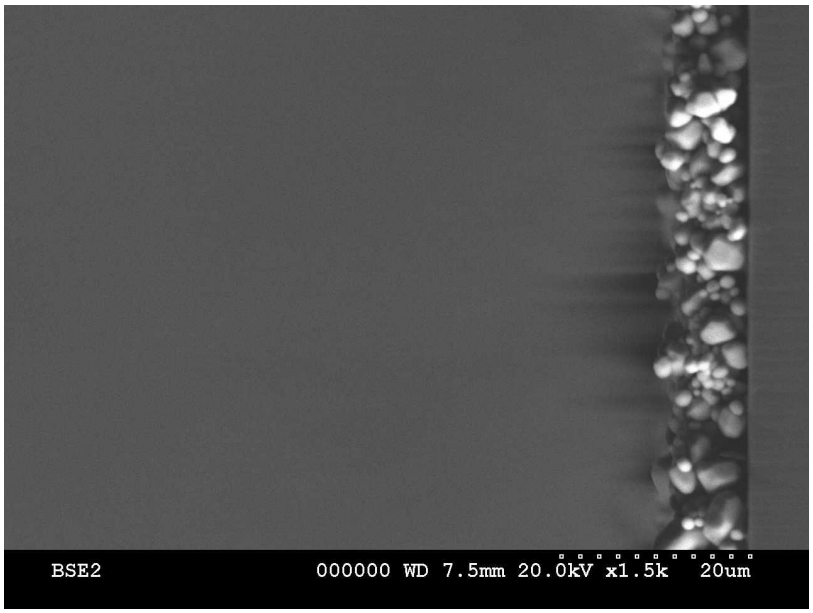

Figure 19 – SEM photograph of cross section of AST 2212-phosphor coating on glass slide, showing thickness and thickness uniformity

5.1.2 2345 Phosphor Coating

The 2345 coating, composed the same as the AST 2212 phosphor coating shown previously, and deposited the same way, showed the same high uniformity. SEM photographs are shown in Figure 20 and Figure 21. However, the crystal shape is quite different. These crystals were formed by growing a large sheet of phosphor, then breaking it up [22]. This process yielded crystal shapes that were rougher and had more surface area. The different shape changes the thickness of the coating (in this case, 7 microns), and as will be shown, changes the properties of the coating as well.

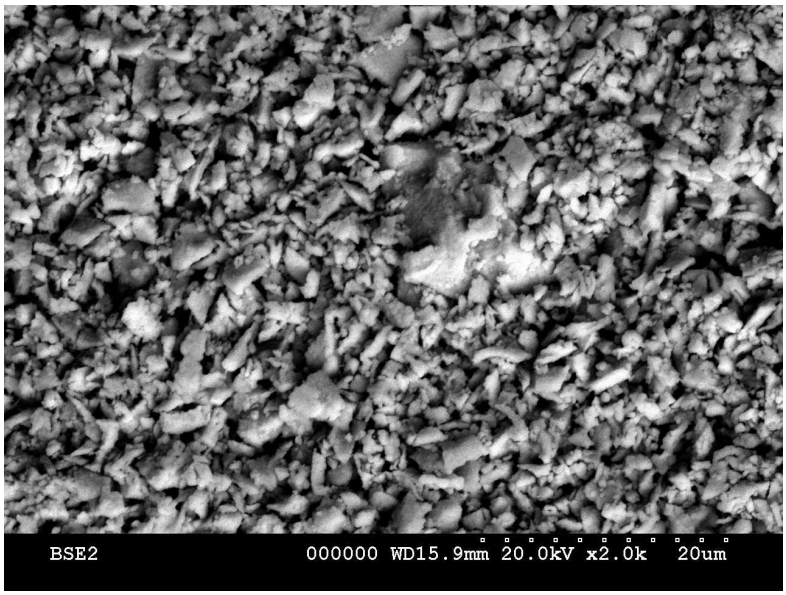

Figure 20 - Overhead SEM photograph of AST 2345-phosphor coating on glass slide, showing coating uniformity

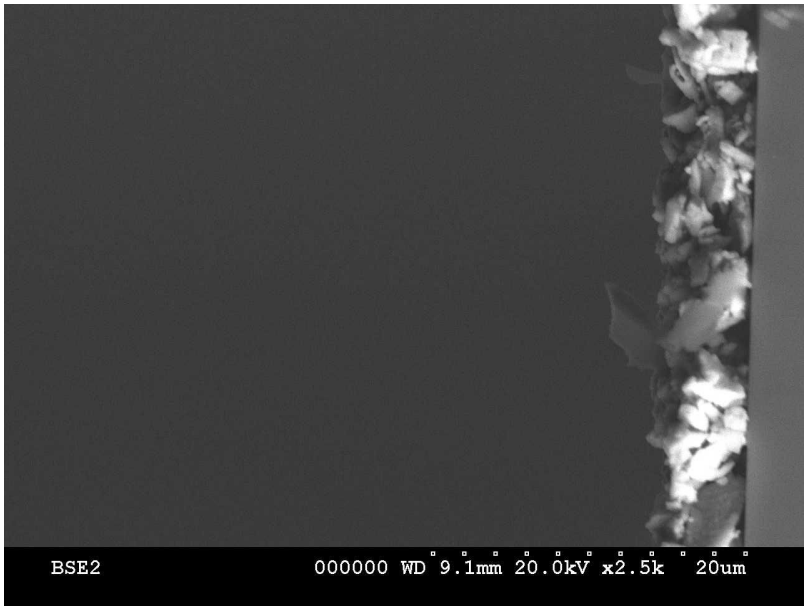

Figure 21 – SEM photograph of cross section of AST 2345-phosphor coating on glass slide, showing thickness and thickness uniformity

5.2 Experimental Setup

Since AST performed the actual coating, and it is proprietary, the details of how the coating was performed cannot be presented here.

5.3 Experimental Results

5.3.1 QE Results

The sensors coated with the AST coating were tested for Quantum Efficiency in the manner described in Section 3.1.1. The results of the QE measurements are shown in Figure 22 and Figure 23.

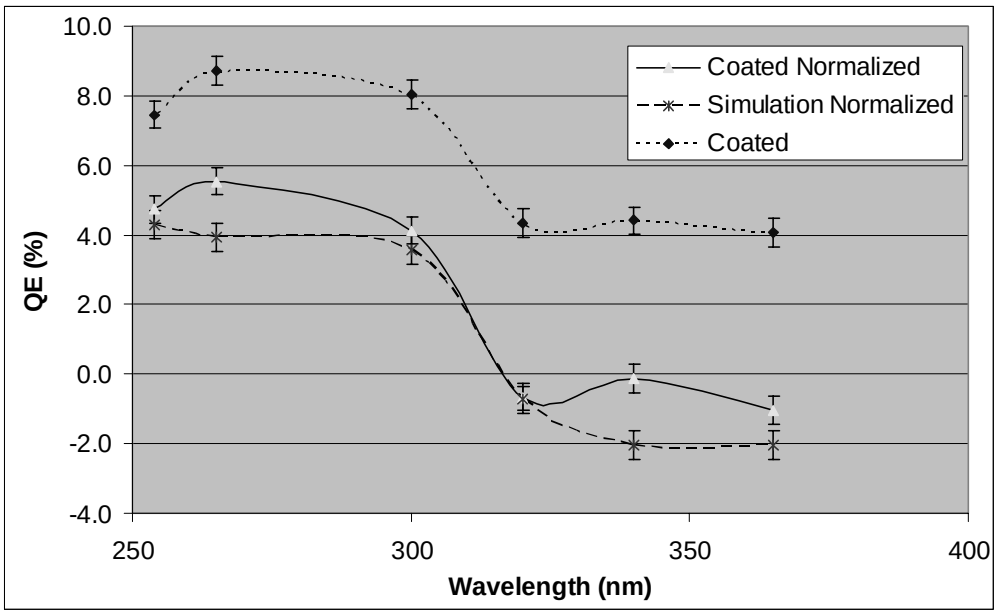

Figure 22 - QE Spectrum of AST 2212-coating on DALSA IA-D1-0256 Sensor

The coated QE is presented to show the absolute performance of the sensor. The 2212-coated sensor shows a peak at 265nm of 9% QE, the same peak wavelength as the settle-coated deposition. This is an increase of 174%

over the uncoated sensor. In order to get a measure of how the coating performed, and properly compare the simulation results, the normalized QE is presented. Here the uncoated QE was subtracted from the coated QE, to get a measure of how much the coating improved the sensor (and not just the absolute performance of the sensor). The simulation assumes 5% QE at all wavelengths with no coating, so 5% was subtracted from the simulation results to obtain the Simulation Normalized QE. The simulation followed the same trend as the results, however it predicted the peak at 254nm (where the phosphor's peak efficiency is).

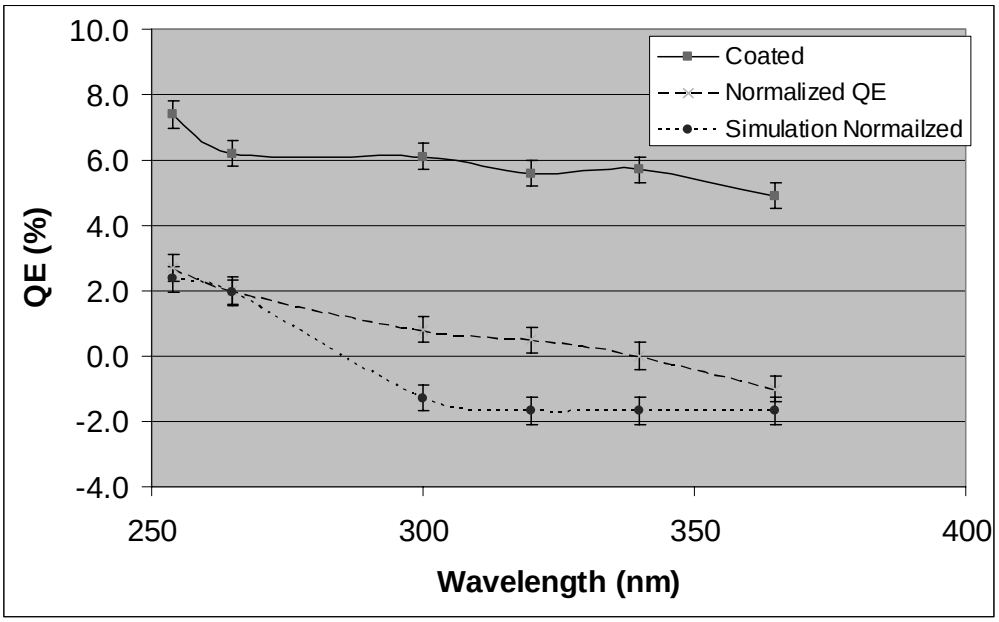

Figure 23 - QE Spectrum of AST 2345-coating on DALSA IA-D1-0256 Sensor

For the 2345-Coated Sensor the peak is at 254nm, the 7.5% QE is 74% higher than the uncoated sensor. The simulation agreed closely with the results, except it predicted lower QE's at the longer wavelengths. Discussion of the results and simulation will follow in Section 5.4

5.3.2 PRNU Results - 2212 Phosphor

The 2212-coated sensor was tested in the manner described in Section 3.1.2. The results for the PRNU test on the sensor coated by AST with 2212 phosphor are shown in Figure 24.

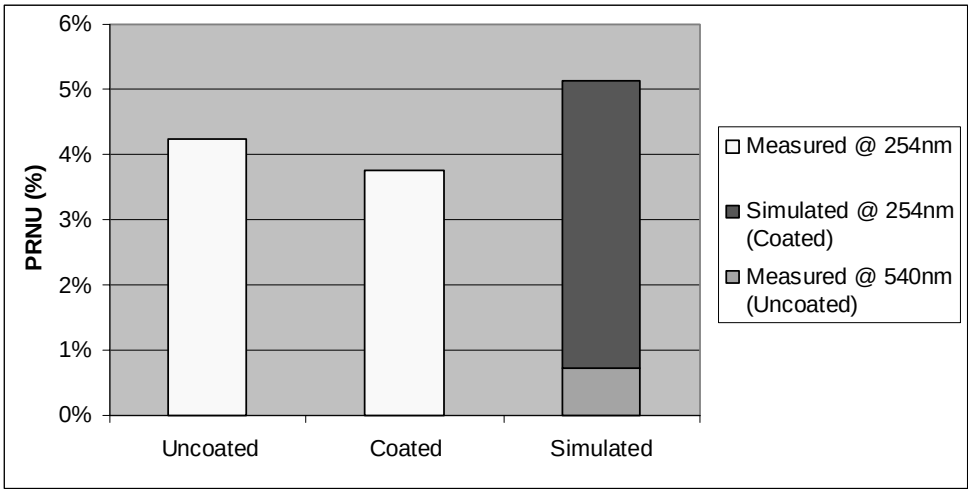

Figure 24 – Coated, Uncoated and Simulated PRNU at 254nm for AST 2212 coating on DALSA IA-D1-0256 Sensor

Figure 24 shows the coated, uncoated and simulated PRNU at 254nm. The coated PRNU at 254nm of 3.7% is actually a decrease of 11% from the uncoated sensor. While it seems illogical that adding this type of phosphor coating would actually decrease the PRNU, this is due to sensor design, and will be explained in the results and discussions section which follows. The uncoated PRNU at 540nm of approximately 0.8% reflects what is expected out of this sensor under normal operation. The simulation predicts the expected PRNU at the sensor's surface after the UV photons have passed through the coating and been converted to 540nm (in this case) photons. The uncoated PRNU at 540nm is added to the simulation results to represent the additional PRNU as the photons pass into the sensor. This allows for a more direct comparison with the measured PRNU, which is also based on photons collected by the sensor (and

not just passing through the coating). The simulation results of 5.2% match quite closely with the measured results. Discussion of the results and the simulation will follow in Section 5.4.3.

5.3.3 PRNU Results - 2345 Phosphor

The 2212-coated sensor was tested in the manner described in Section 3.1.2. The results for the PRNU test on the sensor coated by AST with 2212 phosphor are shown in Figure 25.

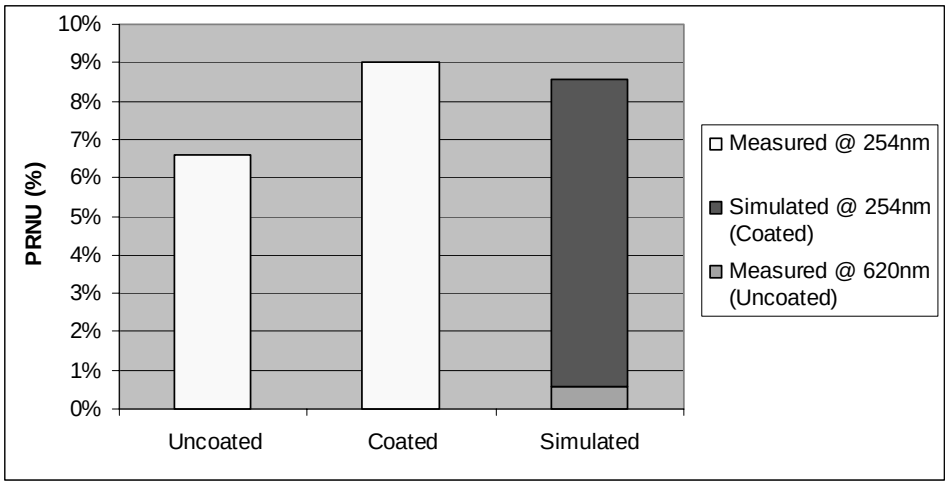

Figure 25 - Coated, Uncoated and Simulated PRNU at 254nm for AST 2345 coating on DALSA IA-D1-0256 Sensor

In this case, all PRNUs are much higher than the 2212-coated sensor. The uncoated PRNU at 254nm is higher than the other 2212-coated sensor, however this type of difference is normal and due to sensor design, which will be discussed in Section 5.4.4. The coating causes the PRNU to degrade, in this case, from 6.6% to 9.0%, a relative drop of 37%. The simulation predicts the PRNU quite closely. In this case, since the 2345 phosphor's peak emission is 611nm, the uncoated PRNU at 620nm was added to the simulation results to represent the additional PRNU from the photons moving into the sensor. The

measured PRNU at 540nm is added to the simulation to represent the measured results more closely, as explained in Section 4.4.

5.3.4 CTF Results – 2212 Phosphor

Ideally, a CTF measurement of a sensor would be taken before coating, and again after coating. This way the individual characteristics of the sensor would not be a source of error in reporting the degradation in CTF. This was not possible while testing the AST coated sensors, since they were shipped off to be tested before the CTF test was developed. The plan was to have a second batch of sensors coated, however this was not possible due to resource constraints at AST. In order to get a reasonable measure of the degradation in CTF, measurements were taken from 20 uncoated sensors, and the results averaged. This one result was used as the uncoated CTF.

The coated sensors were tested for CTF in the manner described in Section 3.3. The results are presented below in Figure 26.

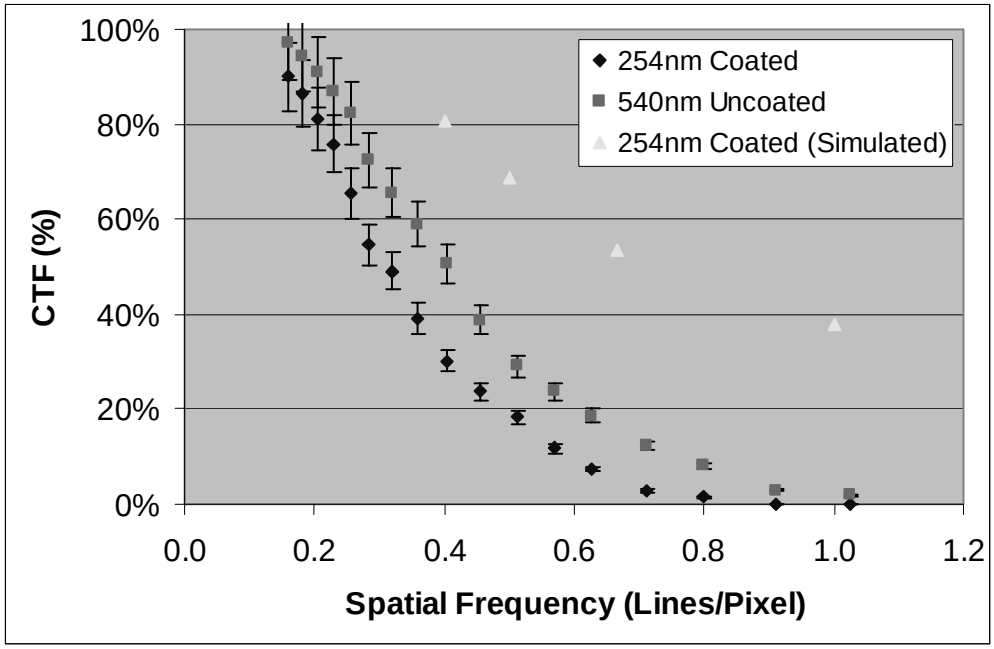

Figure 26 - Coated, Uncoated and Simulated CTF for AST 2212 coating on DALSA IA-D1-0256 Sensor

All three CTF curves shown are the same shape. At low spatial frequencies, the pattern is almost perfectly reproduced on the sensor, as expected. As the lines get narrower and the spatial frequency increases, the CTF drops.

The coating caused the CTF to degrade significantly; the CTF at ½ Nyquist frequency is 29.1% for the uncoated sensor, and 18.3% for the coated sensor, a relative drop of 37.1%. The simulation predicted a much higher CTF at ½ Nyquist frequency of 68.9%.

5.3.5 CTF Results - 2345 Phosphor

Again, the uncoated CTF measurements were an approximation of 20 other uncoated sensors. The coated sensor was tested for CTF in the manner described in Section 3.3. The results are shown in Figure 27.

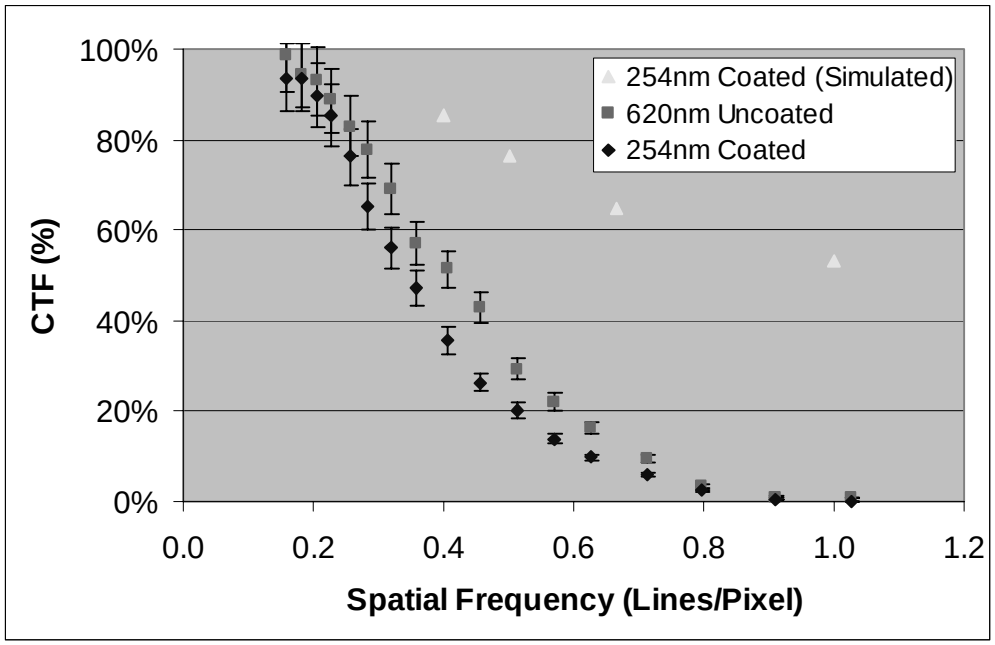

Figure 27 - Coated, Uncoated and Simulated CTF for AST 2345 coating on DALSA IA-D1-0256 Sensor

All three curves have the same shape, as expected, with the CTF decreasing as the spatial frequency increases. The coating did cause the CTF to degrade over its uncoated value, but not as much as with the 2212-coated sensor. The uncoated CTF at ½ Nyquist frequency (in this case measured at 620nm, the peak emission of the 2345 phosphor) is 29.2%, and the coated CTF at ½ Nyquist frequency measured at 254nm is 20.1%, a degradation of 30.1%. Although the simulation predicted a very high value (as before) of 75.5% at ½ Nyquist frequency , it did accurately predict that the CTF for this coating would be higher, in general, than the 2212 coating.

5.3.6 Summary of Results

A Summary of all the results for the AST coating is shown in Table 2.

Table 2 - Summary of experimental results for AST coating on DALSA IA-D1-0256 Sensors

	AST-Coated 2212	AST-Coated 2345	Settle Coat	
			Thin	Thick
Estimated Thickness	10μm	7μm	<20μm	>50μm
Peak QE Increase	174%	74%	36%	210%
PRNU Degradation @254nm	-11% (increase)	37%	700%	160%
CTF Degradation @254nm, ½ Nyquist	37.1%	30.1%	n/a	n/a

The QE of the AST-coated sensors was below that of the settle coated sensor. However, this is most likely due to the reduced thickness of the coating, so the coating didn't absorb as many UV photons. However, the PRNU of the 2212 AST-coated sensors actually improved over the uncoated PRNU. The more advanced coating technique created a more uniform coating. This shows the AST coating is viable, but more work needs to be done increase the QE (while keeping PRNU and CTF as low as possible) most likely by adjusting the thickness of the coating. A thicker or denser coating might yield a better QE, however due to the characteristics of AST's coating method, trying to make it thicker might reduce the quality of the coating.

5.4 Simulation and Discussion

5.4.1 QE Results – 2212 Phosphor

There are two main features of these results. First, the peak QE at 265nm does not agree with the simulation. The phosphor's peak excitation is at 254nm so it follows from theory the peak QE should be at 254nm. However the simulation does not take into account secondary factors such as the changing of the absorption or scattering due to different wavelengths. There may be other impurities in the coating that absorb the 254nm more than the 265nm. The second main feature is the QE dropping around 300nm. This follows exactly with theory, as above 300nm the efficiency of the phosphor drops off to almost zero. At 320nm the QE of the coated sensor drops to less than the uncoated, because the coating is not converting, and actually blocking the photons that might normally get through. This sensor is really meant for the 250-300nm region, though, so the drop-off at 300nm is not critical.

The simulation parameters, explained in Section 4.2, were:

absorption_coeff=0.055

scattering_coeff=0.002

absorption_coeff_2=0.001

scattering_coeff_2=0.005

These were the values that best fit the experimental data. The absorption and scattering coefficients of the re-emitted light were so low that making them lower by a factor of 10 only changed the result by less than 0.1%. Although these are coefficients, and supposed to be independent of coating thickness, these low coefficients are actually due mostly to the thin coating. The AST coating, by design, can only make a layer of 1 to 1 ½ particles thick. So a re-emitted particle doesn't really have any chance to get re-absorbed. The

coefficients are based on photons traveling through many spaces and phosphor crystals, so although the absorption and scattering coefficients are probably lower than they should be, it gives us insight that little re-emitted light is being lost due to absorption and scattering.

5.4.2 QE Results - 2345 Phosphor

The normalized QE, shown in Figure 23, is in this case an unremarkable curve. The highest measured QE was at 254nm, in agreement with theory, and drops almost linearly as the wavelength gets longer. Below 254nm it is possible the QE could get even higher, but the equipment to generate those wavelengths was not available. Again, the phosphor's efficiency decreases at longer wavelengths and blocks the UV photons from reaching the sensor. The simulation predicts a drop in QE of 2.8% at 300nm, due to the sudden drop of phosphor efficiency at that wavelength. Since the phosphor is converting only 3% of UV to visible at these wavelengths, it can be assumed that the raised QE is due to more UV light getting through to the sensor than theory would predict. Since the simulation does not account for a change in scattering of absorption coefficient with wavelength (only the phosphor's efficiency changes with wavelength), perhaps at longer wavelengths the scattering and absorption is vastly reduced. This could be due to the unique shape and composition of the phosphor, however these are properties that are not specified in the phosphor datasheets and measuring them is out of the scope of this work. However it does indicate that this coating would be preferable for situations where the coated sensor would be occasionally used for longer wavelengths.

Even though the theoretical QE at 254nm is higher than the 2212 phosphor, this one gave a lower sensor QE. This was not expected, since the 2212 coating has an 85% theoretical efficiency and the 2345 has a 100%

theoretical efficiency. There are three possible explanations. First, it's possible the shape caused more scattering and reflection, due to the sharper edges and more surface area of this phosphor. The photos in Section 4.1 show the 2212 phosphor to be round and uniform in shape, and the 2345 phosphor to be jagged and sharp. Second, the reduced thickness means more UV photons go right through the phosphor layer without getting absorbed. Third, the CCD is less sensitive to red, which is the peak emission of this phosphor.

The simulation parameters were:

absorption_coeff=0.055;

scattering_coeff=0.005;

absorption_coeff_2=0.001;

scattering_coeff_2=0.005;

Again, these coefficients were not results of the simulation, but rather the necessary empirical parameters that made the simulation results fit best with the experimental data. In this case the only coefficient different than the 2212 coating was the scattering coefficient of the incident UV photons. It was 0.05 instead of 0.02. This is easily explained by observing Figure 21 which shows the jagged shape of the crystals, as opposed to the smoother shape of the 2212 phosphor. It follows that a more jagged shape, with more surface area and more edges, would cause more scattering.

5.4.3 PRNU Results – 2212 Phosphor

The PRNU results for the uncoated sensor at 254nm are quite high. This is due to the design of the sensor. The absorption coefficient of 254nm photons in the gate material (2nm) is such that all the photons get absorbed before ever reaching the sensor. To increase blue light and UV response, the sensors were designed with a 4% gate reticulation, a small area of the active pixel where the

gate is pulled back. This allows approximately 4% of UV photons to get through. Because the gate reticulation is so small (6.76 square microns compared to 169 square microns for the whole pixel, assuming a 13 micron square pixel), the tolerances in the IC process cause different sizes of gate reticulation. With a tolerance of 100nm, for example, the area of the gate reticulation could vary by up to 118%. At longer wavelengths the photons pass through the gate material and get absorbed by the whole pixel, which with the same 100nm tolerance, would only vary in area by 3%. This is shown by the uncoated PRNU at 540nm.

The 254nm coated PRNU has to do with the uniformity of the coating. Certain spots may contain more or less phosphor, or larger or smaller phosphor crystals. Therefore different pixels in the sensor may receive different amounts of light emitted by the phosphor. Although it looks like coating the device improves the PRNU at 254nm, which doesn't seem to make sense, the coating converts the 254nm photons into 540nm photons which pass into the sensor with very little additional PRNU. The difference between the coated PRNU at 254nm and the uncoated PRNU at 540nm can be considered the "coating PRNU", in this case the coating caused the PRNU to degrade by 3%.

The thickness matrix for the simulation was determined by examining the SEM photographs of the coating and making measurements. It was determined that the mean of the coating thickness was 10μm, the standard deviation was 1.5 microns, and there were no clusters or empty spaces in the coating. These parameters were used to create a thickness matrix of randomly generated numbers, using a normal distribution with a mean of 10 and a standard deviation of 1.5. The coefficients used were the ones determined during the QE simulation.

The simulation yielded results slightly higher than measured results. Since the simulation did not take into account PRNU due to non-uniformities in

phosphor density or phosphor efficiency (these were constant throughout), it was expected for the PRNU to be slightly lower than measured. This leads to the conclusion that either these effects are not that significant, or that there are other effects at work reducing the PRNU. One such effect that the simulation did not consider was the scattering of light. The simulation considers light *lost* to scattering, but not the scattering that will tend to "spread out" the light as it goes through the coating. This spreading effect could have contributed to the slightly lower PRNU. The simulation is a first-order approximation and meant to show the general trends that are expected for coatings, not to reproduce results exactly. The fact that it is so close to the measured results shows that the simulation is accurate, and the coefficients used and measurements taken are quite accurate.

5.4.4 PRNU Results – 2345 Phosphor

The same high PRNU at 254nm, 6.6%, displays itself here, again due to the gate reticulation. However it was much higher than the 4.2% PRNU of the 2212-coated sensor. Since the gate reticulation is so small process differences affect the PRNU. In this case the sensor was made from a different wafer run where the tolerances may have been higher. The uncoated PRNU of 0.54% at 620nm is very low, and close to the value of the other sensor (the one coated with 2212 phosphor), so the PRNU of coated sensor should not be affected (since the 611nm re-emitted photons will be the ones absorbed into the sensor).

Since the 2345 phosphor's emission peak is 611nm, we should compare the coated PRNU at 254nm with the uncoated PRNU at 620nm. The 254nm PRNU degraded 37% from the 620nm uncoated result. The other two coated results are consistent with what was expected and seen before. Figure 28 shows

256 pixel by 256 pixel images taken with the 2345-coated sensor uniformly illuminated with 254 and 540nm light.

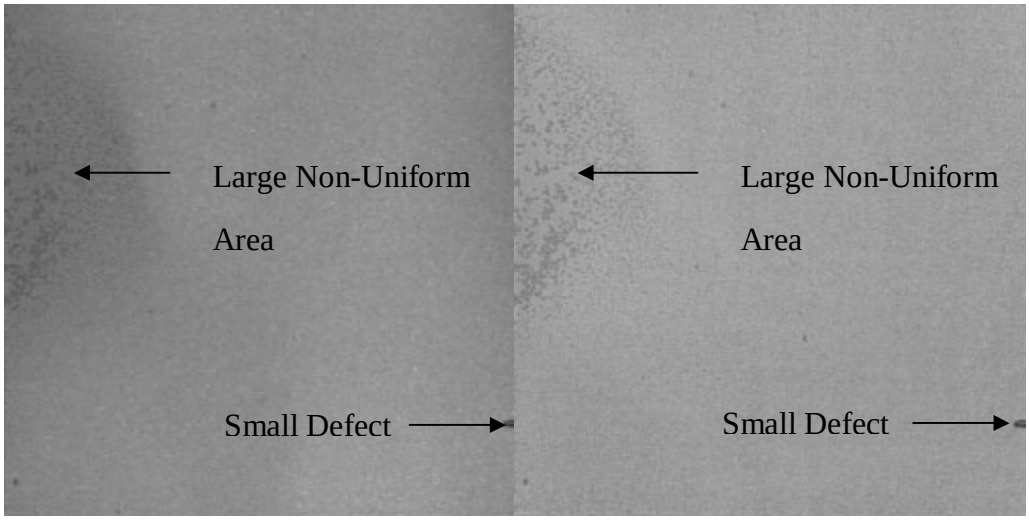

Figure 28 – Images taken with DALSA IA-D1-0256 Sensor coated by AST with 2345 phosphor, illuminated with 254nm (left) and 540nm (right) light

As can be seen, the coating has a spot near the upper left where it's non-uniform. This area was not used for the PRNU calculation, since it was assumed to be an error, and not a normal consequence of the coating. However on the 254nm photo the image is visibly darker on the left. This does not appear on the 540nm photo, so it can be concluded that this is due to a non-uniformity in the phosphor coating, and not due to the sensor or the light. This seems to be more of a problem with the individual coating than with the phosphor itself. The defect along the right edge near the bottom is also due to the coating, since it was not present in the uncoated image. The sensors were shipped after they were coated, so the defects may be due to either the coating itself, or the coating may be fragile and the damage occurred during handling.

The thickness matrix for the simulation was generated by first looking at the SEM photos of the coating. It was determined that the mean of the coating

thickness was 7μm, the standard deviation was 2 microns, and there were no clusters or empty spaces in the coating. These parameters were used to create a thickness matrix of randomly generated numbers, using a normal distribution with a mean of 7 and a standard deviation of 2. The coefficients used were the ones determined during the QE simulation.

The simulation's results were only 0.5% lower than the measured result, extremely accurate when considering the approximate nature of the simulation. The simulation also accurately predicted that the 2345 coating would have a higher PRNU than the 2212 coating. Two factors were involved, first the increased variation in the thickness (4μm in this case versus 3μm in the 2212-coating), and second the thinner overall coating. Both of these factors contributed to a greater *relative* thickness variation in the 2345-coating which the simulation accurately predicted would cause an increase in the PRNU.

5.4.5 CTF Results – 2212 Phosphor

The phosphor coating on the sensor causes the CTF to degrade from its uncoated value. This was expected, because of the isotropic emission of the phosphor, and the scattering of photons as they travel through the coating.

For the simulation, the four coefficients (explained in Section 4.2) were set to the values determined during the QE simulation. Although the simulation predicted the shape of the curve correctly, it also predicted a larger CTF than was measured. There are two main causes for this. First, the only spreading that occurs in the simulator is due to the isotropic emission of the phosphor. It does not consider spreading of the pattern due to scattering within the coating. Second, the simulator only calculates photons traveling as far as one adjacent pixel, in reality they may travel further. However the solid angle and attenuation would cause fewer than 1% of the photons to actually arrive at that

pixel so this is not thought to be a major effect. A third possible cause is that the pattern is lined up perfectly in the simulator, whereas it can never be perfect when measured experimentally. However with extensive measuring the greatest difference measured from different alignments was 8% (see Section 3.3), so this is not thought to be a major effect.

5.4.6 CTF Results – 2345 Phosphor

As expected, the coating caused the CTF to degrade by 30.1%, however in this case it did not degrade as much as the previous 2212 coating, 37.1%. There are two factors that would cause the CTF to degrade. First, a thicker coating means that more photons are isotropically re-emitted higher above the surface of the sensor, so they will travel further, laterally, before reaching the surface of the sensor. This will degrade the CTF. As well, the incident photons and the re-emitted photons will scatter in the coating, and be spread out. This coating is thinner, but also scatters more; however in this case the CTF was improved over the 2212 coating.

For the simulation, the four coefficients were set to the values determined during the QE simulation. The simulation predicted a greater CTF than was measured, for reasons explained in the previous section. However it did accurately predict that the CTF would be better with the thinner coating.

The results here are very similar to the 2212-coated sensor, however the degradation at the higher frequencies is not quite as high at 254nm. This is due to the reduced thickness of the coating at this frequency. The 540nm and 620nm results do not see the same kind of gain, probably due to the shape of the crystals which increases scattering. At 254nm the absorption is in the layer of crystals, and since that layer is only a couple of crystals thick the scattering is not as much of a problem.

6 Doctor Blade Coating

6.1 Theoretical Explanation

Doctor Blading (or Knife Casting) is a simple technique that achieves very uniform coatings. It requires a gel (or paste) that can evaporate completely, leaving only a solid residue. The solid residue should have a mass at most 5% of the original mass of the gel. The phosphor is mixed with the paste, which is applied to the substrate to be coated. A high precision blade with adjustable height scrapes off the paste, leaving a uniform coating. The paste then evaporates leaving only the phosphor.

This section deals with doctor blading theory, what other related work has been performed [6, 7, 8, 11, 12], and the parameters that can be used to predict the output variables. The doctor blading work performed in this research is outlined in Section 6.2, with the results presented in Section 6.3.

6.1.1 Benefits

Doctor blading, while extremely simple, has many benefits that can make it competitive with more advanced techniques. Most importantly, the apparatus is extremely inexpensive and easy to use. Even automatic doctor blading machines suitable for production cost only several thousand dollars. Doctor blading is also a very simple technique. The manual process involves simply sliding the blade over the film, and the automatic machine has very few variables to set. The most difficult part is obtaining the correct type of slurry, a mostly trial-and-error process, that once found, can be easily replicated. Since there is no heating and no vacuums or beams, the phosphor crystals will not be

damaged or destroyed. The uniformity can be comparable with other more advanced techniques, and the thickness is easily controllable.

6.1.2 Description of Apparatus

The manual apparatus in its simplest form consists of a high-precision bar of metal, with micrometers to adjust the distance off the surface (see Figure 29). The device to be coated is spread with the slurry and the doctor blade apparatus is drawn over top of the device, leaving a uniform film. Constant speed and pressure must be used, as they have an impact of the final coating thickness. This device costs several hundred dollars, and works well for initial experimentation, however repeatable results are difficult to achieve due to human error.

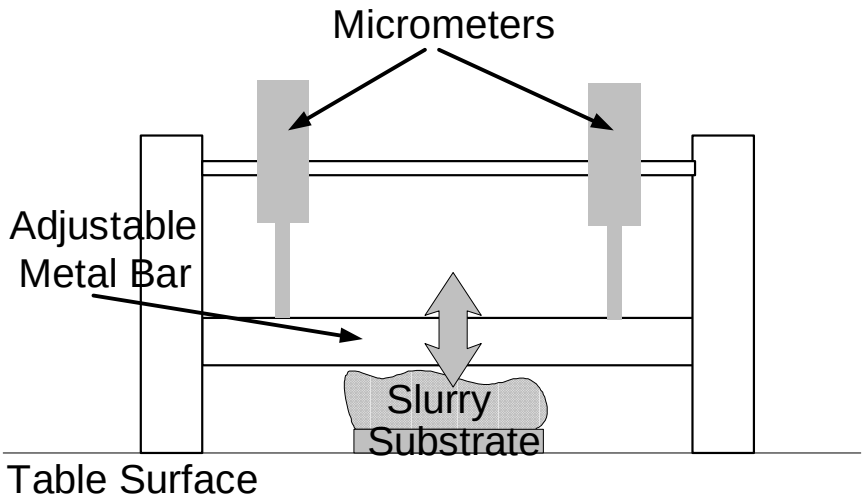

Figure 29 – Schematic of manual Doctor Blading Device

The automated apparatus looks like a plotter. It has a high precision metal bar attached to a motor. The device to be coated has the slurry applied,

then the blade is drawn over the device by the motor. The speed, height and pressure are all selectable. This device costs one to two thousand dollars, and provides repeatable results, since both the speed and pressure are constant, and human error is removed.

Both of these apparatus use "batch casting", since the doctor blade itself moves over the stationary substrate. For mass production, a continuous process is better, where the slurry is cast on a substrate that moves below the doctor blade. This has the same adjustable parameters as the automated apparatus, however many more devices can be coated using this approach (Figure 30).

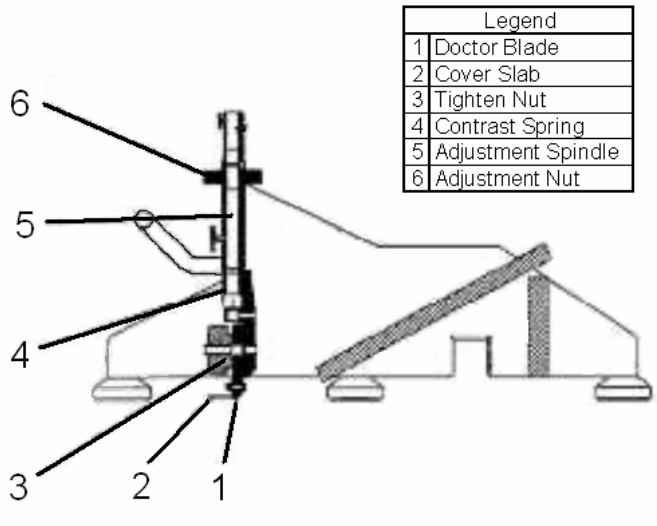

Figure 30 – Schematic of Continuous Doctor Blading Machine [8]

6.1.3 Slurry

Inorganic phosphor crystals are insoluble in almost every material, so there are a wide variety of chemicals one can use to make up the slurry. In general, evaporating pastes are made of a volatile liquid (such as an organic solvent), with an added “gelling agent” to raise the viscosity. The gelling agent will not evaporate, and will therefore be left behind as a residue. However gelling

agents are typically less than 5% of the total mass of the gel, so the residue can be minimized. The phosphor crystals are mixed with the gel to form the slurry. A plastisizer is sometimes necessary to hold the phosphor together once the gel has evaporated. If the phosphor crumbles off the substrate, using increasing amounts of plastic will prevent this, but may also reduce the effectiveness of the coating (by lowering the density of phosphor in the coating).

6.1.4 Input Variables

The slurry casting rate, V_p, is the relative velocity for the "scraping off" of the excess slurry. Typical values range from 8 to 18 mm/s [6]. The height of the doctor blade above the substrate surface is represented by H_t. Typical values are 0.4 to 2.0 mm [6], and these tend to produce films in the 10 to 100 micron range. D_p is the mean particle diameter. Although there is a distribution of sizes in the diameter of the phosphor crystals, it is unnecessary to take this into account, since it will be shown that the mean particle size does not have much impact on the results.

6.1.5 Output Variables

The primary output variable we are looking to control is the film thickness, S. This cannot be predicted using the variables above, since it is largely a function of the slurry properties. However, we can see how the different parameters can affect the final thickness. The doctor blade height H_t is the primary way to control the thickness of the final film. A greater amount of material on top of the substrate will mean more phosphor once the organic compounds have evaporated. The casting rate will also affect the final thickness of the film. A greater casting rate will create more "compression" of the slurry, creating a

thinner film. A plot of V_p, H_t and S is shown below in Figure 31 for a SiC thin film. Although SiC is not a phosphor, the properties for doctor blading are the same.

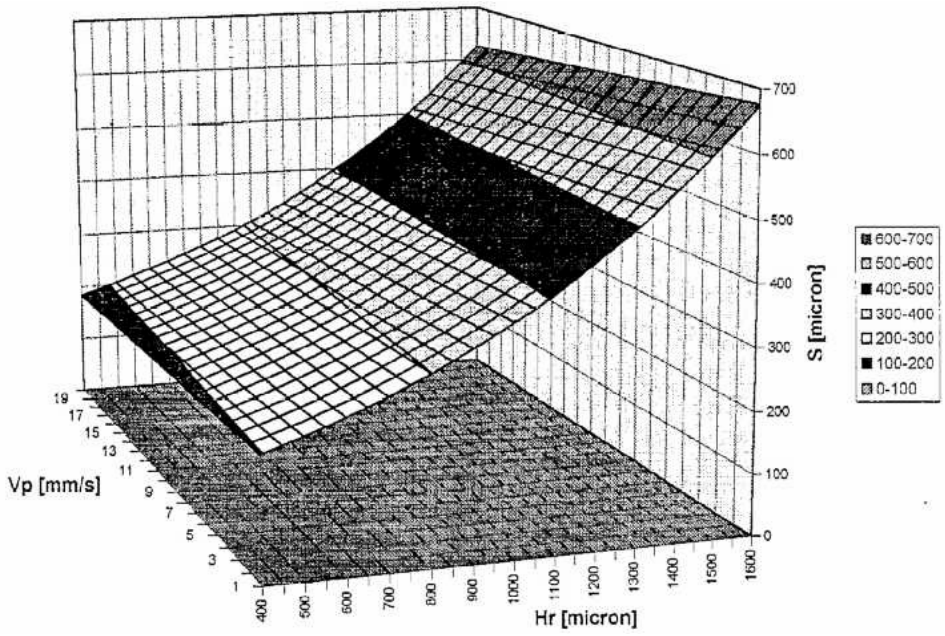

Figure 31 - Film Thickness (S) as a function of initial slurry thickness (Hr) and casting rate (Vp), for SiC thin film [8]

The mean particle diameter D_p has no effect on the thickness of the film, unless the thickness of the film approaches D_p. In this case, the film can't be made thinner than the diameter of the particles without destroying them. The quality of the film also becomes extremely poor at thicknesses around D_p, since there is only a single layer of particles on the substrate, and the thickness will vary significantly.

Other than the height of the film, the quality is also critical. This is difficult to accurately quantify, and it is usually measured by determining how well the coated device performs, rather than directly examining the coating. For example, one might coat an image sensor with phosphor, then examine the performance of the sensor to judge the quality of the film. However, to observe

only the film quality, one can examine the porosimetric characteristics. There are two variables here: the porosity θ, which is the number of pores or "holes" in the film in a unit of area, and the mean pore radius R_p, which is the average size of those holes. However, the values of the casting speed and the mean particle diameter do not significantly influence θ or R_p [7]. A thicker or thinner film may affect the quality, but this would depend on the specific situation and no general trends exist for blade height. So the only variable to control the quality is the slurry. In general, if there is a high percentage of evaporating material, a porous, uneven film will result. If the slurry is mostly phosphor a denser, more uniform coating will result. The goal with the slurry is to make the viscosity high enough that it hold its shape while it dries, while keeping the phosphor concentration as high as possible. Figure 32 shows SEM photographs of a phosphor coating where the slurry had different concentrations of phosphor. Table 3 shows a summary of all the variables involved in doctor blading, and how they affect the outcome.

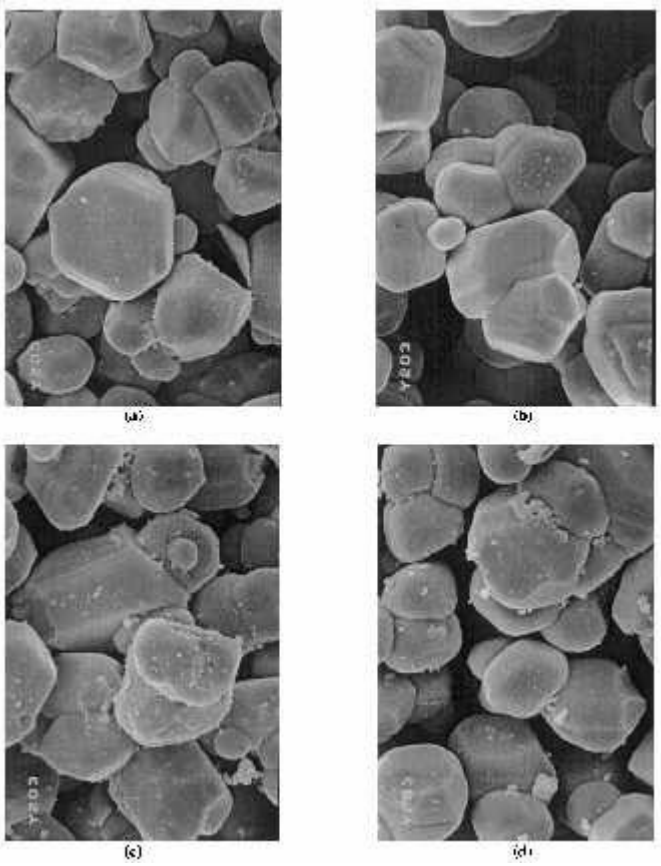

Figure 32 - SEM Photographs of Y_2O_3 phosphor concentration in the slurry of (a) 0.1 wt.%, (b) 0.5wt.%, (c) 1.0 wt.%, and (d) 2.0wt.% [11]

Table 3 – Relationships between Input and Output Variables for Doctor Blading

Output Variables	Input Variables			
	Slurry Casting Rate V_p	Blade Height above Substrate H_t	Mean Particle Diameter D_p	Slurry Composition
Film Thickness S	**Decreases** with increasing V_p	**Increases** with increasing Ht	No effect	**Increases** with increasing phosphor concentration
Porosity θ	No effect	No effect	No effect	**Decreases** with increasing phosphor concentration

Mean pore radius R_p	No effect	No effect	No effect	Can change with phosphor size, density, (many other factors)

6.2 Experimental Setup

6.2.1 Gel Selection

The most difficult part of Doctor Blading, and the part that gives rise to the most problems (non-uniformity, non-repeatability), involves the preparation of the gel. The selection of the evaporating paste was quite difficult. The requirements are that it evaporate away completely, and that it have the necessary viscosity to suspend the phosphor in place during the doctor blading process. No gels could be found that evaporated without leaving residue, the only option was to find a "gelling agent" that could be added to water, alcohol or an organic solvent, to raise the viscosity. The gelling agent would not evaporate, but it was hoped the gel could be prepared with a very small (<5%) proportion of gelling agent. Various gelling agents from different sources were used, but the amount of gelling agent needed to obtain the necessary viscosity was too high. Therefore the higher amounts of residue (which was, in all cases, not transparent to UV) would interfere with the coating. Finally, various prepared gels were tried, such as hand sanitizer and aloe vera moisturizer. A measured amount of gel was placed in a clean, dry container, and stirred using a magnetic pellet to speed up evaporation. No heat was applied. The container was weighed every 4 hours. Once there had been less than a 1% change over 4 hours, the final weight was recorded. The results are shown in Table 4.

Table 4 – Results from Prepared Gel Evaporation Experiments

Name of Product	Supplier	Initial weight	Final weight	% left after evaporation
Purell Hand Sanitizer	Local Drugstore – off the shelf	10.056g	0.097g	0.96%
Rexell Vitamin E Gel	Local Drugstore – off the shelf	8.046g	0.526g	6.54%
MediFlo	Local Drugstore – from pharmacist, special order	15.510g	6.495g	41.88%
Band-Aid Anti-itch gel	Local Drugstore – off the shelf	10.744g	1.543g	14.36%
President's Choice Hand Sanitizer	Supermarket	10.142g	0.287g	2.83%

It was found that Purell Hand Sanitizer evaporated leaving only 0.96% of its mass behind – much less than any of the advertised gelling agents. This was a consumer product, made of water, alcohol, gelling agent, and some fragrances and moisturizers. If the gelling agent alone could be obtained, the percentage of material left behind could be lowered further. Unfortunately such a substance could not be found at any chemical company, and the manufacturers of the products were unwilling to divulge their formula.

6.2.2 Thickness Calculation

The final "dry" thickness of the coating is a function of slurry composition, and the initial "wet" thickness. First, the density of the phosphor in air must be calculated. This value, $D_{phosphor\_in\_air}$, with units of [mass/volume], was calculated by weighing 10mL of phosphor.

The density of phosphor in the phosphor/gel slurry mixture is much less, however. This value, $D_{phosphor\_in\_slurry}$, with units of [mass/volume], is

calculated by dividing the weight of phosphor that was added to the gel, by the total volume of the phosphor/gel slurry mixture.

In order to find the final thickness, one must first find the weight of phosphor deposited per unit area. If t_{wet} is the thickness of the slurry as deposited on the substrate, the weight of the phosphor (per unit area) is:

$$Weight\_of\_Phosphor = t_{wet} \times D_{phosphor\_in\_slurry} \quad \textbf{(Equation 14)}$$

The volume that this weight of phosphor takes up can be found from $D_{phosphor\_in\_air}$, so the height of phosphor is:

$$t_{dry} = \frac{Weight\_of\_Phosphor}{D_{phosphor\_in\_air}} \quad \textbf{(Equation 15)}$$

Substituting Equation 14 into Equation 15, we have the final equation for the final (dry) thickness:

$$t_{dry} = \frac{t_{wet} \times D_{phosphor\_in\_slurry}}{D_{phosphor\_in\_air}} \quad \textbf{(Equation 16)}$$

This is assuming that all of the gel will evaporate; since only 0.96% of the mass of the gel will remain as solid residue, this introduces very little error.

6.2.3 Slurry Preparation

The first time the doctor blading experiment was tried, the measured amount of gel was placed in a glass container, and the measured amount of phosphor was put on top of the gel. It was mixed using a magnetic pellet, for five minutes, and then spread onto the substrate. This yielded a coating with large clumps of phosphor, on the order of 1mm in diameter. Several attempts were made, each time changing the mixing process and visually inspecting the slurry on a glass slide to see if it was mixed. Eventually, a procedure was devised that created the most uniform slurry mixture.

The gel was put into a clean glass container, and stirring began. The phosphor was measured and added slowly to the gel through a 250μm screen which would filter out any clumps larger than that. As the phosphor fell onto the gel, it would become stirred into the mixture and would not have as much chance to clump as it would if it were added all at once. A bit of phosphor remained on the screen, so the screen was weighed before and after, and the amount of phosphor adjusted accordingly. The slurry was then mixed on high speed for 60 minutes, with the container sealed to reduce evaporation of the gel. The slurry was placed on the sensors and scraped off with the doctor blade to the precise thickness as quickly as possible, to prevent settling and evaporation.

6.2.4 2212 Sample Preparation

First, 20mL of 2212 phosphor was placed in a glass jar and weighed. The mass was 35.591g, therefore the density of phosphor is 1.7796 g/mL. In order to have enough for all the coatings, it was decided to make up 30mL of slurry. Although it makes coating easier and more accurate to have as little phosphor in the slurry as possible (then the initial wet thickness can be made much larger),

this also increases the amount of residue. Because of the minimum and maximum heights of the doctor blade used, the phosphor concentration was set such that there would be 10 times more phosphor left at the end than residue from the gel. The density of the gel was measured, and it was determined that 0.1454g of the gel residue would be left. Therefore there should be 1.5g of phosphor in the slurry. This gave a density of phosphor in the slurry of 0.05g/mL.

Using Equation 16, the initial wet thickness needed for a given final (dry) thickness was calculated for all desired results. The results are shown in Table 5.

Table 5 – Final (dry) film thickness vs. Initial (wet) slurry thickness for Doctor Blade coating using 2212 Phosphor

Final thickness Desired (μm)	Initial (wet) slurry thickness (μm)
10	365
15	534
20	711
25	890
30	1068

The thickness of the coatings on the sensors cannot be measured, nor can the actual coating be examined. So three slides were coated, with an expected final thickness of 15μm, 20μm and 30μm. Cross-section pictures were taken with an SEM, shown in Figure 33.

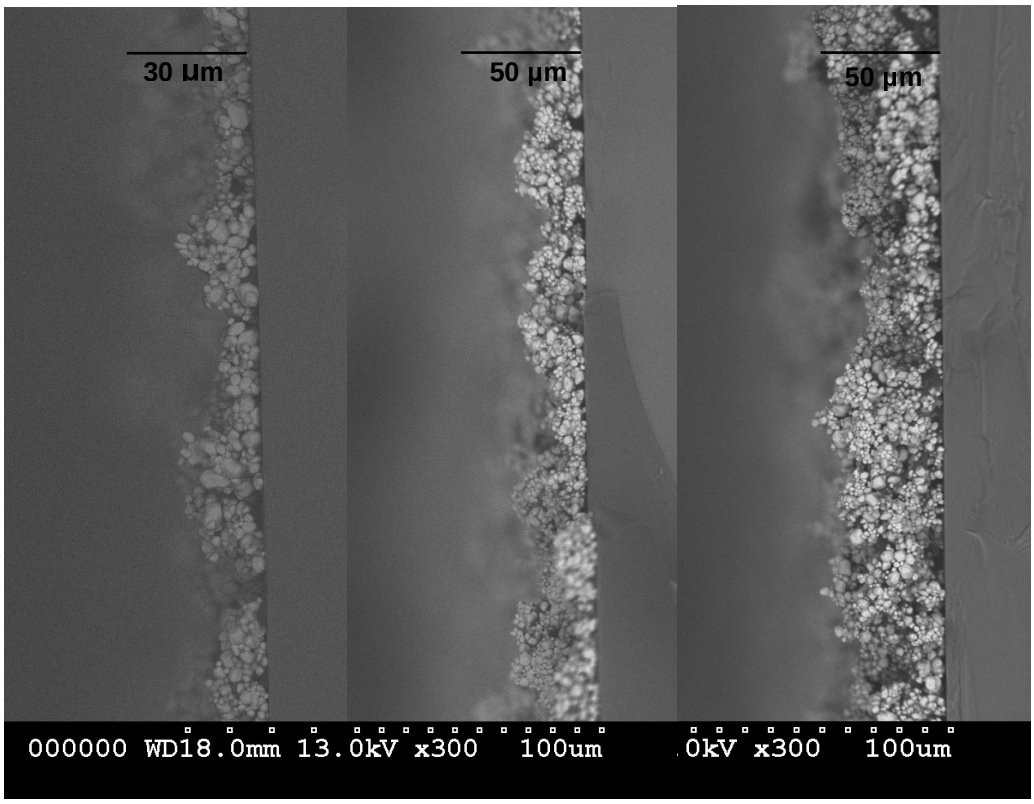

Figure 33 – SEM Cross-section of glass slides coated with 2212 phosphor using Doctor-Blade Method, with a target thickness of 15µm, 20µm and 30µm, respectively

As can be seen, the thin coating (targeted at 15µm) ended up having a mean thickness of approximately 15µm, with an estimated standard deviation of 3µm. The medium coating (targeted at 20µm) ended up having an approximate mean thickness of 18µm, with an estimated standard deviation of 6µm. The thickest coating (targeted at 30µm) resulted in an approximate mean thickness of 25µm, with an estimated standard deviation of 10µm. Therefore the thickness calculation of the slurry is verified to within 17%, since it deposited the correct amount of material (to within 17%) on the surface. The non-uniformity of the coating makes this difficult to measure exactly, however.

Figure 34, Figure 35 and Figure 36 show the top of the coating, for the three different thicknesses.

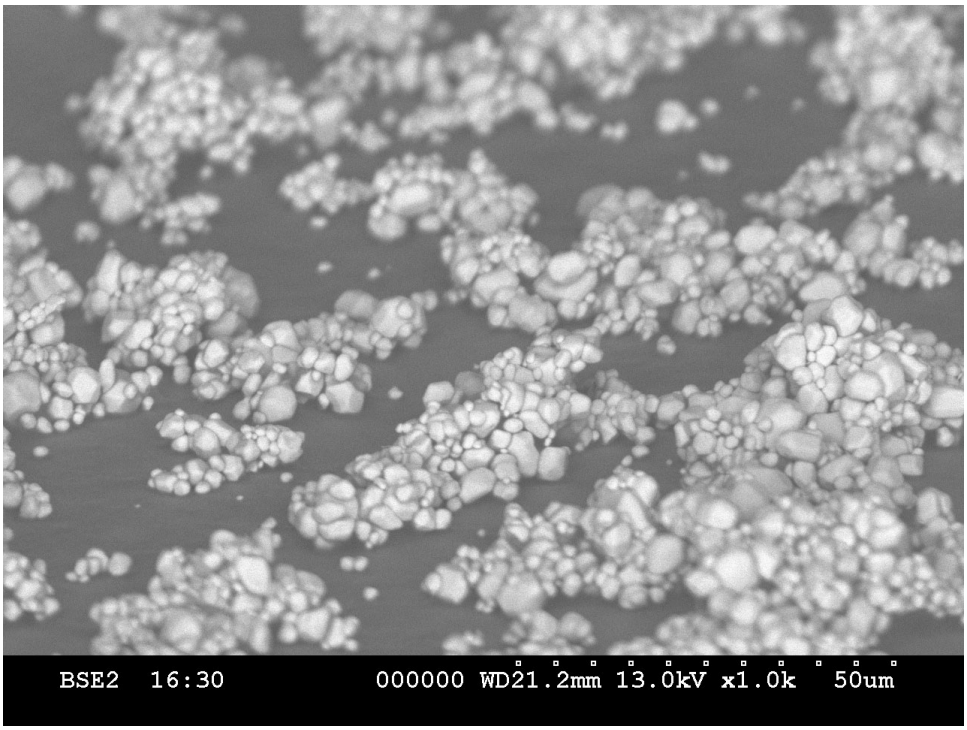

Figure 34 - Overhead SEM photograph of Doctor Blade coated 2212 phosphor coating on glass slide, thin coating, showing clustering and approximately 50% uncoated area

Although it is easier to see the depth profile of the coating from the cross section, the top view gives a reasonable indication of the coverage. From Figure 34 showing the thinnest coating, it can be seen that the phosphor is in clusters, covering approximately half of the total surface area. It would seem more likely that the phosphor would be distributed more evenly across the surface, instead of piling up in some spots and leaving other spots vacant. There are two main reasons why the phosphor would form clusters instead of spreading evenly. First, the phosphor would have been in clusters when coated – in fact the first attempts at Doctor Blading were unsuccessful because of this

reason. More mixing or different mixing methods may help with this. As well, the evaporating paste in the coating would not evaporate completely evenly, and near the end of the drying process there were areas with "wet" gel remaining, and areas that were completely "dry". A reasonable explanation is that the surface tension could have pulled the phosphor into clusters.

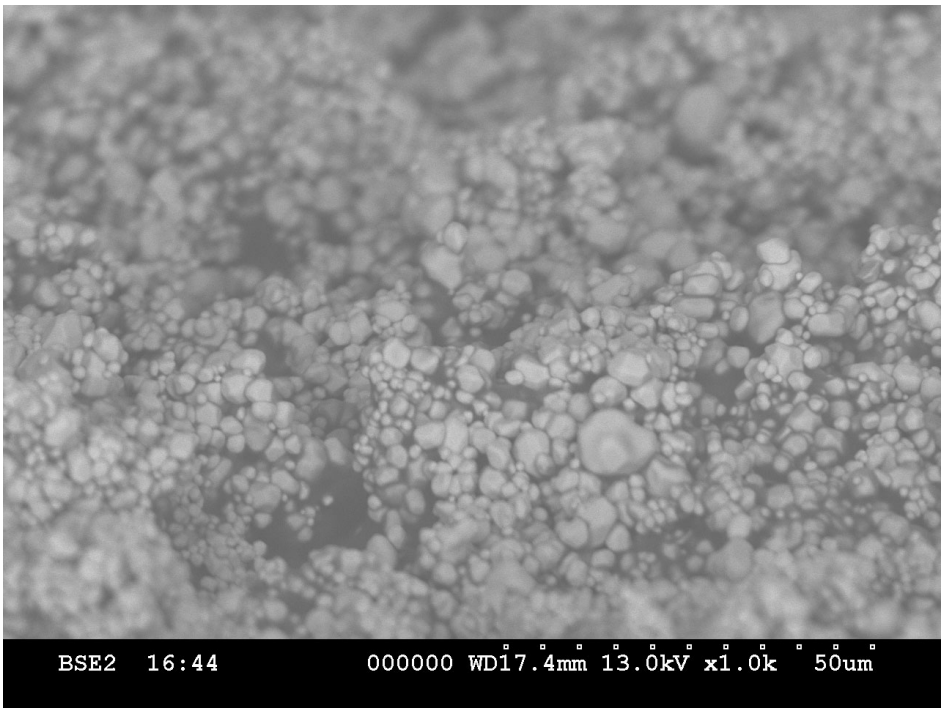

Figure 35 - Overhead SEM photograph of Doctor Blade coated 2212 phosphor coating on glass slide, medium coating, showing clustering and approximately 25% uncoated area

The medium coating shows more coverage, but there are still bare spots covering approximately 25% of the surface.

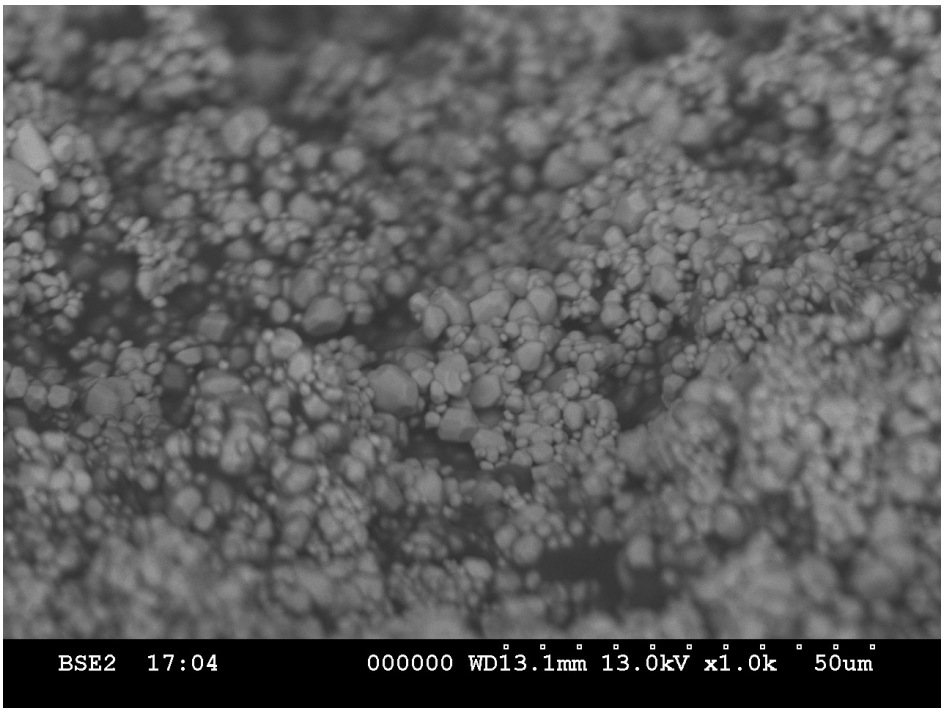

Figure 36 - Overhead SEM photograph of Doctor Blade coated 2212 phosphor coating on glass slide, thick coating, showing clustering and full coverage of surface area

The thickest coating shows full coverage, with no bare substrate visible in the picture. This fits in with the idea that clustering during mixing and surface tension are causing the non-uniformity in the thickness of the coating. With more phosphor, there are more clusters so they can coat the surface more evenly. As well, the surface tension does not have the force necessary to create bare patches on the substrate, however it still causes clustering of the phosphor.

6.2.5 2345 Sample Preparation

The sample was prepared in the same manner as the 2212 sample in Section 6.2.4. The density of phosphor is 0.8904 g/mL . Again, for 30mL of slurry there would have to be at least 1.5g of phosphor to achieve the ratio of 10 times

more phosphor than residue. However, this was not possible, since the distance from the sensor die to the top of the ceramic package (the minimum wet thickness achievable) was too large to create the necessary 15μm coating. So the amount of phosphor was halved, there was 0.75g of phosphor in the slurry, so the density of phosphor in slurry was 0.025g/mL.

Using Equation 16, the initial wet thickness needed for a given final (dry) thickness was calculated for all desired results. The results are shown in Table 6.

Table 6 - Final (dry) film thickness vs. Initial (wet) slurry thickness for Doctor Blade coating using 2345 Phosphor

Final thickness Desired (μm)	Initial (wet) slurry thickness (μm)
10	365
15	534
20	711
25	890
30	1068

Since the density of 2345 phosphor is almost exactly half that of the 2212 phosphor, but half as much phosphor was used, the necessary wet coating thickness coincidentally is equal to that of the 2212 phosphor.

The thickness of the coatings on the sensors cannot be measured, nor can the actual coating be examined. So three slides were coated, with an expected final thickness of 15μm, 20μm and 30μm. Cross-section pictures were taken with an SEM, shown in Figure 37.

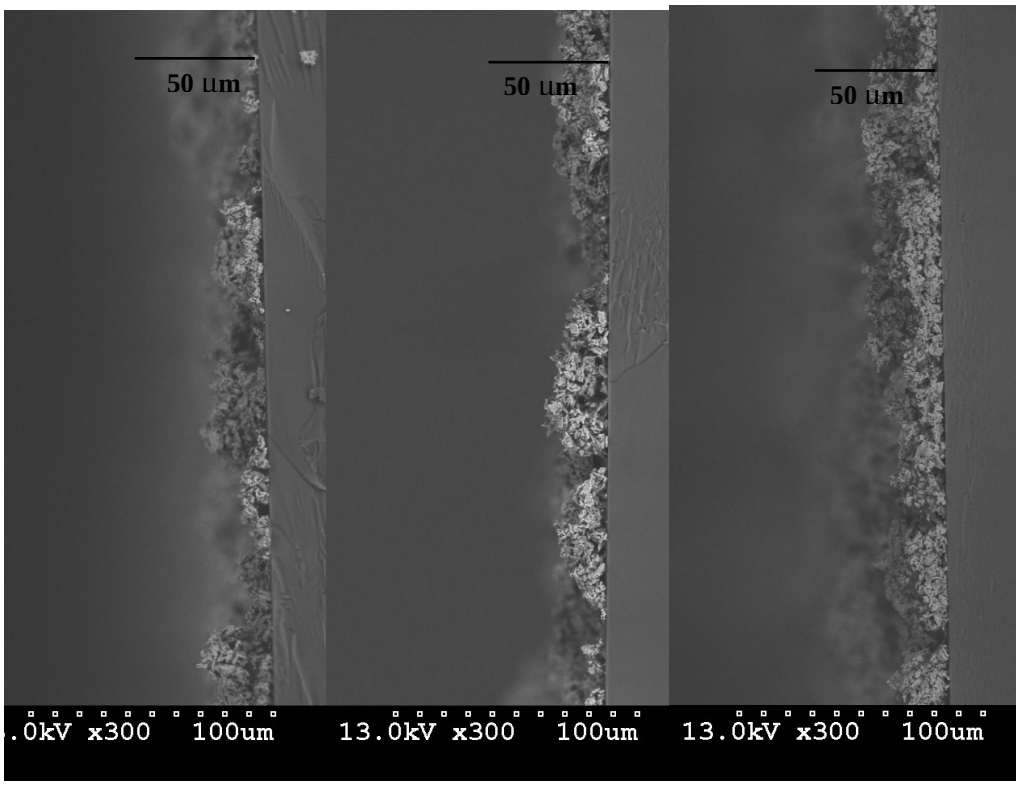

Figure 37 – SEM Cross-section of glass slides coated with 2345 phosphor using Doctor-Blade Method, with a target thickness of 15µm, 20µm and 30µm, respectively

The 2345 phosphor coating is more non-uniform that the previous 2212 phosphor coating. The clusters and bare patches make it difficult to judge the exact mean thickness and standard deviation, although estimates can be provided, based on many SEM photographs. The thin coating (targeted at 15µm) has some very thick clusters, as much as 30µm. However careful examination shows a mean thickness of approximately 15µm, with an estimated standard deviation of 3µm. The medium coating (targeted at 20µm) has an approximate mean thickness of 20µm, with an estimated standard deviation of 10µm. The thickest coating (targeted at 30µm) resulted in an approximate mean thickness of 25µm, with an estimated standard deviation of 10µm. Therefore the thickness calculation of the slurry is verified to within 17% (the same as for

the 2212 phosphor coating), since it deposited the correct amount of material (to within 17%) on the surface.

Figure 38, Figure 39 and Figure 40 show the surface of the coatings.

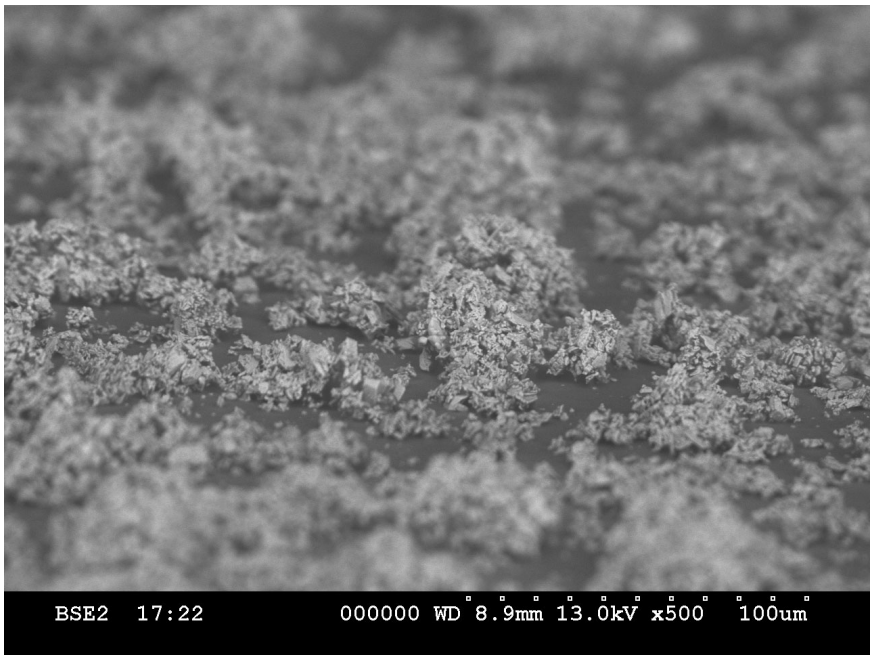

Figure 38 - Overhead SEM photograph of Doctor Blade coated 2345 phosphor coating on glass slide, thin coating, showing clustering and approximately 50% uncoated area

The thinnest coating, like the 2212-coated slides, is very uneven, with approximately 50% bare spots. There are many places where the phosphor has clustered together. The reason for this is the same as with the 2212 phosphor, clustering of the phosphor during mixing, and surface tension while drying.

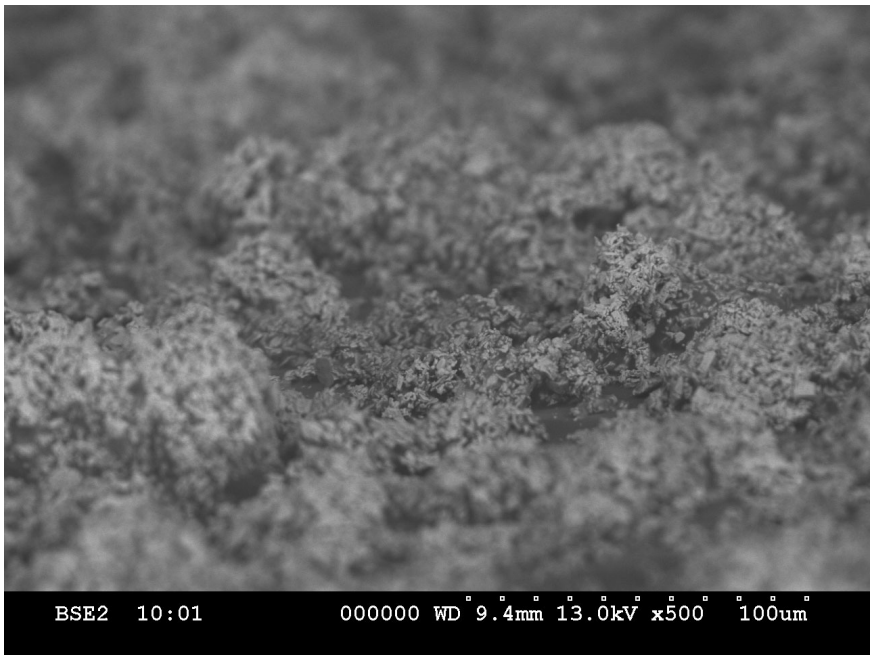

Figure 39 - Overhead SEM photograph of Doctor Blade coated 2345 phosphor coating on glass slide, medium coating, showing clustering and approximately 25% uncoated area

The medium coating of 2345 phosphor shows great non-uniformity, with approximately 75% coverage.

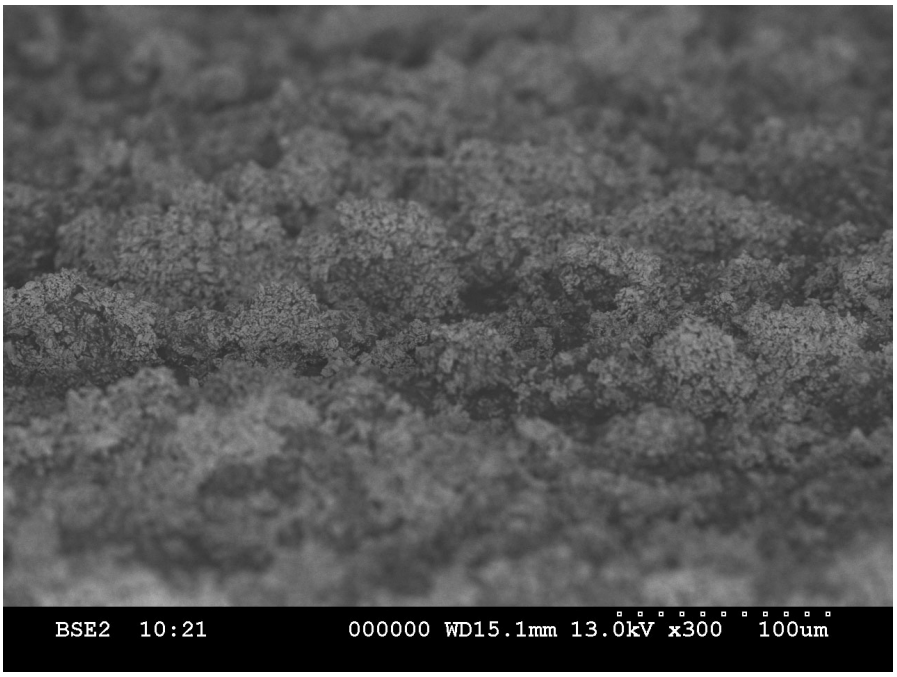

Figure 40 - Overhead SEM photograph of Doctor Blade coated 2345 phosphor coating on glass slide, thick coating, showing clustering and full coverage of surface area

Finally, the thickest 2345 coating shows full coverage, but still many large clusters.

The residue left behind by the evaporating gel was not visible in most of the photos, however Figure 41 shows a large (20μm by 60μm) clump of residue, easily noticeable due to its smooth texture and shape, versus the more jagged appearance of the phosphor.

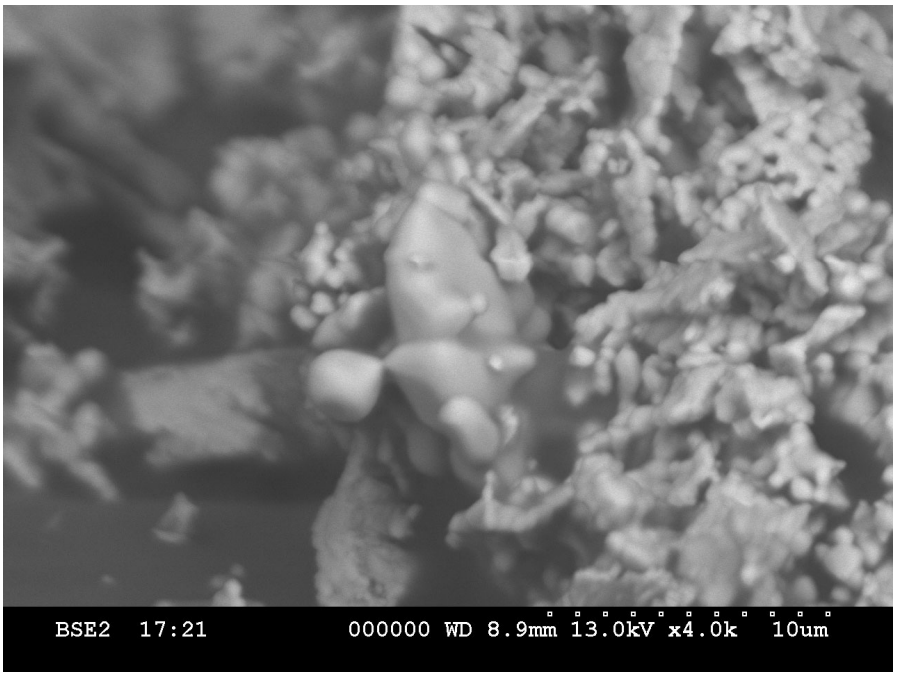

Figure 41 – SEM photograph of Doctor Blade coated 2345 phosphor coating on glass slide, thin coating, showing solid residue from evaporating gel

It is assumed that most of the residue formed clumps like this, and also filled in the smaller areas between the phosphor, smoothing out the appearance of the phosphor slightly.

6.3 Experimental Results

6.3.1 QE Results – 2212 Phosphor

Three sensors were coated with 2212 phosphor using the Doctor Blading method described in Section 5.2, with three different thicknesses. They were tested for QE in the manner described in Section 3.1.1. The results for the three different thicknesses are shown in Figure 42.

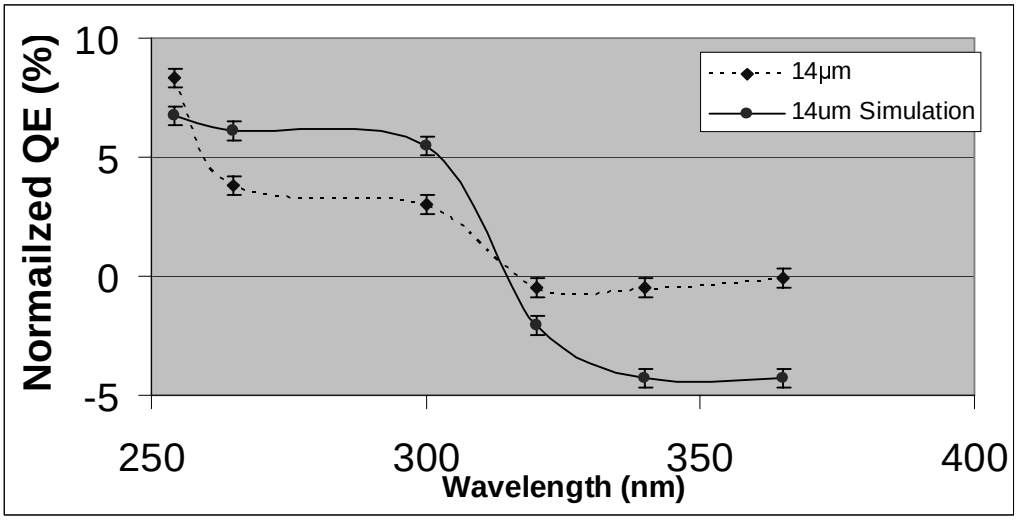

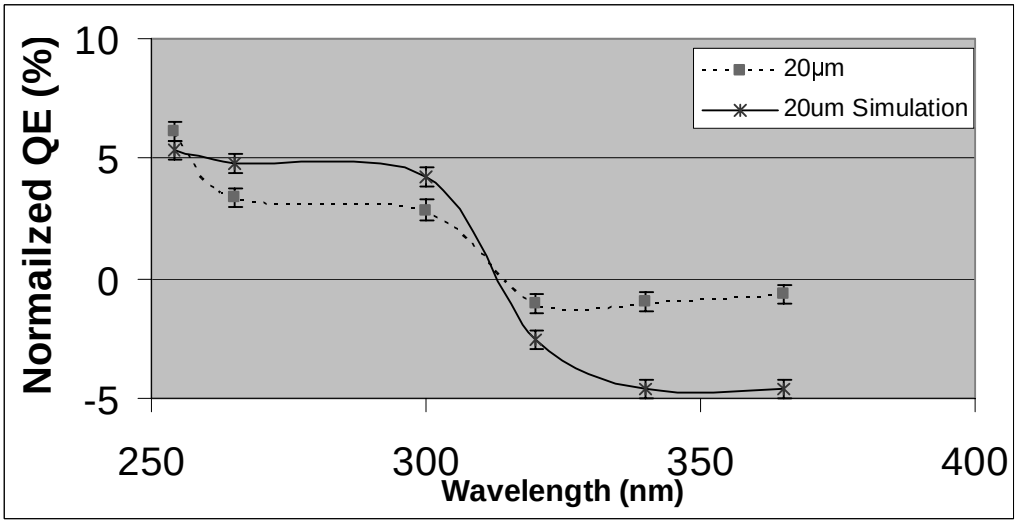

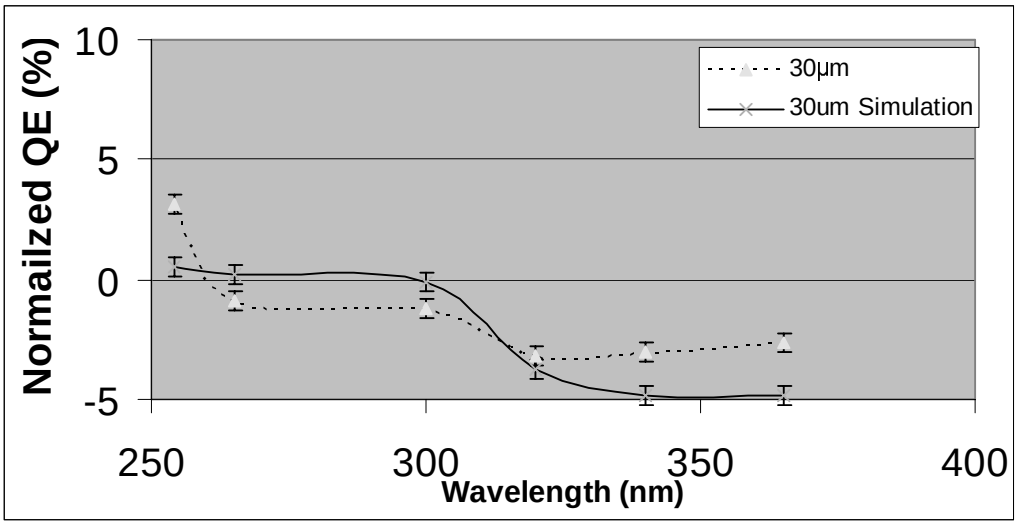

Figure 42 - QE Spectrum of Doctor Blade coated 2212 phosphor coating on DALSA IA-D1-0256 Sensor, thin (top), medium (middle) and thick (bottom) coatings

The shape of the QE spectrum for all three coatings was very similar. The peak QE is at 254nm, a large drop at 265nm, then another large drop at 320nm, where all three coatings actually reduce the QE below the uncoated level. All three coatings had a peak QE at 254nm. The results at 254nm for all 3 sensors coated with 2212 phosphor are shown below in Table 7.

Table 7 - Summary of QE Results at 254nm for DALSA IA-D1-0256 Sensors coated with 2212 phosphor using Doctor Blade Method

Coating Thickness	Uncoated QE (%) *(Simulated)*	Coated QE (%) *(Simulated)*	% Increase *(Simulated)*
Thin	5.3 *(5.0)*	13.6 *(11.7)*	158 *(134)*
Medium	5.3 *(5.0)*	11.4 *(10.3)*	117 *(106)*
Thick	4.6 *(5.0)*	7.7 *(5.5)*	37 *(10)*

The simulation, in all 3 cases, follows the same general trend as the experimental results, including the optimum coating thickness of 14μm. However the shape is slightly different. Discussion of the results and simulation will follow in Section 6.4.1.

6.3.2 QE Results – 2345 Phosphor

Three sensors were coated with 2345 phosphor using the Doctor Blade method described in Section 5.2, with 3 different thicknesses. They were tested for QE in the manner described in Section 3.1.1. The results are shown in Figure 43.

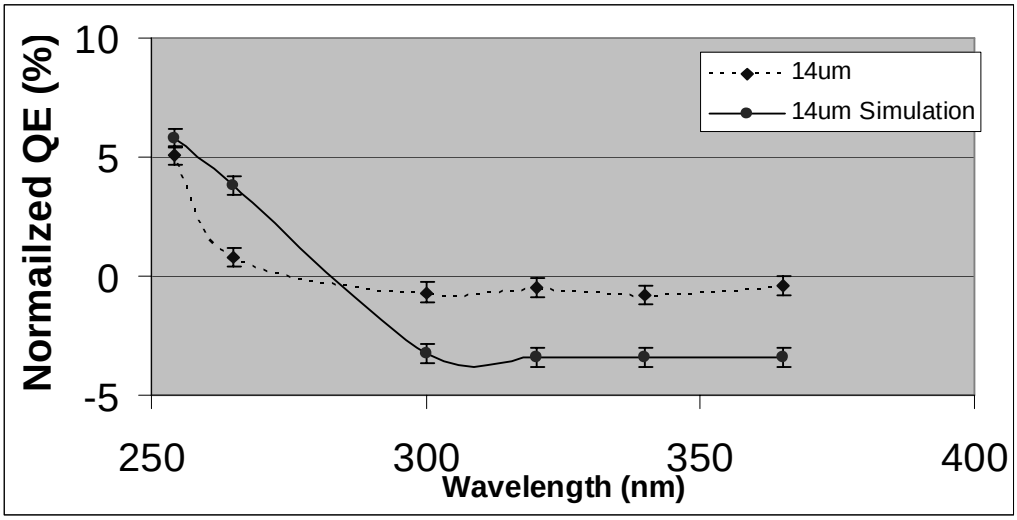

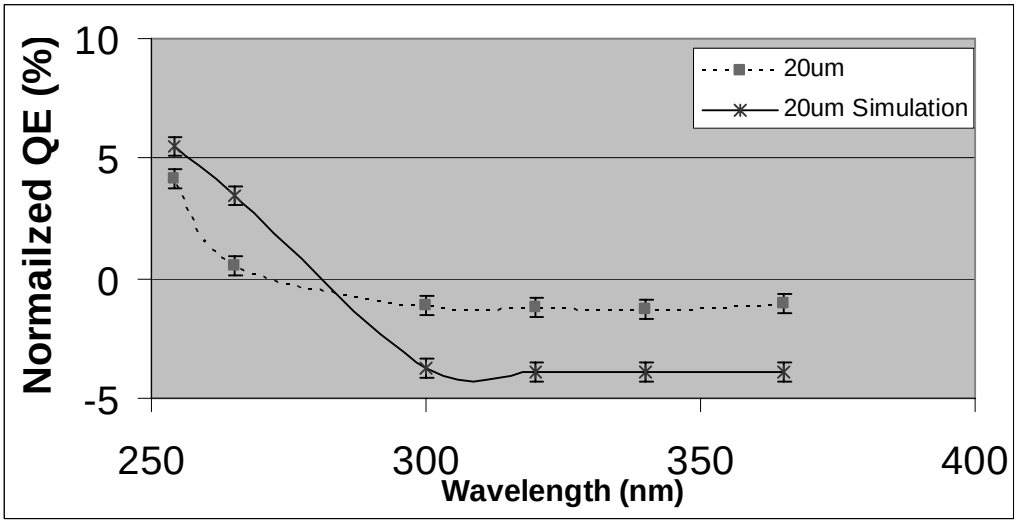

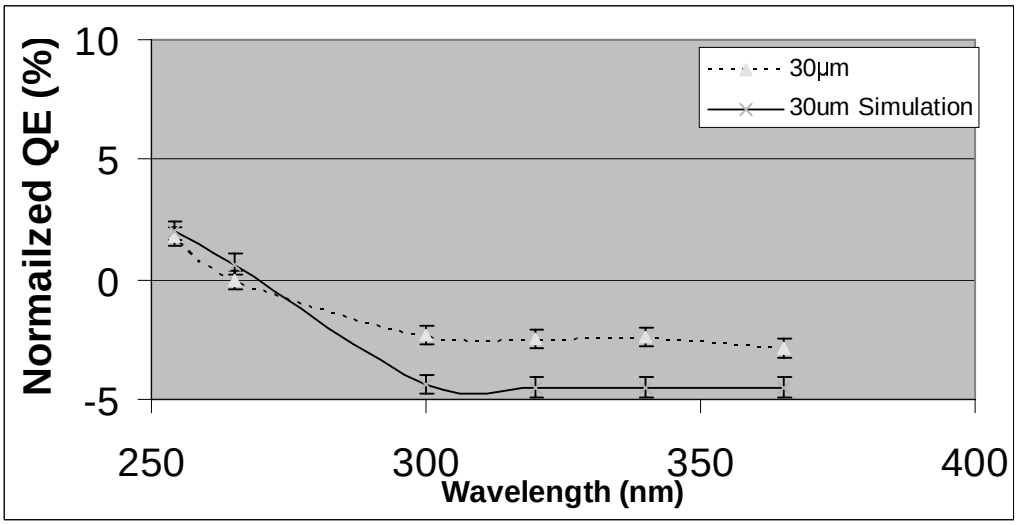

Figure 43 - QE Spectrum of Doctor Blade coated 2345 phosphor coating on DALSA IA-D1-0256 Sensor, thin (top), medium (middle) and thick (bottom) coatings

All three of the coating thicknesses followed the same general trend. The peak QE was at 254nm, vastly reduced at 265nm, and actually going below the QE of the uncoated sensors at wavelengths over 300nm. The results at 254nm for all 3 sensors coated with 2212 phosphor are shown below in Table 8.

Table 8 - Summary of QE Results at 254nm for DALSA IA-D1-0256 Sensors coated with 2345 phosphor using Doctor Blade Method

Coating Thickness	Uncoated QE (%) *(Simulated)*	Coated QE (%) *(Simulated)*	% Increase *(Simulated)*
Thin	5.2 *(5.0)*	10.3 *(10.7)*	96 *(114)*
Medium	4.9 *(5.0)*	9.0 *(10.5)*	86 *(110)*
Thick	4.7 *(5.0)*	6.5 *(7.0)*	38 *(40)*

In all 3 cases, the simulation results followed the same general trend but the shape of the curve was slightly different. The simulation always predicted a higher QE at 265nm, and a much lower QE for the longer wavelengths.

6.3.3 PRNU Results - 2212 Phosphor

The three sensors coated with 2212 phosphor using the Doctor Blading method were tested for PRNU in the manner described in Section 3.1.2. The results of the PRNU test of all three sensors for 3 different wavelengths are shown in Figure 44, Figure 45 and Figure 46.

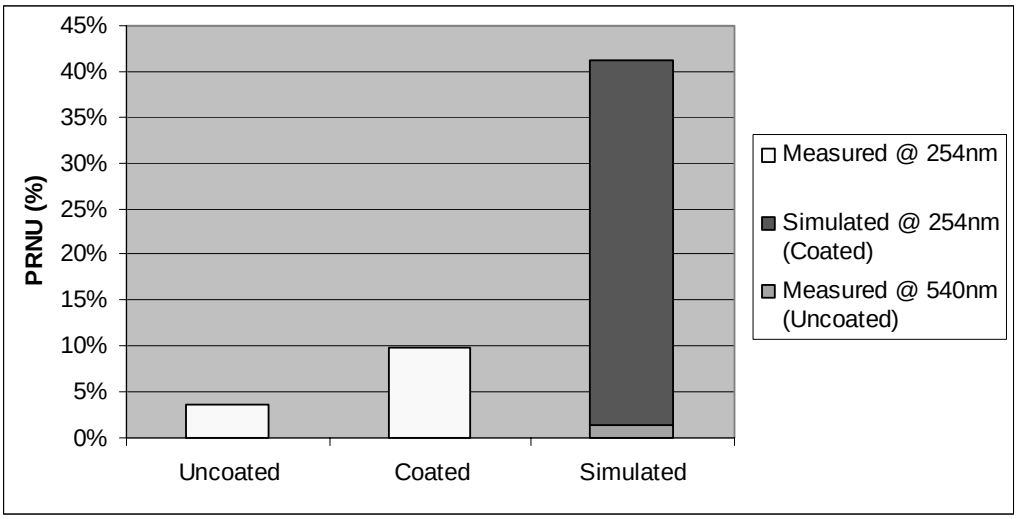

Figure 44 - Coated, Uncoated and Simulated PRNU at 254nm for Doctor Blade coated 2212 phosphor coating on DALSA IA-D1-0256 Sensor, Thin Coating

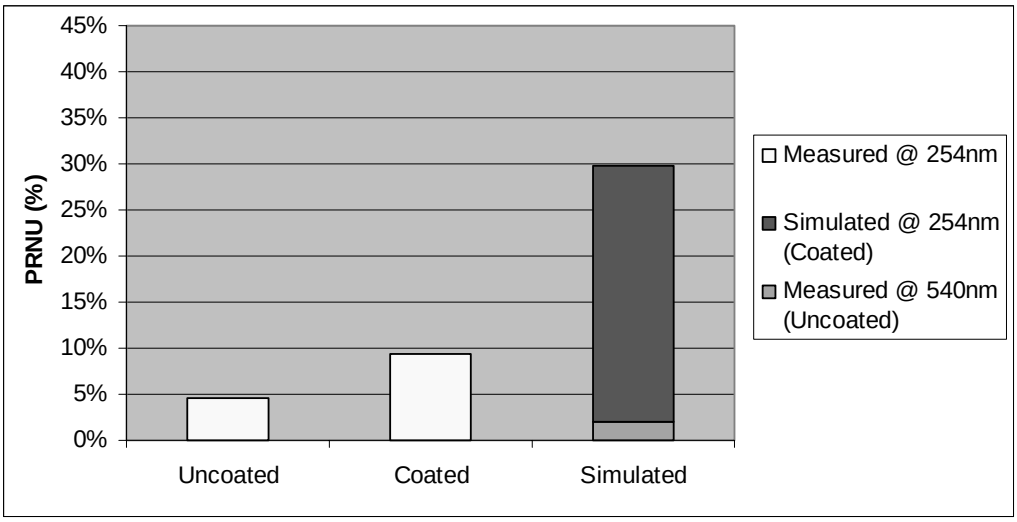

Figure 45 - Coated, Uncoated and Simulated PRNU at 254nm for Doctor Blade coated 2212 phosphor coating on DALSA IA-D1-0256 Sensor, Medium Coating

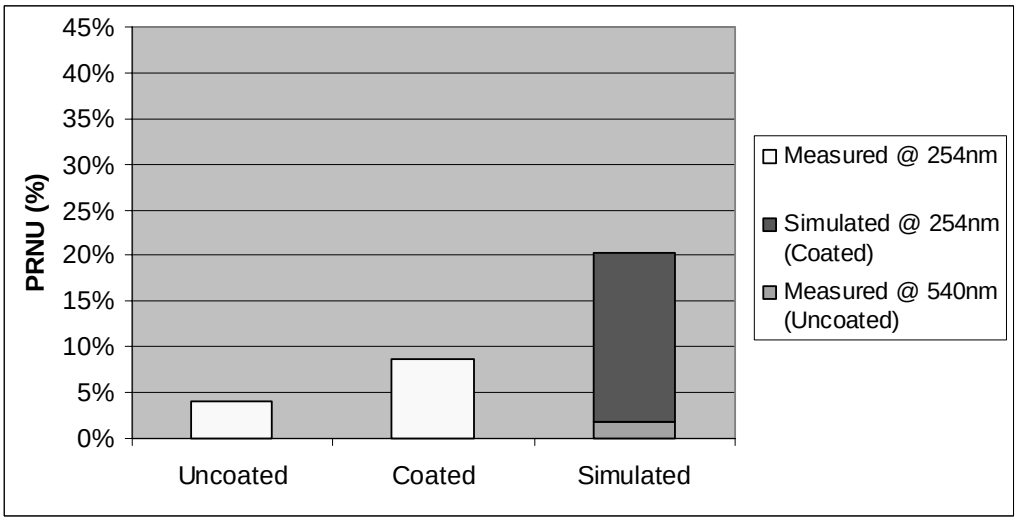

Figure 46 - Coated, Uncoated and Simulated PRNU at 254nm for Doctor Blade coated 2212 phosphor coating on DALSA IA-D1-0256 Sensor, Thick coating

For all three coatings, the trends were the same; an uncoated PRNU of 4-5%, due to the design of the sensor (this will be explained in Section 6.4). The coating increased the PRNU by a factor of 2-3, and the simulation predicted

a much higher degradation in PRNU than was measured. As before, the uncoated PRNU at 540nm was added to the simulation to represent the additional PRNU of the re-emitted photons moving into the sensor.

The results at 254nm for all 3 sensors coated with 2212 phosphor are shown below in Table 9.

Table 9 - Summary of PRNU Results at 254nm for DALSA IA-D1-0256 Sensors coated with 2212 phosphor using Doctor Blade Method

Coating Thickness	Uncoated PRNU (%)	Coated PRNU (%) *(Simulated)*	% Increase
Thin	3.6	9.8 *(41.3)*	173
Medium	4.5	9.4 *(29.9)*	119
Thick	4.0	8.6 *(18.3)*	111

Although the simulation was, in each case, much higher than the measured value, it accurately predicted that the thinnest coating would have the highest PRNU and the thickest one would have the lowest PRNU. Discussion of the results and simulation will follow in Section 6.4.3.

6.3.4 PRNU Results - 2345 Phosphor

The three sensors coated with 2345 phosphor using the Doctor Blading method were tested for PRNU in the manner described in Section 3.1.2. The results are presented below in Figure 47, Figure 48 and Figure 49.

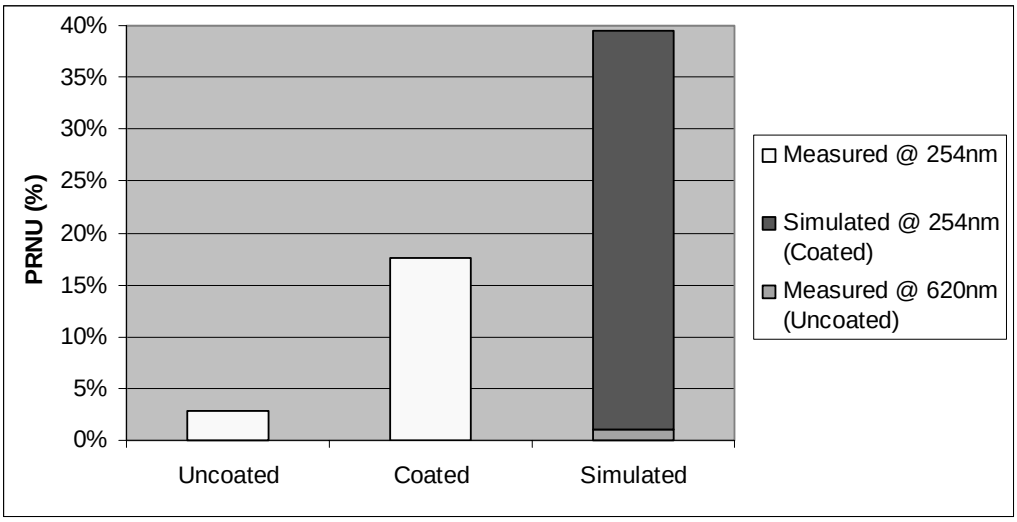

Figure 47 - Coated, Uncoated and Simulated PRNU at 254nm for Doctor Blade coated 2345 phosphor coating on DALSA IA-D1-0256 Sensor, Thin Coating

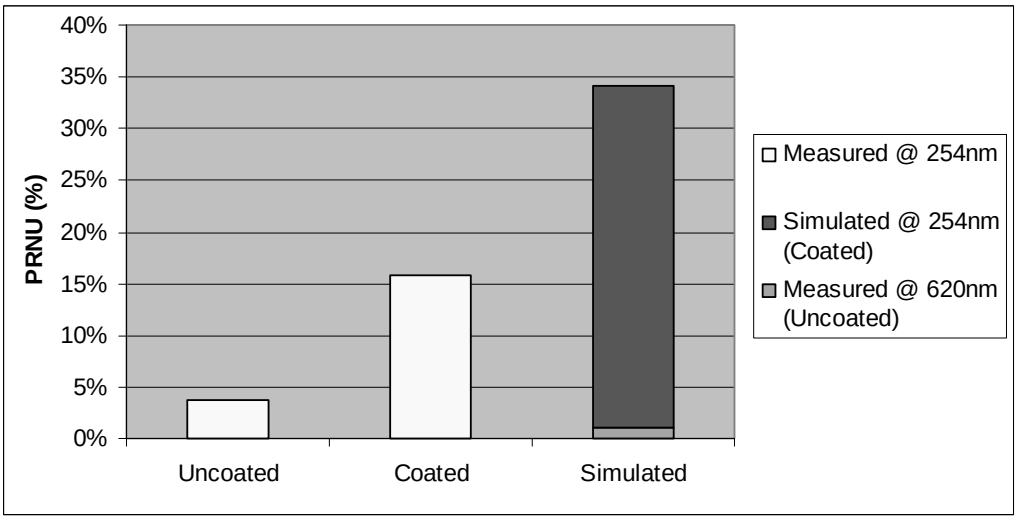

Figure 48 - Coated, Uncoated and Simulated PRNU at 254nm for Doctor Blade coated 2345 phosphor coating on DALSA IA-D1-0256 Sensor, Medium coating

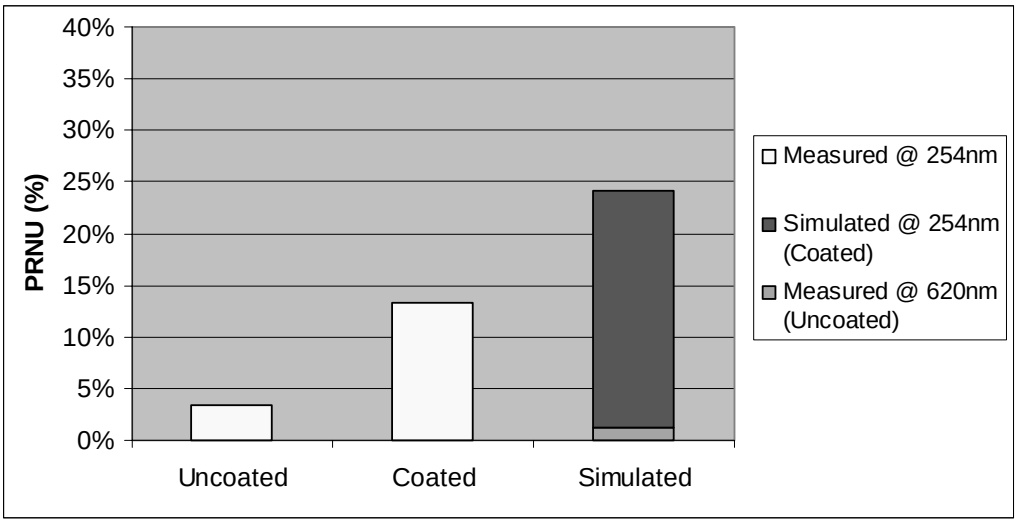

Figure 49 - Coated, Uncoated and Simulated PRNU at 254nm for Doctor Blade coated 2345 phosphor coating on DALSA IA-D1-0256 Sensor, Thick coating

All 3 sensors showed the same trend; an uncoated PRNU of 3-5%, a much higher Coated PRNU, and the simulation predicting an even higher PRNU. As predicted, and like the 2212-coated sensors, the thickest coating had the lowest PRNU, and the thinnest coating had the highest PRNU. The results at 254nm for all 3 sensors coated with 2345 phosphor are shown below in Table 10.

Table 10 - Summary of PRNU Results at 254nm for DALSA IA-D1-0256 Sensors coated with 2345 phosphor using Doctor Blade Method

Coating Thickness	Uncoated PRNU (%)	Coated PRNU (%) *(Simulated)*	% Increase
Thin	2.8	17.6 *(39.4)*	540
Medium	3.6	15.8 *(34.1)*	339
Thick	3.3	13.3 *(24.13)*	300

Again, the simulation predicted much higher PRNU results than were measured, but accurately predicted that the thinnest coating would have the worst PRNU, and the thickest coating the best.

6.3.5 CTF Results – 2212 Phosphor

The sensors coated with 2212 phosphor using the Doctor-Blade method were tested for CTF in the manner described in Section 3.3. The results are presented below in Figure 50, Figure 51 and Figure 52

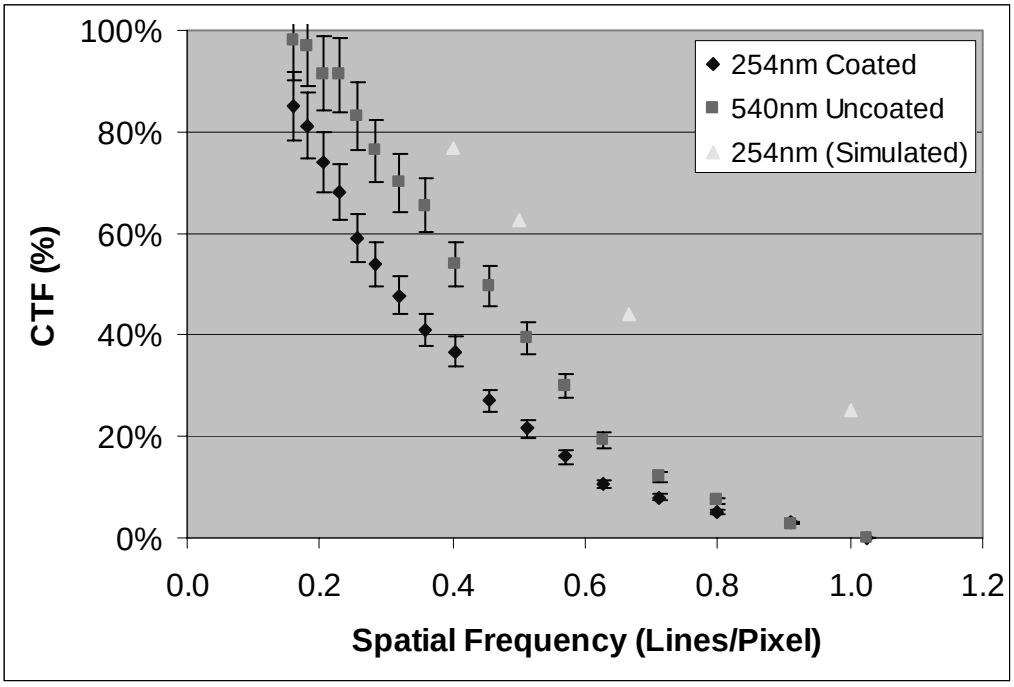

Figure 50 - Coated, Uncoated and Simulated CTF for Doctor Blade coated 2212 Phosphor coating on DALSA IA-D1-0256 Sensor, Thin Coating

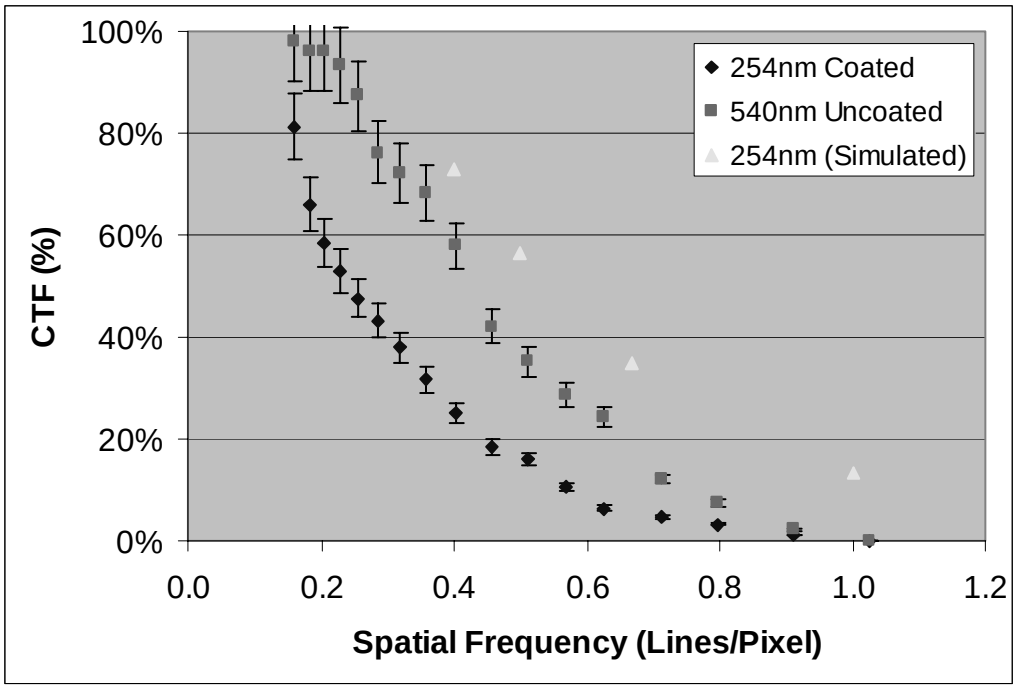

Figure 51 - Coated, Uncoated and Simulated CTF for Doctor Blade coated 2212 Phosphor coating on DALSA IA-D1-0256 Sensor, Medium Coating

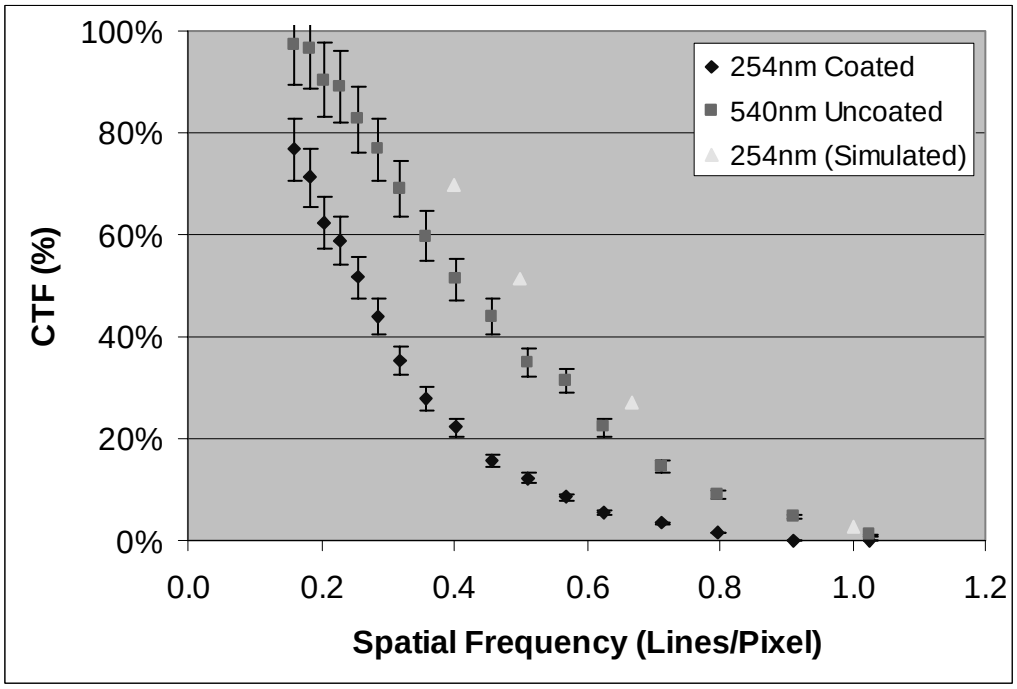

Figure 52 - Coated, Uncoated and Simulated CTF for Doctor Blade coated 2212 Phosphor coating on DALSA IA-D1-0256 Sensor, Thick Coating

All three sensors displayed a similar CTF curve, with the CTF decreasing with increasing spatial frequency. The results at 254nm and ½ Nyquist for all 3 sensors coated with 2212 phosphor are shown below in Table 11.

Table 11 - Summary of CTF Results at ½ Nyquist frequency for DALSA IA-D1-0256 Sensors coated with 2212 phosphor using Doctor Blade Method

Coating Thickness	Uncoated CTF @ 540nm (%)	Coated CTF @ 254nm (%) *(Simulated)*	% Decrease
Thin	39.5	21.6 *(62.7)*	45
Medium	35.1	16.1 *(56.6)*	54
Thick	34.9	12.3 *(51.4)*	65

The simulation predicted a very large drop in CTF, which was not realised by the measurements. However it did accurately predict that the CTF would be highest for the thin coating. Further discussion of the results and simulation will follow in Section 6.4.5.

6.3.6 CTF Results - 2345 Phosphor

The sensors coated with 2212 phosphor using the Doctor-Blade method were tested for CTF in the manner described in Section 3.3. The results are presented below in Figure 53, Figure 54 and Figure 55.

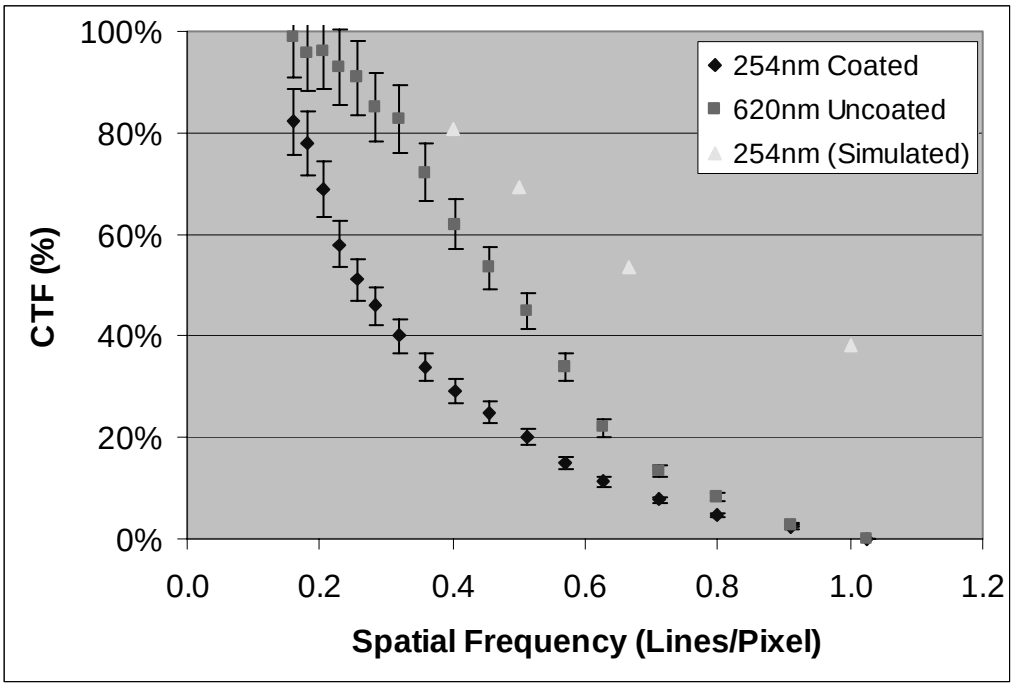

Figure 53 - Coated, Uncoated and Simulated CTF for Doctor Blade coated 2345 Phosphor coating on DALSA IA-D1-0256 Sensor, Thin Coating

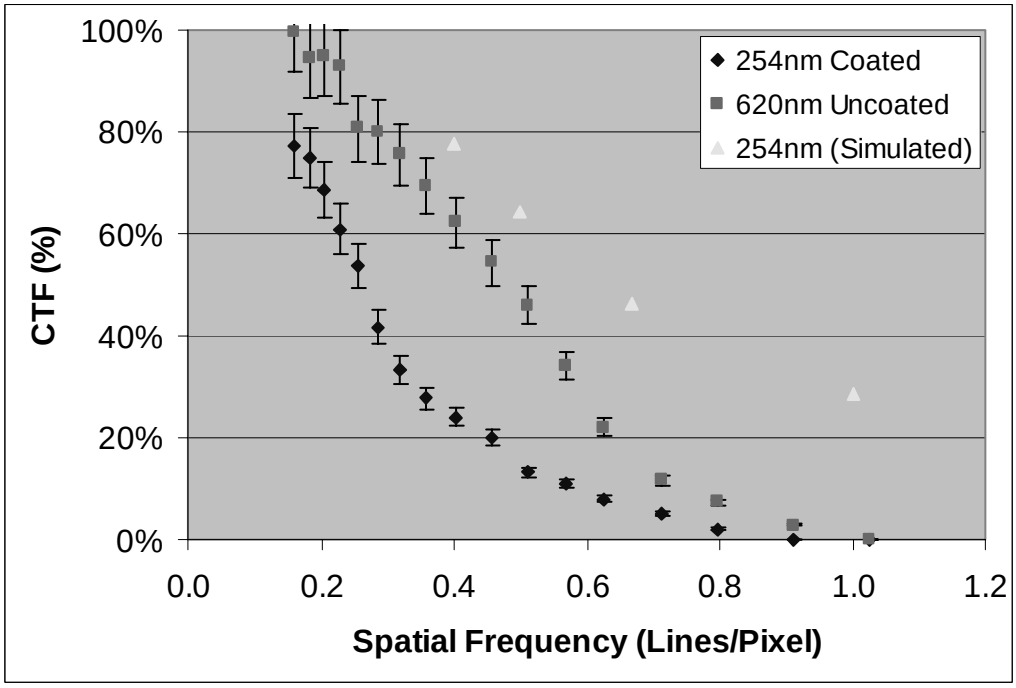

Figure 54 - Coated, Uncoated and Simulated CTF for Doctor Blade coated 2345 Phosphor coating on DALSA IA-D1-0256 Sensor, Medium Coating

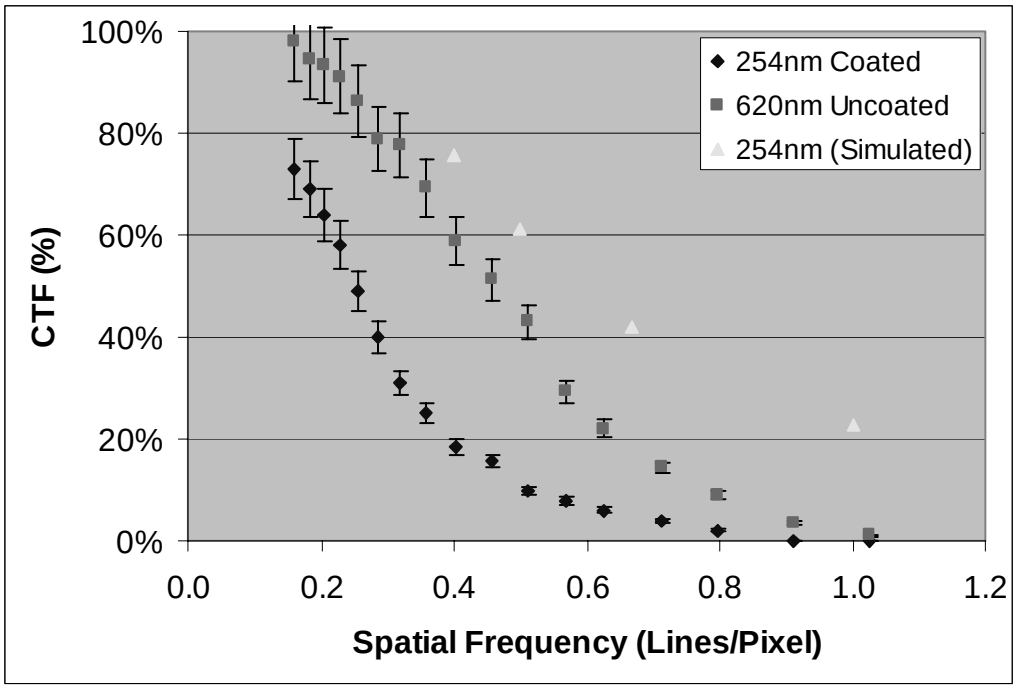

Figure 55 - Coated, Uncoated and Simulated CTF for Doctor Blade coated 2345 Phosphor coating on DALSA IA-D1-0256 Sensor, Thick Coating

As before, the CTF curves all showed the same general trend, decreasing with increasing spatial frequency. The results at 254nm and ½ Nyquist frequency for all 3 sensors coated with 2345 phosphor are shown below in Table 12.

Table 12 - Summary of CTF Results at ½ Nyquist frequency for DALSA IA-D1-0256 Sensors coated with 2345 phosphor using Doctor Blade Method

Coating Thickness	Uncoated CTF @ 620nm (%)	Coated CTF @ 254nm (%) *(Simulated)*	% Decrease
Thin	44.8	20.1 *(69.1)*	40
Medium	46.0	13.3 *(64.3)*	71
Thick	42.3	9.9 *(61.3)*	77

Expect in the case of the thinnest coating, these CTF values were all lower than the 2212-coated sensors presented in the previous section. The simulation predicts higher CTF values than were measured, although it is able to predict that the thinnest coating would display the best CTF. Further discussion of the results and simulation will follow in Section 6.4.6.

6.3.7 Summary of Results

A Summary of all the results for the Doctor Blade coating is shown in Table 13.

Table 13 - Summary of experimental results for Doctor-Blade coating on DALSA IA-D1-0256 Sensors

Coating Type	Doctor-Blade 2212			Doctor-Blade 2345			Settle Coat	
	Thin	Medium	Thick	Thin	Medium	Thick	Thin	Thick
Estimated Thickness	15μm	20μm	30μm	15μm	20μm	30μm	<20μm	>50μm
Peak QE Increase	158%	117%	67%	96%	86%	38%	36%	210%
PRNU Degradation @254nm	173%	119%	111%	540%	330%	300%	700%	160%
CTF Degradation @254nm, ½ Nyquist	45%	54%	65%	40%	71%	77%	n/a	n/a

The Doctor Blade coating was able to increase the QE by up to 158%, in the case of the thin 2212 coating. However this was lower than the thick settle coating, which showed a 210% improvement. The QE and CTF were highest with the thinnest Doctor blade coatings. The PRNU, however, was lowest with the thickest Doctor Blade coatings.

The Doctor Blade coatings can be made to almost any thickness, so the QE, PRNU and CTF can be tuned to meet the application. However there are

still issues that need to be resolved, such as the clustering, and the empty spaces with no phosphor coating. This would be a possible technique for fabricating inexpensive UV sensors if the slurry can be made more homogeneous, reducing the PRNU.

6.4 Simulation and Discussion

6.4.1 QE Results – 2212 Phosphor

The QE spectrum for each of the sensors (see Figure 42) has three distinct regions. First, the peak QE is at 254nm. Then the QE drops at 265nm and 300nm, then another lower region at 320nm, 340nm and 365nm. The coating absorbs a certain percentage of the incoming photons (this percentage is determined by the absorption coefficient and is different for each coating). At UV wavelengths, the phosphor absorbs photons and re-emits them at a longer wavelength. However the efficiency of the phosphor decreases as the wavelength increases. So the longer wavelength photons get absorbed, but no photons are re-emitted. At 320nm (for 2212 phosphor) this efficiency decreases to zero [40]. Therefore fewer photons are reaching the sensor's surface than without the coating, which explains why the longer wavelengths show a drop in QE, instead of an increase.

However the drops are much more severe than theory (simulation) predicts. As noted before, the only wavelength-dependent property in the simulation is the phosphor efficiency. In the case of 2212 phosphor, the efficiency is high for 254nm, 265nm, and 300nm. Since the experimental results show a substantial drop at 265nm and 300nm, it cannot be due to the drop in phosphor efficiency alone. In all 3 cases the simulation showed a slight

drop at 265nm but not as much as the experimental data. There are impurities in the doctor blading coating, so it can be assumed that they are absorbing more photons at 254nm and above. Since impurities have specific absorption spectra, these deviations from theory point to impurities in the coating.

The simulation also predicted a much lower QE at the longer wavelengths (greater than 320nm) than the experimental data showed. Looking at the empirical parameters helps to understand this.

absorption_coeff=0.15;

scattering_coeff=0.001;

absorption_coeff_2=0.02;

scattering_coeff_2=0.02;

Note the absorption coefficient of 0.15 is much higher than that of the AST coating (0.055) (see Section 5.4.1). This value of absorption coefficient was necessary to make the simulation have the same dependence on thickness as the experimental data. The effect of the four coefficients on the optimal thickness, the QE of shorter wavelengths and the QE of longer wavelengths is shown in Table 14.

Table 14 - Effect of the four simulation coefficients on the optimal thickness, the QE of shorter wavelengths and the QE of longer wavelengths

	Optimal thickness	QE of shorter wavelengths (where phosphor has high efficiency)	QE of longer wavelengths (where phosphor had low efficiency)
Absorption Coefficient 1	Inversely Proportional to	Proportional to	Inversely Proportional to
Scattering Coefficient 1	No effect	Inversely Proportional to	Inversely Proportional to
Absorption Coefficient 2	No effect	Inversely Proportional to	Inversely Proportional to
Scattering Coefficient 2	No effect	Inversely Proportional to	Inversely Proportional to

In this case, a high absorption coefficient was necessary to make 14μm the optimal thickness. A higher absorption coefficient also raises the shorter wavelength QE (where the phosphor has high efficiency) while lowering the longer wavelength QE (that is more dependent on UV light getting through the coating). The higher-than-expected experimental QE can be explained by the change in absorption and scattering due to wavelength (which the simulation did not consider, for reasons explained in Section 5.4). The longer wavelengths do not absorb or scatter as much as the shorter wavelengths. Because the absorption and scattering coefficients were much higher than the AST coating, this effect is more pronounced.

When the absorption coefficient of the UV light was set high, it made the longer wavelength QE extremely high, and had to be brought down to fit the experimental data by raising the absorption and scattering of re-emitted light in the coating. These values are much higher than for the AST coating. This further confirms the assumptions that the coating has more contamination than

the AST coating. As well, the AST coating had artificially low re-emitted scattering and absorption coefficients due to the single layer coating, the thicker coating here means the model for scattering and absorption through the coating fits better and gives a more accurate result.

6.4.2 QE Results – 2345 Phosphor

The QE spectrum for the 2345-coated sensors (Figure 43) is quite similar to the 2212-coated sensors. The peak QE is at 254nm, there is a large drop at 265nm, then another small drop at 300nm where the QE stays constant as the wavelength is increased. This fits in with theory that predicts the phosphor efficiency drops as the QE drops.

The QE for all thicknesses is much lower with the 2345 phosphor than with the 2212. Although the efficiency of the phosphor is higher, as explained in Section 2.2, it results in a lower overall sensor QE, for all wavelengths. This is due to several effects. First, the shape of the crystals, as shown in Figure 21, created more scattering of photons. This means fewer incident photons can be absorbed, and fewer re-emitted photons can be absorbed by the sensor. Second, the peak emission wavelength of the phosphor is 611nm, and the CCD is less responsive at that wavelength that at 550nm, the peak emission of the 2212 phosphor. Third, because of the reduced density of this phosphor, in order to get the desired thickness the density of the phosphor in the slurry had to be reduced, so there is twice as much residue from the gel as with the 2212 coating.

However, just like the 2212 coating, the drop at 265nm was more than theory predicted. For the same reasons, it can be assumed this is due to impurities in the coating. As well, this coating displayed the same higher-than-predicted QE for the longer wavelengths. This is due to the same effects as explained in the previous section.

The simulation parameters are shown here:

absorption_coeff=0.08;

scattering_coeff=0.01;

absorption_coeff_2=0.01;

scattering_coeff_2=0.03;

In order to make the simulation match the data, the absorption coefficient was much lower (almost half) and the scattering coefficient of UV light was higher by a factor of 10. Because of the more jagged shape of the crystals, it makes sense that there would be more scattering and less absorption. As well, the scattering coefficient was slightly higher and the absorption coefficient slightly lower for re-emitted light.

6.4.3 PRNU Results – 2212 Phosphor

The uncoated PRNU at 254nm is higher than the PRNU at 540nm and 620nm, as explained in Section 5.4.3, because of the gate reticulation designed into the sensor. However, the results for the coated PRNU at 254nm are far higher than for the AST coating. For an explanation, one has to look at the SEM photos of the Doctor-Bladed coatings. The coatings show large amounts of clustering, and in the case of the two thinner coatings, patches where there is no phosphor at all. The thickness varies substantially (see Section 6.2.4), and the thicker coatings (which should yield lower PRNUs) are not enough to make up for the roughness of the coating. As well, there was up to 10% residue in the coating, which in some cases formed into clusters, so this would affect the PRNU as well.

The thinnest coating had the highest PRNU, as expected. In a thicker coating, more photons will be absorbed and re-emitted (isotropically) further from the surface of the sensor. So the photons have more distance to “spread

out". As well, the photons will "spread" more because of scattering, due to the thicker layer. The same effects that reduce the CTF, by degrading the resolution, also help to lower the PRNU.

To generate the thickness matrix for the simulation, the SEM photos of the three coatings were examined (Section 6.2.4). For the thinnest coating, it was determined that the coating had a mean thickness of 15μm, and a standard deviation of 3μm. There were bare patches that accounted for approximately 50% of the surface area, and the thickness was not random, but tended to be in "clusters", areas about 30μm in diameter where there was a clump of phosphor. Within the cluster, the thickness would vary very little (an approximate standard deviation of 2μm). Since the pixel size of the sensor is 13μm, a cluster is approximately 2 pixels by 2 pixels. So a thickness matrix was made that contained 2x2 clusters, and in between them were all zeros. The position of the clusters were generated randomly, but they accounted for 50% of the entries (with zeroes accounting for the other 50%). One entry in the cluster was a random number, generated with a normal distribution with a mean of 15 and standard deviation of 3. The other three entries in the cluster were random Gaussian numbers with a mean equal to the first entry in the cluster, and a standard deviation of two. This is shown in Figure 56.

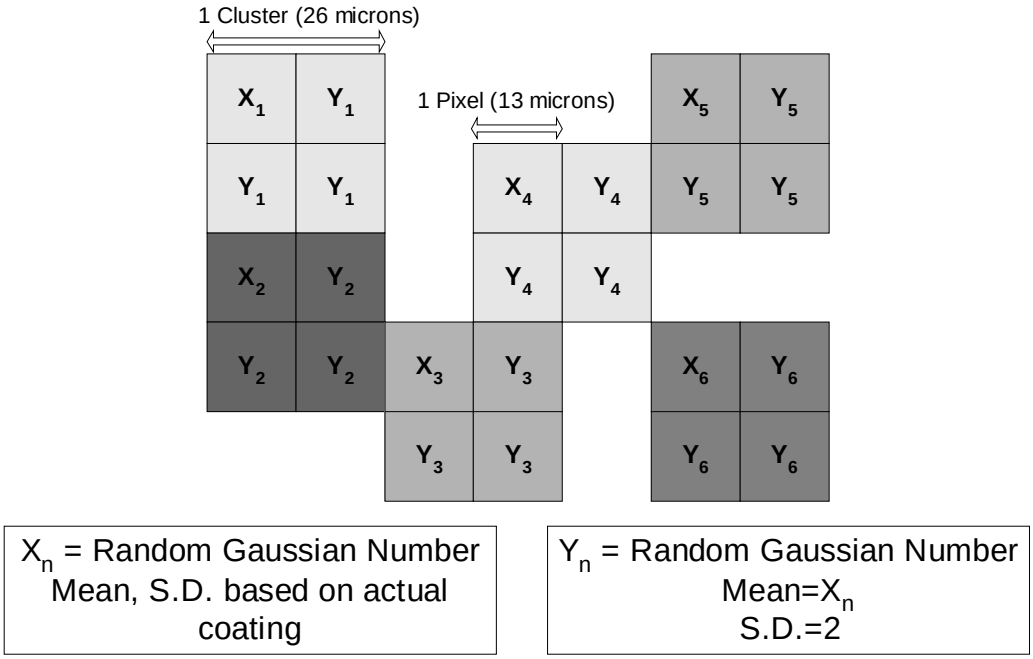

Figure 56 - Explanation of thickness matrix generation for PRNU Simulation

The medium coating was found to have a mean thickness of 18μm with a standard deviation of 6μm. The clusters had a mean diameter of approximately 30μm, with empty space accounting for approximately 25% of the coating. So a thickness matrix was made up, the same as the thin coating, but with the first entry in the cluster being a random number fitting the normal distribution with a mean of 18 and a standard deviation of 6, and the other 3 numbers, as before, with a mean equal to the first entry and a standard deviation of two. The clusters accounted for 75% of the entries, with 25% being zeros.

The thickest coating was found to have a mean thickness of 25μm, with a standard deviation of 10μm. The clusters were about 30μm in diameter, but there were no empty spaces. So the matrix was prepared in the same way as before, with one entry in the cluster a random number fitting a normal distribution with a mean of 25 and a standard deviation of 10, and the other 3

random numbers differing by a random number fitting the standard normal distribution. The clusters filled 100% of the matrix.

The simulation predicted that the PRNU would be very high, in fact much higher than was measured. The PRNU was quite accurate for the AST-coated sensors, however it was off by 200-400% for the doctor-blade coated sensors. The explanation can be found in one of the assumptions the simulation makes. When the incident UV light hits the coating, the simulator calculates how much is absorbed, and how much visible light is re-emitted. The re-emitted light that travels to a given pixel must travel through the coating, so some of it gets attenuated. However the simulator assumes that the photon is emitted inside the coating, and so after re-emission must travel the entire way through the coating. This assumption is valid for coatings that have uniform thickness. However, with large clusters and large empty spaces, some re-emitted photons will be able to travel to a pixel with no attenuation at all. This is shown in Figure 57.

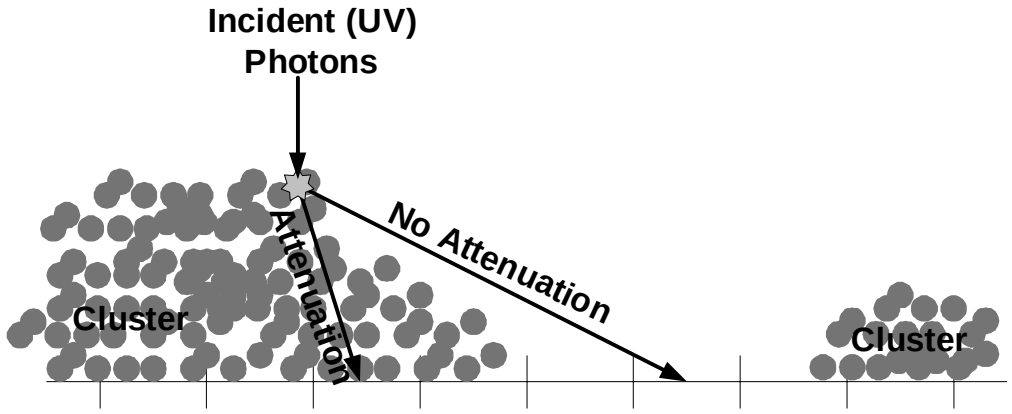

Figure 57 – Diagram of phosphor coating on image sensor, showing how clustering and bare spots affect attenuation of re-emitted photons

These uncoated pixels will actually experience a very large quantum efficiency, whereas the simulator predicts they would not. This partially compensates for the fact that those pixels have no phosphor on them and would

otherwise experience a low QE. As an example, a sample iteration of the simulation was performed for the situation of incoming photons being absorbed and re-emitted by phosphor on the edge of a cluster. The situation is shown in Figure 58.

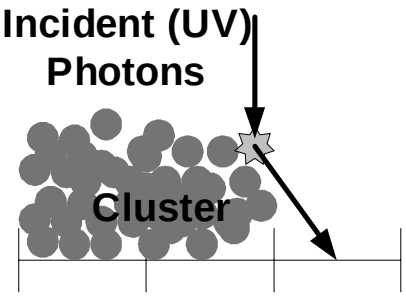

Figure 58 – Example situation for sample calculation to explain PRNU results

The parameters for this sample calculation are a 20μm coating, divided into 100 slices, using type 2212 phosphor at 254nm (therefore 0.95% efficiency), an incident light level of 100, and the scattering and absorption coefficients in Section 6.4.1. The photons absorbed (and re-emitted) in the top slice will be used, since the effect will be greatest. Using Equation 8 to obtain the photons absorbed in this slice, multiplying by the phosphor efficiency, and applying the solid angle correction (Equations 10-13) for the adjacent pixel gives a value of 0.30, to represent the intensity of photons travelling towards the given pixel. Note the intensity has no units, as explained in Chapter 4. In reality, all of these photons will reach the pixel, since there is no coating between the re-emitting phosphor and the pixel, as shown in Figure 58. However, the simulation assumes the coating is uniform, and therefore applies Equations 8 and 9 to represent the (re-emitted) photons absorbed and scattered on their way to the pixel. This leaves an intensity of only 0.071 reaching the pixel. The simulation was incorrect, in this case, by a factor of approximately four. This effect causes more photons to reach uncoated pixels, raising the QE

of those pixels, thereby lowering the overall PRNU. As was just shown, the simulator does not account for this effect.

As well, the simulator assumes the re-emitted photons can only travel into adjacent pixels. This assumption is valid in most cases, since the path into further pixels involves travelling through even more coating, so the attenuation is extremely large. However in this case there are areas with no attenuation, where the simulator's assumption is not valid. The simulator would need to be re-written to use increased resolution, and detect when the re-emitted photon left the coating. This would greatly increase the complexity and processing time of the simulation, and as mentioned in Chapter 4, the purpose is to show trends, which is does accurately in this situation.

So while an uneven coating gives a very large PRNU, especially coatings with clusters and empty spaces, the PRNU is not quite as high as would be predicted, since the empty areas actually allow for re-emitted photons to be absorbed more easily. This is a significant effect, as demonstrated by the sample calculation, and the large difference (see Table 9 and Table 10) between simulated and measured results.

6.4.4 PRNU Results – 2345 Phosphor

The results for the 2345 coated sensors are very similar to the other Doctor-Blade coated 2212 sensors. The PRNU at 254nm for all 3 sensors is much higher than the AST coating, due to the non-uniformities which can be seen in the SEM photos. The thinnest coating had the highest PRNU, and the thickest had the lowest. Both of these effects are explained in the previous section.

The PRNU for the 2345-coated sensors was much higher than that of the 2212-coated sensors. The different shape of the phosphor crystals, contributed to the increased non-uniformity in the coating. The phosphor's shape could

have caused it to clump more during the mixing of the slurry, causing increased non-uniformity in the density of phosphor in the coating. This can be seen in the SEM photos, and is reflected in the thickness matrices used for the simulation that are presented next. Another contributing factor is the higher percentage of gel residue left in the coating (twice as much as the 2212 coating), which would have clumped, as shown in the SEM photos, and caused non-uniformities in the overall efficiency of the coating.

For the simulation, the SEM photos were examined and measured (Section 6.2.5), and used to create the thickness matrices. The mean and standard deviation of the thickness for the thinnest coating was found to be identical to the thin 2212 coating, so the same thickness matrix was used. The medium coating had a mean thickness of 20μm, and a standard deviation of 10μm, with 25% uncoated area. Clusters were about 30μm in diameter, so a thickness matrix was prepared in the same way as for the 2212-coated medium thickness simulation, as described in the previous section. Finally, the thickest coating had a mean thickness of 25μm, with a standard deviation of 10μm, and 30μm clusters. So a thickness matrix was prepared in the same was as for the thick 2212-coating explained in the previous section.

The simulations predicted a much higher PRNU than was measured, just like the 2212-coated sensors. This is due to the assumption the simulator makes, that re-emitted photons will have to travel through the coating, causing attenuation. As explained in the previous section, the assumption does not always hold for a very uneven coating, with large clusters and empty spaces.

However the simulation was able to predict that the PRNU of the 2345-coated sensors would be higher than the 2212-coated sensors. Although it did not take into account the additional residue present in the coating, the thickness matrices had greater variation, so this validates the conclusion that the increased

PRNU is caused, at least in part, by the phosphor clumping more, causing a more uneven coating.

6.4.5 CTF Results – 2212 Phosphor

All three coatings had the same shape of CTF curve, with the CTF decreasing as the spatial frequency increased. The thicker coatings had more CTF degradation because more light was absorbed further from the surface of the sensor, so was able to spread out more before reaching the sensor.

The CTF results were higher than AST because of the clusters of phosphor, and the empty spaces. As explained in the previous section, a large clump next to an empty space means there would be little attenuation. So photons would be able to travel greater distances and therefore degrade the CTF further. As well, the coatings were all thicker than the AST coatings, which would cause the CTF to degrade.

For the simulation, the four coefficients were set to the values determined during the QE simulation. The simulation results were much higher than the measured results. The reasons for this are explained in Section 5.4.5. The simulation was able to accurately predict that the thicker coatings would have worse CTF.

6.4.6 CTF Results – 2345 Phosphor

The CTF degraded with increasing spatial frequency for all three coatings, as expected. The thicker coatings had worse CTF degradation because more light was absorbed further from the surface of the sensor, so was able to spread out more before it hit the sensor.

The CTF results were higher than the CTF results for the AST-coated sensors, because of the increased thickness of the coatings, and the clumps and empty spaces, as explained in the previous section.

The CTF results were worse than the Doctor-Blade 2212-coated sensors. Since the thickness was the same, it can be assumed that the decrease in CTF is due to spreading due to scattering. The 2345 phosphor causes more scattering, which causes both the incident and re-emitted photons to spread out as they travel through the coating, therefore lowering the CTF.

For the simulation, the four coefficients were set to the values determined during the QE simulation. The simulation results were much higher than the measured results. The reasons for this are explained in Section 5.4.5. The simulation was able to predict that the CTF would be best for the thinner coatings. However, the simulation also predicted that the CTF for this coating would be better than the 2212 coating, which was not the case. There are two reasons for this; the absorption coefficients, and the spreading due to scattering.

A higher absorption coefficient means that more of the UV photons are absorbed (and re-emitted isotropically) further from the surface of the sensor. This increased distance gives them more distance to spread out, degrading the CTF. A lower absorption coefficient means fewer photons are absorbed and more make it through the coating and end up in the pixel where they belong, so the CTF improves. The absorption coefficient (determined during the QE simulation) was 0.15 for the 2212 coating, and 0.08 for the 2345 coating.

The 2345 coating causes more scattering because of the phosphor's shape. The phosphor has a jagged shape, with sharper edges and more surface area. Both of these cause more scattering than the smooth, round shape of the 2212 phosphor. However the simulator does not take into account spreading due to scattering (only losses due to scattering). This would have degraded the measured value, but not the simulated value. So the scattering caused the

measured CTF to actually be lower, but the simulator did not take that into account.

7 Laser Ablation Coating

7.1 Theoretical Explanation

A high-power pulse laser can be used for the deposition of phosphors onto a substrate. The technique, known as Laser Ablation, can deposit the coating with or without vaporizing the material. In its simplest form, the laser is directed at the target material, which has been pressed into a pellet or disk. When the laser hits the target, it "ablates" the material (this mechanism is described later), breaking it up into vapor and particles, which are deposited on the substrate. All this should take place in a vacuum for optimal coating characteristics.

The difficult part of using this technique for depositing inorganic phosphors is getting the laser properties just right, so that the material will not vaporize. As explained previously, the phosphors must be in the correct ambient atmosphere when they crystallize, or they will not be active. This atmosphere is not known, since this is a commercial phosphor and Osram Sylvania would not want to reveal how they make it. So with laser ablation, if the crystalline structure is destroyed, it cannot re-form and still work as a phosphor. Even if the phosphor is not destroyed, high energy and heat levels can have undesired effects on the lifetime, the efficiency, and the absorption and emission spectrums.

This section deals with laser ablation theory, what other related work has been performed [3, 5, 15], and the parameters that can be used to predict the output variables. The laser ablation work performed in this research is outlined in Section 7.2, with the results presented in Section 7.3.

7.1.1 Benefits

Laser ablation is an extremely versatile technique that can be used in many applications. One of the reasons for this versatility is that any solid sample can be directly ablated into its vapor-phase components (i.e. vapor and particles). There are no sample size requirements, no sample preparation (other than pressing the pellet or disk), and no solution waste. As well, the film can be deposited with micron characteristics, not only involving the film thickness, but patterning as well. As widely used as this technique is, it is an extremely complex process which is fundamentally poorly understood.

7.1.2 Sample Forming

The phosphor powder needs to be ground and cold-pressed into pellets or disks to use as a target. The usual pressure used is around 2000Pa. Too high a pressure can degrade the efficiency by destroying the crystals. Too little pressure will cause too "loose" a pellet, and the material can come off too quickly and in an uncontrolled manner.

7.1.3 Setup

For optimal coating, the laser ablation should take place in a vacuum chamber. The laser can be positioned inside the chamber, but it can also easily be outside, as long as there is a window into the chamber. The laser is directed at the target (the pellet of pressed phosphor), and the substrate is placed in the path of the ablated particles. The amount of time the laser is on determines the thickness of the film. A schematic representation of a laser ablation setup is shown in Figure 59.

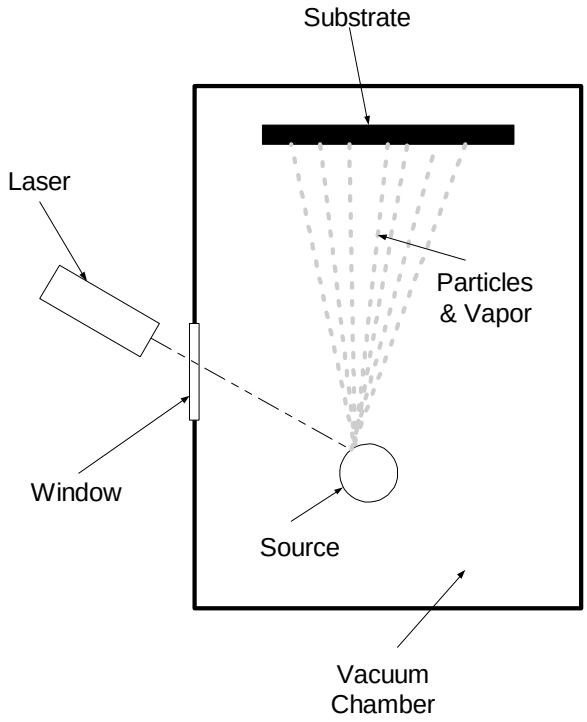

Figure 59 – Schematic of Laser Ablation setup

7.1.4 Fundamentals

If the laser has a long pulse and is very high power, the material will be evaporated. Called thermal sputtering, the material reaches liquid state and evaporates in a vacuum.

Although this is useful in some cases (described later on), most of this section will focus on depositing the material without vaporising the phosphor. Explaining the mechanism behind ablation would take a deep exploration into fundamental physics. In general, the laser has an extremely short pulse, in the nanosecond, picosecond or even femtosecond range. The pulse excites the electron of the molecule, which sends it flying off from the rest of the particles. This happens before a phonon (a unit of vibrational energy) can be transferred to the nucleus of the atom, which would cause it to heat up.

The main goal is to ablate individual particles while minimising the number that are vaporised. There will be a composition of atomic and molecular vapour, and particles. The percentage of each depends on the laser properties, which will be examine shortly. As long as most of the particles do not get vaporised, a functional film will be deposited. However some of the vaporised particles which do get deposited and collect on the substrate may even help by serving as a binder, even though they will be inactive.

There are four stages to the laser ablation process. First, the laser pulse itself. Second, the laser-sample interaction, where the actual ablation mechanism (or possibly vaporisation) takes place. Third, the particle transport. It could have kinetic energy due to ablation, or due to various vaporisation mechanisms which will be described at the end of this section. The final stage is the particle deposition, where the particles and vapour are deposited onto the substrate, and the vapour condenses into a solid. The amount of material that sticks to the substrate (compared to how much hits it) is the sticking coefficient, which can vary from 0 to 1. This is almost always assumed to be one.

To compare the various laser types and their effectiveness, it is useful to have a variable other than the film thickness. The ablation rate is the amount of material emitted per laser pulse. This can be evaluated in two different ways. First, it can be obtained from the depth of the crater created by the incoming radiation (this can be measured by optical microscopy). It can also be estimated using the amount of material deposited, accounting for the solid angle and the sticking coefficient.

7.1.5 Laser Properties

The amount of mass ablated from the solid target and its composition (vapour vs. particles) is highly dependent on the laser properties. Some of the properties

of a pulse laser include laser fluence (power density), wavelength, pulse duration, frequency (number of pulses per second), beam size, spatial profile (different parts of the beam being more powerful), and temporal profile (the beam being more powerful at different times during the pulse).

Laser fluence (in Joules per square centimetre) or the power density (in Watts per square centimetre) determines how much power is delivered when the laser is on. Higher laser fluence will cause more of the target particles to be removed, however it does not have much to do with gas/particle composition, as one might expect. A high fluence is necessary for ablation to even take place, and for vaporisation the fluence determines the transport mechanism. However we will see the pulse duration has much more to do with the composition of the ablated mass. A laser used for ablation is usually in the area of GW/cm^2.

The pulse duration is how long the laser is on for each pulse. The typical range is in the femtosecond to nanosecond range. This is six orders of magnitude, so we can expect quite different mechanisms to take place. In almost every way, a shorter pulse laser is much better for ablation. With shorter pulses, heat loss by diffusion into the solid is less, and more laser energy is converted into ablated mass instead of being dissipated in the sample. This transfers the most energy to the particle with the least amount of heat. Longer pulse lasers will vaporise many more of the particles.

The wavelength is also very important for the composition of the ablated material. A longer wavelength, such as in IR lasers, will cause more vaporisation. A shorter wavelength, such as in UV lasers, gives more mass ablated. It's also more efficient, which means more mass ablated for less energy. One reason may be the optical properties or the material at different wavelengths. Reflectance R can be an order of magnitude difference from IR to UV. The laser is also transferring much more energy in a shorter time, and as we've seen from the pulse duration that makes for better ablation.

The frequency is how many pulses the laser emits per second. Generally this is fixed by the type of laser, in the range of 5 Hz. It generally takes this long for the laser to recharge, and as long as the frequency is so high that it does not cause excessive heating, it is not a factor to worry about.

Beam size is generally fixed for most lasers, and as long as they are focused as much as possible this parameter is not vital to laser ablation. The beam size is very important for laser direct write, though (explained at the end).

The spatial profiles of a laser are something to be considered. The beam will generally be more powerful in certain spots, and this can cause uneven ablation in the pellet. If the substrate is very large, this can cause a problem, since it may be coated unevenly. This is one of the hardest challenges of laser ablation, and can be solved in various ways, addressed in the calibration and optimisation section. The temporal profiles are not much of a problem in extremely short pulse lasers that we are dealing with.

7.1.6 Calibration and Optimisation

As the laser ablates the material, the mass and shape changes, so the “spray” of ablated particles may change shape and direction. This is made worse if the laser has an uneven spatial profile, as most do. For small areas, this is not a problem, but for large areas such as display screens, the coating may be uneven. Advanced technologies are necessary to compensate for each of these effects. Technologies such as light scattering, acoustic emission in the sample, a mass monitor to collect a portion of the vapour, and spectrum emission intensities are just a few. However each of these are extremely complex, and are a research paper in and of themselves.

7.1.7 Preferential Ablation

One of the requirements for any deposition process is that the composition of deposited mass should be the same as the sample composition. However, some molecules are ablated better than others. This could be due to differences in the latent heat of vaporisation; some are vaporised more easily and therefore destroyed. It could also be due to different electrons in the valence shell, so they behave differently when they are excited. Equation 1 shows the ratio of ablated particles, in this case copper and zinc, although these could be replaced by anything. Here k_b is the Boltzmann constant, L is the latent heat of vaporisation, T_b is the boiling temperature and M is the mass of the atom. C is the bulk concentration, and the subscripts Cu and Zn indicate the components.

$$R_{\mathrm{Zn/Cu}} = \frac{C_{\mathrm{Zn}}}{C_{\mathrm{Cu}}}\sqrt{\frac{M_{\mathrm{Zn}}}{M_{\mathrm{Cu}}}}\exp\left(-\frac{(L_{\mathrm{vZn}} - L_{\mathrm{vCu}})}{k_{\mathrm{B}}T_{\mathrm{s}}} + \left(\frac{L_{\mathrm{vZn}}}{k_{\mathrm{B}}T_{\mathrm{BZn}}} - \frac{L_{\mathrm{vCu}}}{k_{\mathrm{B}}T_{\mathrm{BCu}}}\right)\right)$$

Equation 17 - Prefferential ablation ratio [3]

7.1.8 Thermal Evaporation

Although for inorganic phosphors we do not want any vaporisation, laser ablation can be used for organic compounds, metals, and other molecules that can be evaporated. All of the other considerations are the same, however the transport mechanisms are slightly different and are worth investigating [15].

There are three different regimes of ablation depending on laser fluence. These regimes are characterised by a large difference in ablation rate.

In the low fluence regime, thermal evaporation can account for the observed ablation rate. Treating the laser ablation as a point heat source in the ablated mass and applying the appropriate analysis, the amount of material ablated corresponds very closely with what the theory predicts. However, for the other two regimes, the ablation rates are much higher than simple thermal evaporation predicts.

In the mid fluence regime, the mechanism is based on the liquid-gas transition at the critical point (between solid and liquid). The laser heats the surface until it is just at the melting point of the material. In the low fluence regime, the individual particles are vaporised – here, the extra energy vaporises particles, but also heats the entire material until it just begins to melt. Particles leaving the surface with their own velocity exert a pressure on the liquid, and vapour formed on the surface gives another contribution to this pressure. This pressure increases strongly with increasing evaporation rate, and pressures as high as 10^8 Pa have been measured [15].

In the high fluence regime, the liquid rises in temperature well above the melting point. Temperature and pressure reach the critical value of irradiated material. At this point, the liquid transforms with zero enthalpy of evaporation to a highly compressed vapour phase and expands in a direction normal to the target surface.

The separation of regimes depends on the melting point and critical value of the material, so they will be different for each compound. However, as an example, for a XeCl laser with a 15ns pulse ablating SiC, below 1 J/cm^2 is the low fluence regime, from 1 to 1.6 J/cm^2 is the mid fluence regime, and above 1.6J/cm^2 is the high fluence regime.

7.1.9 Laser Direct Write

Laser Direct Write is a special application of laser ablation that can produce patterned phosphor on a substrate [13]. This is useful for multicolour displays where phosphors of different colour are all required to be patterned on the same surface. This method requires that the coating be first deposited onto a quartz ribbon, using another coating technique (such as doctor blading or standard laser ablation). The sensor is placed just under the ribbon, and the backside of the ribbon is illuminated with a laser, transferring the coating to the substrate. By positioning the ribbon very close to the substrate, the "spreading" effects of laser ablation can be minimized. Ideally, there will be a spot on the substrate the exact same shape as the laser beam. A schematic representation of this process is shown in Figure 60

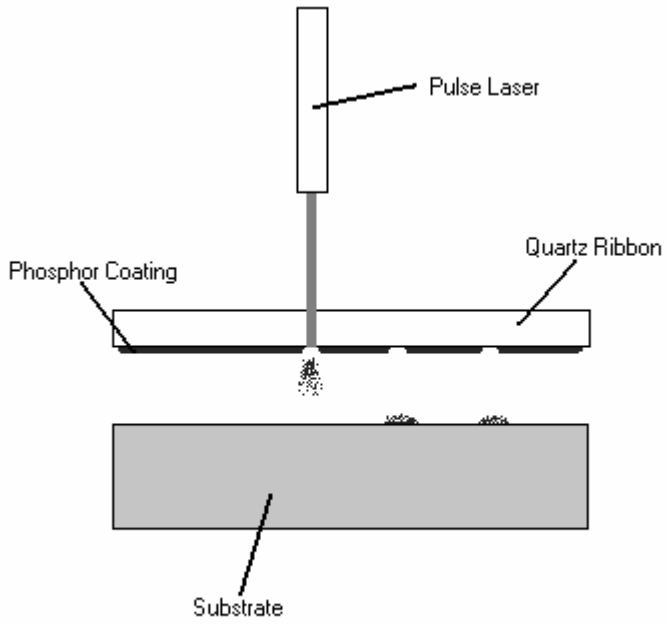

Figure 60 – Schematic representation of Laser Direct Write Process

One of the problems with this method is that the spot size is limited by the laser. Ideally one would like to be able to choose the size of the pixels (if it is for a display), instead of the laser doing the choosing. The size can be varied somewhat with some focusing of the beam.

Another problem with this technique is that the laser is actually pointing at the substrate. If the pulse is a little too long or the phosphor coating a little too thin, it is possible the laser could hit the substrate and damage it.

Laser direct write is a technique that shows some promise, however there are also some limitations and dangers that must be overcome.

Table 15 shows the relationships between the properties of the laser (the only properties in laser ablation that we are really concerned with), and the ablation properties.

Table 15 - Relationships between Laser Ablation Process Properties and Laser Properties

Laser Properties	Ablation Properties	
	% of particles in the ablated stream	Amount of mass ablated
Laser Fluence	**Decreases** with increasing fluence	**Increases** with increasing fluence
Pulse Duration	**Decreases** with increasing pulse duration	**Increases** with increasing pulse duration
Wavelength	**Decreases** with longer wavelength	**Decreases** with longer wavelength
Frequency	No effect	**Increases** with increasing frequency
Beam size	No effect	**Increases** with increasing Beam Size
Spatial profile	No effect	No effect
Temporal profile	No effect	No effect

7.2 Experimental Setup

The first step was to prepare a target of phosphor. This was done using a pellet press with a die made of tungsten carbide. The pellets discs were ½" in diameter and 5mm thick. The phosphor powder was put into the die, and the pressure was set to 5000lb and left for 60 minutes. Various pressures and times were tried and this was found to be optimal. Even so, the pellets were not firm. The 2212 phosphor pellets tended to crumble while handled, and the 2345 phosphor tended to "shear", coming off in slices. The pellets had to be made at the same location as the laser ablation was performed, and be transported and handled carefully.

The pellets and the sensor were put into a small stainless steel chamber with a window, which was then evacuated using a diffusion pump. The laser used was a KrF excimer laser, with a wavelength of 248nm. The power was 500mJ/pulse, with a pulse duration of 30 ns, with 10 pulses/second. The deposition was done in a vacuum, with an energy density of approximately 10 J/cm^2. The target-detector distance was approximately 3 cm. The small chamber was positioned so that the beam would hit the phosphor pellet, and the particles that flew off would hit the sensor's active area and coat the surface. Since the rate of ablation was unknown, the surface of the sensor was examined visually, and compared to various coated sensors with known thickness, so that an approximation could be made. A small piece of glass was placed next to the sensor so that SEM photos could be taken of the coating.

The 2212 phosphor ablated very easily, since the pellet was very loose. The pellet was used up quite quickly, and the maximum amount of phosphor was put down. The SEM photos of the glass coated at the same time as the sensors are shown in Figure 61.

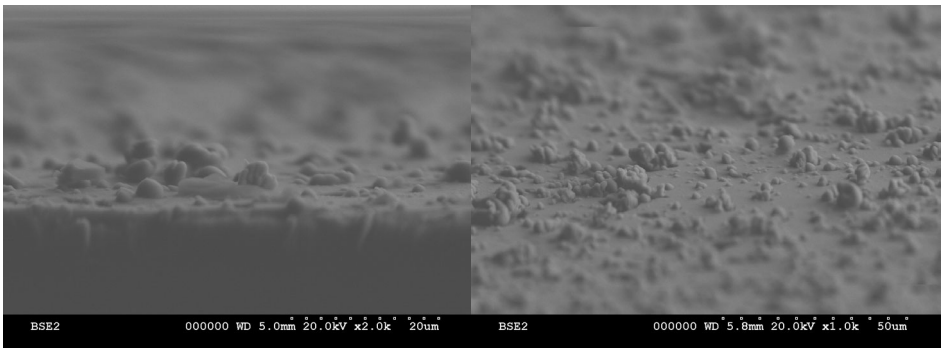

Figure 61 – SEM photographs of Laser Ablation coated 2212 phosphor coating on glass slide, showing sparse surface coverage

The photos show that the phosphor does not cover the entire surface of the sensor. Coverage is estimated at 20%. The particles are small and intact, from which we can gather that no melting of the phosphor occurred. The coating is quite even over large areas, as well. However more phosphor is needed to form a complete coating. This was not possible using the current setup, as the pellet could not be made thicker, and a different chamber would have to be used to hold a larger diameter pellet.

SEM photos of the 2345 coating are shown in Figure 62.

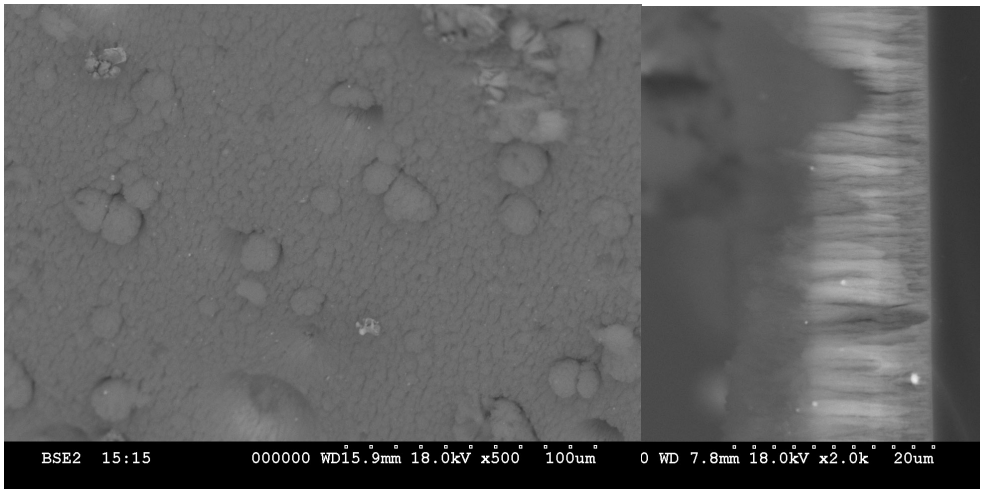

Figure 62 – SEM photographs of Laser Ablation coated 2345 phosphor coating on glass slide, showing columnar growth

In this case, it can be seen that the laser's power was enough to vaporize the phosphor, and re-deposit it onto the surface of the sensor. From the SEM photos it can be seen that this is columnar growth. Since the same laser settings were used it can be concluded that the melting temperature for this phosphor is lower than the 2212 phosphor. Some large clumps did break off, composed of multiple pieces of phosphor, but the coating is uniform , 13μm thick. In order for the phosphor to be active, it must be re-deposited in the correct ambient gases. Since this is a commercial phosphor from Osram Sylvania, with a proprietary formula, these could not be obtained, so the phosphor that has been re-grown on the surface is inactive. The clumps of phosphor on the surface, however, were active, and could be seen when the coating was exposed to UV light.

7.3 Experimental Results and Discussion

7.3.1 QE Results

The Laser Ablation Coated sensors were tested for QE in the manner described in Section 3.1. The results for the 2212-coated sensor are shown in Figure 63.

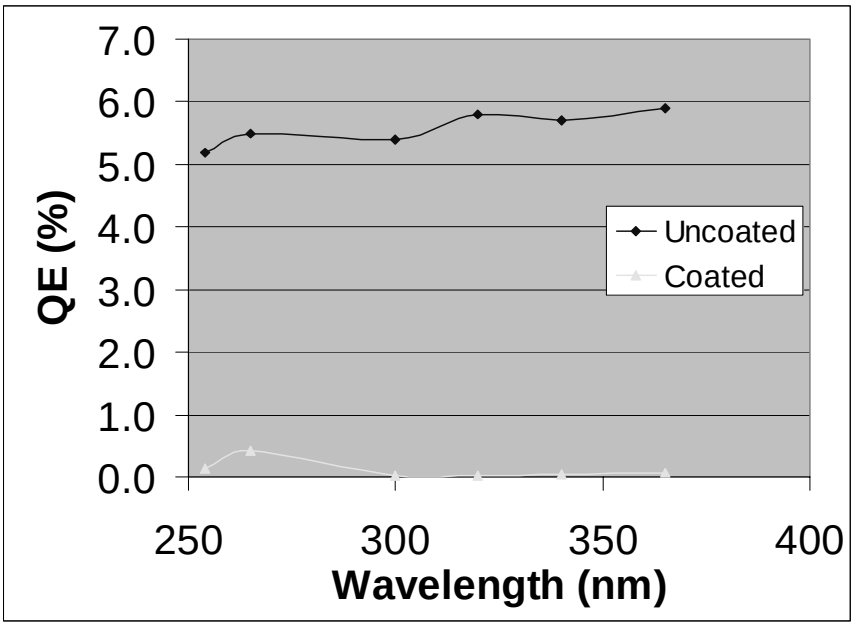

Figure 63 - QE Spectrum of Laser Ablation coated 2212 phosphor coating on DALSA IA-D1-0256 Sensor

The results show a vastly reduced QE. Although the sensor was still operational values of QE for all wavelengths were well below their uncoated values. The peak QE was 0.4% at 265nm, a 93% degradation relative to the uncoated sensor. Since the sensor was barely coated with phosphor, with mostly empty space, one would expect a QE very close the uncoated value. However, it seems the uncoated parts of the sensor were damaged and the QE was reduced. Since it is known that high levels of UV can damage the sensor, it is logical to assume that the scattered UV photons from the laser ablation hit the sensor's surface, and reduced the QE to almost zero. Therefore, even if a thicker coating could be obtained, the sensor would still be essentially non-operational.

The results for the 2345-coated sensor are shown below in Figure 64.

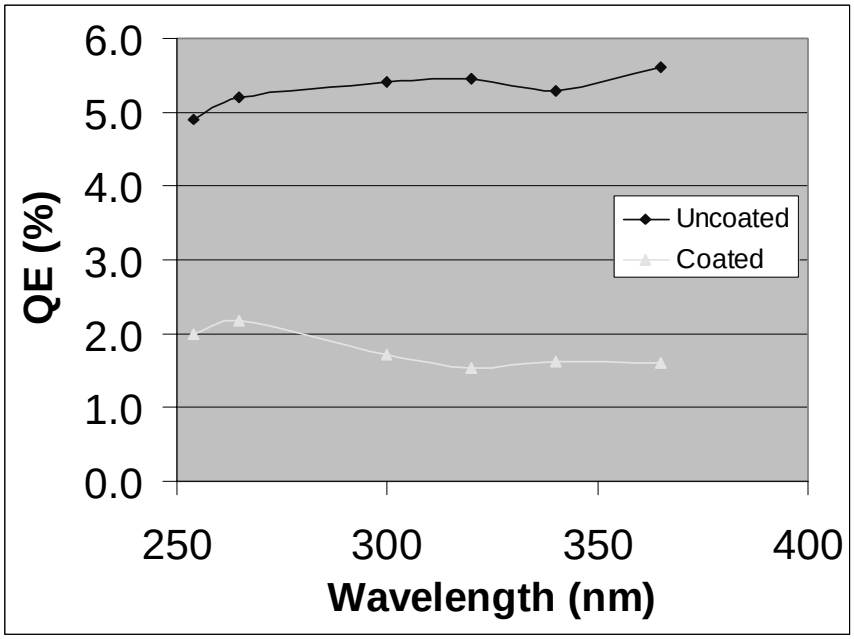

Figure 64 - QE Spectrum of Laser Ablation coated 2345 phosphor coating on DALSA IA-D1-0256 Sensor

In this case, although the QE is still vastly reduced from the uncoated value, it is higher than the previous sensor. The results showed a peak QE of 2.2% at 265nm, a relative drop of 58% from the uncoated sensor. Since the columnar growth of phosphor can be assumed to be inactive, it was the clumps of phosphor on the surface which were absorbing the UV photons and re-emitting visible photons. Because of the columnar growth on the surface, there were many paths to the surface of the sensor so some photons were able to get through. The UV damage was less on this sensor, and therefore the QE was higher, because of the layer of phosphor that grew on the surface of the sensor, partially protecting it from further UV damage.

7.3.2 PRNU Results

The Laser-Ablation coated sensors were tested for PRNU in the manner described in Section 3.2. The results for the 2212-coated sensor are shown below in Figure 65.

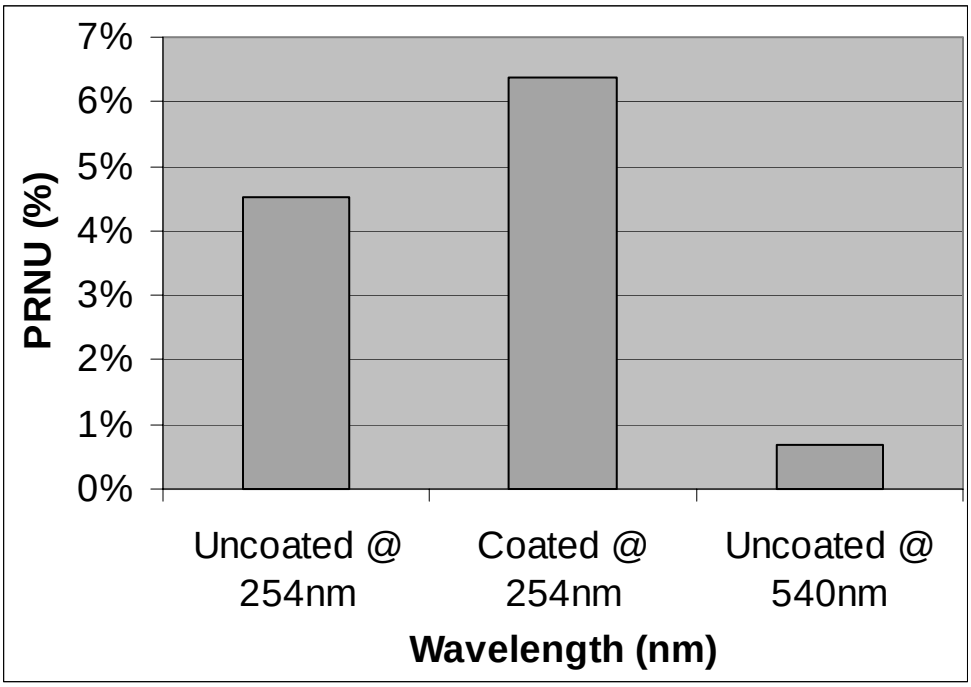

Figure 65 – Uncoated and Coated PRNU Results for Laser Ablation deposited 2212 phosphor coating on DALSA IA-D1-0256 Sensor

The PRNU for the coated sensor is 6.3%, a 40% relative increase from the uncoated sensor. This value fits well with the SEM photos which show mostly empty space with a low density of scattered crystal grains. The crystal grains would cause lower QE in the pixels they cover since they interfere with the incoming UV photons. The low coated PRNU also reveals that the UV damage was equal over the active area of the sensor.

The results for the 2345-coated sensor are shown in Figure 66.

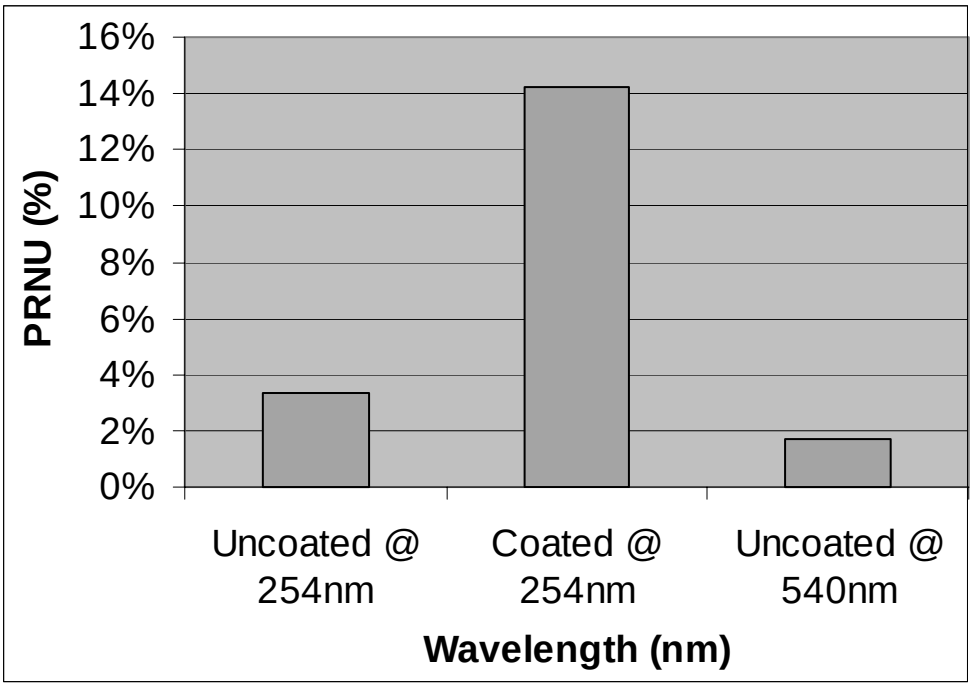

Figure 66 - Uncoated and Coated PRNU Results for Laser Ablation deposited 2345 phosphor coating on DALSA IA-D1-0256 Sensor

Here, the PRNU for the coated sensor is 14.1%, an increase of 400% relative to the uncoated value. This is much higher than the 2212-coated sensor, however the SEM photos reveal a 13μm coating on the surface, so a higher PRNU is expected. Although the coating is quite uniform, it is composed of "columns" of phosphor with spaces in between, where the incident photons can get through. The columns and spaces are large enough that they allow different amounts of light to each pixel, thereby increasing the PRNU. As well, the few individual crystal clusters on top of the coating are active. However they are far enough apart that they also serve to increase the PRNU.

7.3.3 CTF Results

The CTF tests are not presented here for the laser ablation coatings. The CTF of the 2212 coating would have been essentially unchanged, since there was not a continuous coating on the surface. Although the 2345-coated sensor had a

continuous coating, it was inactive, and therefore would not display CTF degradation due to isotropic emission of the phosphor. The two CTF results would not be comparable to anything else and would not reveal any additional information.

7.3.4 Summary of Results

A summary of the experimental results for the Laser Ablation Coating is presented in Table 16.

Table 16 - Summary of Experimental Results for Laser Ablation Deposited phosphor coatings on DALSA IA-D1-0256 Sensors

	2212-Coated	2345-Coated
Estimated Thickness	n/a	13µm
Peak QE Increase (@265nm)	-93%	-58%
PRNU Degradation @254nm	40%	400%
CTF Degradation @254nm, ½ Nyquist	n/a	n/a

In the case of the 2212 coating, the scattered UV photons from the laser lowered the QE to almost zero. The 2345 coating was deposited molecularly by vaporising the phosphor, so most of it was inactive. This coating did serve to partially protect the sensor from UV damage, however. The PRNU results reflect what was seen in the SEM photos, but since in both cases the coating was not deposited properly, these values do not reflect the values that would be obtained from a properly-deposited laser ablation coating.

It was shown that a laser could be used to deposit inorganic phosphor on the surface on a sensor, and that it would adhere properly. However, as seen with the 2345-coating, the parameters need to be adjusted for each phosphor to

prevent vaporization. As well, the issue of UV damage to the sensor must be dealt with, for this to be a viable technique.

8 Physical Vapour Deposition

8.1 Theoretical Explanation

Physical Vapour Deposition, or PVD, is a class of thin-film deposition processes where the source material is evaporated and transported to the substrate in a high-vacuum environment. This section will examine the various equipment and processes used to evaporate the source material. It will not go into detail on the mechanism of transport, or the process modifications that can be done during the transport (such as e-fields to separate ions from neutrals). It will also not focus on processes affecting the deposited film, such as resputtering or laser recrystallization. Most of the focus is on the various methods of evaporation, and how those affect the uniformity, rate control and monitoring, simplicity (cost/ease of use), and throughput.

This section deals with physical vapour deposition theory, what other related work has been performed [4, 9, 10, 14, 16, 17, 18, 20], and the parameters that can be used to predict the output variables. The doctor blading work performed in this research is outlined in Section 6.2, with the results presented in Section 6.3.

8.1.1 Process Steps

All thin-film processes involve the 4 (or 5) steps listed in Figure 67. The source is the actual material that will be deposited on the substrate (the object to be coated with the thin-film). This may be in the form of solid, liquid, vapour, or gas – the focus here will be will be on solid sources (this includes powders as well).

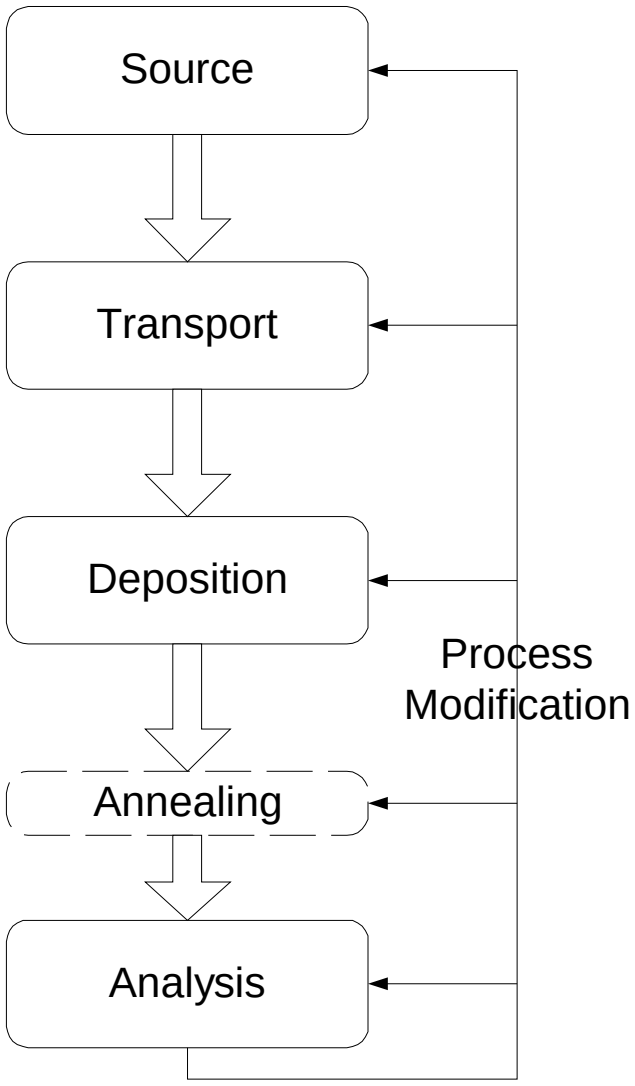

Figure 67 – Diagram of PVD Process Steps (Adapted from [16])

In order to have this material transported to and deposited on the substrate, this solid needs to be vaporised. This can be done in several different ways. First, the solid material can be put in a container with an open top, with the substrate above it. The container is heated, the source melts and evaporates, and is transported towards the substrate. This is known as thermal evaporation. Second, the material can be hit with a non-thermal source to vaporize it – an

electron beam (e-beam evaporation), or photons (laser ablation). Third, it can be hit with positive ions, a process known as sputtering. These three methods together are referred to as Physical Vapour Deposition (PVD). This section will focus on these three methods, and how they influence the deposition. The solid sources can also be chemically converted to vapours (eg. Ga to GaCl), or the source material can be a gas or a liquid to start with. If these have sufficient vapour pressure, they can be transported to the substrate. This is known as Chemical Vapour Deposition (CVD), and will not be covered here.

In the transport step, the vapour travels from the source material to the substrate. If this happens in the presence of a gas, the transport involves gas flow patterns and diffusion of the source material through the ambient gas. It also introduces contamination into the film, which may or may not be desirable. If the transport takes place in a vacuum, where the molecules fall is determined by geometry alone.

In the actual deposition of the film, the material, the transport, and the conditions at the deposition surface come into play. Three principal factors are involved here. The condition of the substrate surface, such as roughness, contamination, and composition determines how much of the incoming material will stick. The reactivity of the film determines how well incoming particles will be added to the film, once it has started to form. The energy input to the surface is a third factor, which is determined by the method of deposition. Except for how the different methods of transport affect the deposition, the actual deposition will not be covered in detail.

Finally, when refining the process one must analyse the film for the desired properties such as hardness, breakdown voltage, index of refraction, etc. This can be done by measuring the actual properties, or it can be done with a direct analysis of the film. Using those analysis results, one can go back and vary the parameters of the deposition process, and try to improve on the results.

8.1.2 Thermal Evaporation

Thermal evaporation is the most basic PVD process. Here the source material is heated until it evaporates. In fact, the thermal energy input to the system is not just for evaporating the source material, but also for driving the transport, reaction and the film formation. The mechanisms will be investigates, as well as what happens to the vapour once it arrives at the substrate.

8.1.3 Heating Sources

All heating sources consist of a container, which holds the evaporant. The container is heated in some manner, transferring thermal energy to the evaporant through either conduction or radiation. The following discussion will involve the selection of materials for the container, and the three types of heating sources; the twisted-wire coil, the dimpled boat, and the heat-shielded crucible. The criteria to examine here include the arrival rate, the arrival rate uniformity, and the contamination.

8.1.4 Materials for Heating Sources

All materials emit gases or vapours, from their surface or bulk, a process known as outgassing. This is a source of contamination in thin-film deposition processes, so the materials must be chosen carefully. The rate that the gasses from the material enter the process environment is in general unaffected by the pressure of the environment, so this applies equally to high-vacuum or atmospheric pressure systems.

Metals have two different mechanisms for outgassing; gases dissolved in the metal (from when the metal was in the atmosphere) and high-vapour-pressure alloying elements, parts of the actual metal itself.

Some particularly bad elements for outgassing alloying elements include Zn, Cd, Pb, Sb, P, S and Se, and Te. The most commonly used vacuum metals are stainless steel types 304(L) and 316(L), which are Fe-Ni-Cr alloys. This is only useful for temperatures below 450° C, since the small amount of Mn is very volatile and will outgas rapidly. For high temperature applications, the refractory (high melting point) metals W, Ta and Mo are best. Ta has the advantage of not becoming brittle after incandescent heating. W has the highest melting point and lowest outgassing of alloying elements of any metal.

The gas evolution from stainless steel consists of H and O dissolved in the metal while in the regular atmosphere, which react with the C in the steel. These gases include mostly CO, with some H_2, CO_2, and CH_4. Baking the metal prior to the deposition process can reduce these.

Sometimes the evaporant will alloy with the materials used in the heating source. This can result in the heating source becoming brittle, or even melting. Contamination is also an issue. If no suitable metal can be found, a ceramic container (or a ceramic-coated container) can be used. In evaporants such as Si, even ceramic will dissolve at the melting temperature. These cases are unsuitable for thermal evaporation. In these cases, evaporation must be carried out by focusing an energy beam into the centre of the solid material, so that the evaporating material only comes into contact with its solid form. This will be dealt with in the next section.

8.1.5 Thermal Evaporation Systems

Thermal evaporation systems are the simplest of all PVD systems. They consist of a vacuum chamber with a thermal evaporation source that uses joule heating to evaporate the source, as shown in Figure 68. The vapour gets transported to the substrate, and the vapour solidifies on the substrate, forming the thin-film.

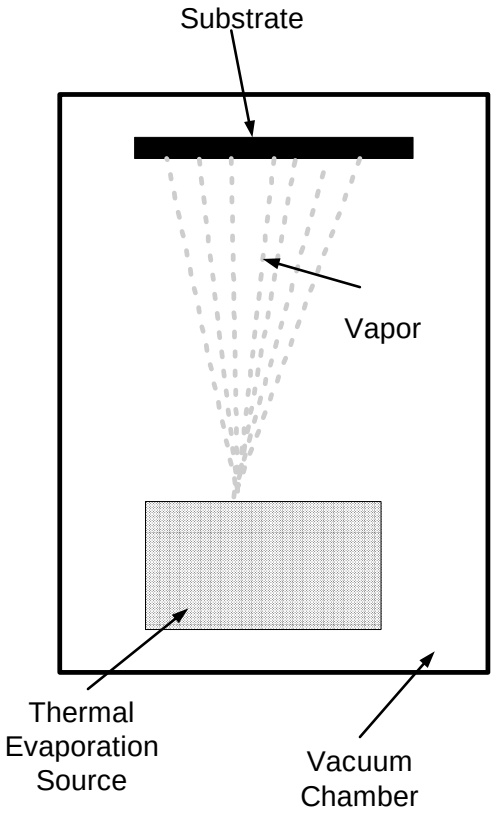

Figure 68 – Schematic Diagram of Basic Thermal Evaporation System

8.1.6 Twisted-Wire coil

There are three main types of heat sources for thermal evaporation processes. The first and the simplest is the twisted-wire coil, shown in Figure 69.

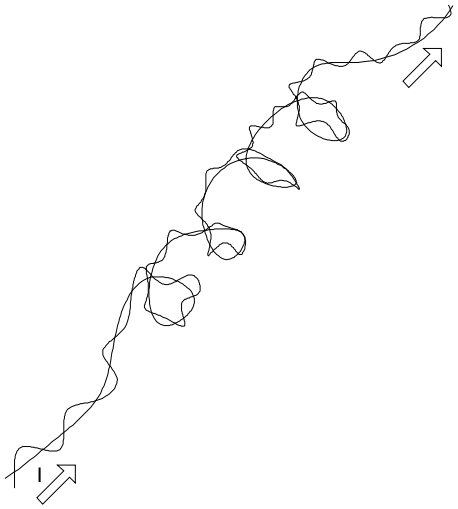

Figure 69 - Twisted-wire coil evaporation source (Adapted from [16])

A current of the order of 100A is passed through a twisted metal coil, while the coil is submerged in the source material. The selection of the metal for the coil is very important.

The twisted metal coil is usually made from one of the refractory metals, W, Ta or Mo. The amount of heat generated is simply I^2R. R is the parallel combination of the coil material/evaporant at the evaporation temperature, but the temperature is nonuniform because of heat conduction. Since evaporation rate depends on temperature, if one wants to control the rate of evaporation, it is insufficient to simply keep a constant current. One solution is to provide a feedback system that monitors the flux of the evaporant, and controls the current I. Such systems are awkward and expensive. Most often, the temperature of the source is monitored, and through experimentation the temperature can be calibrated to the flux.

Another important consideration is that this can only be used for metals that "wet" the wire; essentially forming a low-resistance contact so that heating through conduction can take place. So solids will have to be heated to their

melting point. Another option is to have the wire coated with the source material, which can then be used in the evaporation chamber. Otherwise heating is by radiation alone and for this design of heating element, the heating by radiation is insufficient for a practical process.

8.1.7 Dimpled Boat

The dimpled boat, shown in Figure 70, partially solves the problem of heating materials that do not "wet" the metal. The dimpled boat is essentially a plate of metal with a dimple in the centre that holds the source evaporant. A current is passed through the boat, of the order of 100A. The 4 pieces out of the side of the plate are to form high resistance regions, where more heating takes place. This is to prevent any evaporant from spreading away from the hot zone of the boat. These regions are much hotter than anywhere else on the boat, so in those regions the evaporation rate exceeds the spreading rate. So just like the twisted-wire coil, the dimpled boat is heated by joule heating, and the same problems in temperature monitoring for rate control apply as well. The difference here is that if the metal does not "wet" the boat, the heating by radiation is much higher, and sufficient to be used in an actual process. The thermal coupling is still lower than with conduction, so the boat will have to be much hotter than the evaporant, which makes temperature monitoring even more difficult.

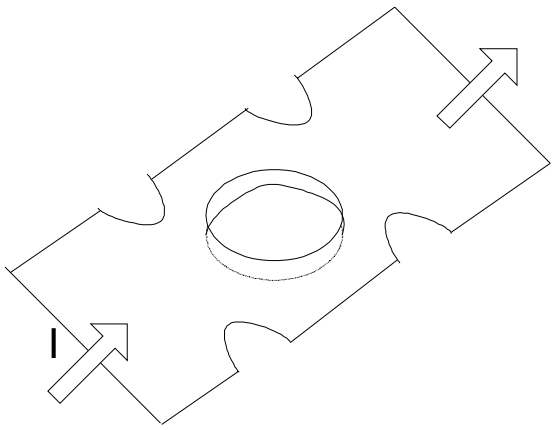

Figure 70 - Dimpled Boat Evaporation Source (Adapted from [16])

8.1.8 Heat-Shielded Crucible

Crucible sources, shown in Figure 71, solve the problem of flux monitoring by providing much better temperature uniformity and control. The heating coil is made of Ta, and is supported with notched ceramic rods to reduce heat sinking. The coil extends below the crucible bottom so a thermocouple can be attached to the bottom of the crucible and it will be in the same heating environment as the source. The heater coil is thinner near the crucible mouth, which offers higher resistance and therefore higher temperature. This prevents any evaporant from condensing at the mouth of the crucible. It also prevents spreading – just as the notches in the dimpled boat. Any material that tried to spread outside the mouth of the crucible would be evaporated because of the higher temperature. The heat shielding reflects radiation back to the crucible, increasing the temperature uniformity, and also keeping the high temperatures localized to the crucible.

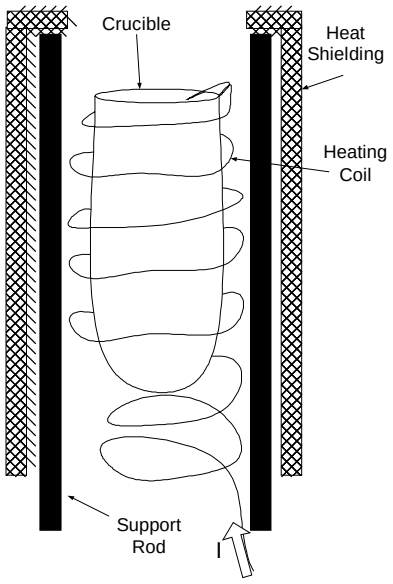

Figure 71 – Schematic Diagram of Heat-Shielded Crucible (Adapted from [16])

It is interesting to note that precise temperature uniformity is not necessary for high-quality evaporation – the only purpose is to make the feedback control more reliable, by making the temperature constant, the flux monitoring by temperature is more reliable.

The selection of materials for the crucible is the same as for the twisted-wire coil and dimpled boat.

8.1.9 Non-Thermal Evaporation

Up to this point, the focus has been on thermal means to evaporate the source material. Now non-thermal means of evaporating the source material will be examined. As mentioned before, the energy input is not only responsible for the evaporation, but also the transport, reaction and film formation. In fact, this energy may be directed directly at any of the 3 transport steps. This includes

vaporizing the source material, activating it during transport, and modifying the film structure once it has been deposited. This report, however, will focus only on using energy beams as sources for evaporation, and not for modifying the transport or deposited film. This energy can be in the form of electrons, photons, or ions. The point here is that the energy beam is so tightly focused, it creates heating in the source material, so the evaporation is by thermal means, but without explicit thermal input. Note this is different from sputtering, where the ions are distributed over a large area, so no heating takes place – it is by direct momentum transfer alone.

The use of energy beams offers several advantages over the Joule heating methods mentioned previously. First, any material can be vaporized – it was mentioned previously that some materials could not be heated by traditional methods, because they would react with anything that held them. Another advantage is that the evaporated material has more energy than the thermal energy at the source surface. This energy helps out the deposition process. In the case of an ionized vapour, charging the substrate can accelerate the vapour even faster towards the source.

8.1.10 Electron-Beam Evaporation

In electron-beam evaporation (or e-beam evaporation) an intense beam of high-energy electrons is used to evaporate the source material. A hot filament emits the electrons, and using electric fields they are accelerated into the source material. Since the beam is focused, there is enough energy density to evaporate any material. Typically, 1A of electrons are accelerated through 10 kV, delivering 10kW to a small area in the source material.

Figure 72 shows a typical e-beam evaporation set-up. If the e-beam were positioned to hit the source directly, the evaporated material could hit the

filament and contaminate it. So the filament is located out of sight of the source, and magnetic fields are used to bend the beam. The magnetic field can be generated with a permanent magnet, but it is advantageous to use a solenoid so the magnetic field can be controlled, and the beam "steered". If the beam is aimed only at the centre of the source material, the deposition will be non-uniform. This is because at the point of evaporation, there is a small depression in the surface of the source material due to the material being evaporated. This will cause the vapour to be slightly collimated. This can happen even with molten metals, since the evaporation happens faster than their ability to flow in and fill the void. With the addition of a second lateral steering coil, the beam can be scanned around the entire surface of the source material, obtaining a more even distribution.

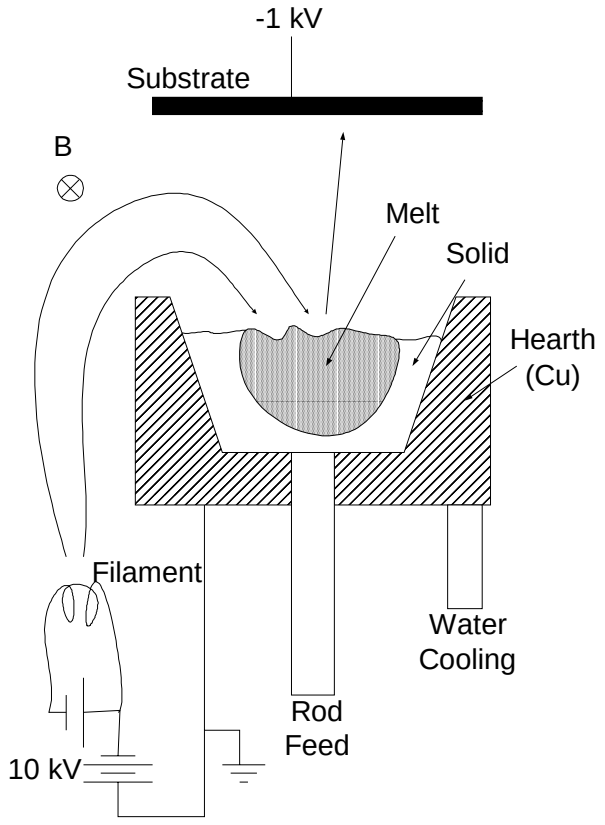

Figure 72 – Schematic of E-beam evaporation system (Adapted from [16])

Flux monitoring is more of a problem with e-beam evaporation, since the evaporation rate can fluctuate rapidly. Just as with the thermal evaporation, the best way to control is it to obtain the relationship between power to the filament and deposition rate. Once calibrated, one only has to control the power to the filament to obtain the desired evaporation rate.

The source material is usually contained in a copper "hearth" which is grounded to take care of any stray electrons from the beam. This hearth should be water cooled to prevent alloying with molten source materials. One of the real advantages of e-beam evaporation is that the material is essentially being evaporated from a container formed by its own solid phase. For certain materials, a solid bar can be continually pushed up into the chamber, so an enormous amount of material can be evaporated before reloading.

One major issue with energy beams is "macroparticle-splitting". This happens very little with thermal evaporation sources, but happens quite frequently with e-beam evaporation. All source materials will have certain contaminants in them – when that material is suddenly evaporated, if its vapour pressure is much higher than that of the source material it can knock off a solid or liquid macroparticle ("clump" of unevaporated material), from 0.1 to 1 μm in size. This macroparticle will more than likely end up on the evaporated film, since it travels at such high speeds that gravity doesn't play much of a role. Since many of these particles are charged, a transverse electric field can deflect some of them, reducing this effect. However, in certain situation this effect may be desirable. Some materials, such as inorganic phosphor crystals, cannot be melted or they will no longer work when re-crystallized. In this case, the dominant mechanism must be macroparticle splitting, and individual crystals or clumps of them can be deposited on the substrate, with the crystals that do melt being used as an (inactive) binder. A material with a very high vapour pressure

may be included with the crystals to aid in the macroparticle splitting mechanism. Flat-panel and plasma displays have been coated successfully using e-beam evaporation in this way.

8.1.11 Laser Ablation

A high-power pulse laser can also be used for the deposition of source material onto a substrate. The technique, known as Laser Ablation, can deposit the coating with or without vaporizing the material. Technically, laser ablation not involving vaporization is quite a different mechanism from evaporation, and is generally not considered PVD. This type of laser ablation is explained in Section 6.1.

8.1.12 Sputtering

Sputtering uses an ion source to vaporize the source material. Unlike other methods discussed previously such as thermal evaporation, e-beam evaporation and laser ablation, the ion beam does not thermally evaporate the source material. Instead, it works because the bombarding ions have energies that are much greater than chemical bond strengths. Although heat is generated, it is not the primary evaporation mechanism. The ions transfer energy to the source in the form of momentum. Sputtering has some distinct advantages. First, any material can be vaporized with sputtering. Second, the material is vaporized stoichiometrically. Third, because the ions are spread out over the entire surface of the source material, the coverage is much more uniform, especially for a large areas.

There are two common set-ups for sputtering deposition, both of which use a glow discharge plasma to generate inert gas ions. The ions are then

accelerated until they hit the target, knocking off source material atoms, which then travel towards the substrate. The first, known as ion beam sputtering, is shown in Figure 73.

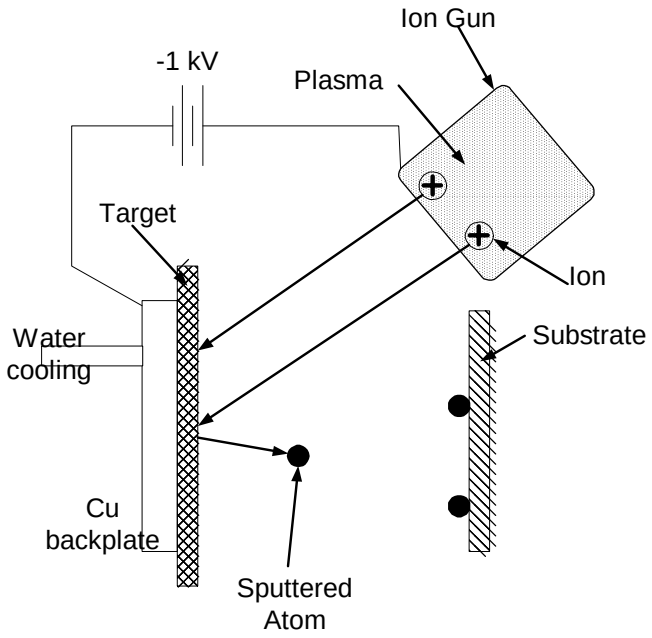

Figure 73 - Schematic for Ion Beam Sputtering (Adapted from [16])

Even though thermal energy is not the primary mechanism to get the source atoms to the substrate, quite a bit of heat is generated in the source. So the target must be attached to a copper backplate with water-cooling. Otherwise, the target material could melt, which is undesirable for sputtering. The ion gun is essentially just a plasma source, where the ions are extracted and accelerated towards the source due to the positive bias of the gun, with respect to the copper backplate. The real advantage of this technique comes with the separate control of flux and energy. The ion flux is determined by the intensity of the plasma in the gun, and the ion energy is controlled by the bias of the gun assembly. The ion gun can also be moved to hit the target at a different angle. These adjustments make this set-up highly versatile. However throughput is

low because the ion flux to the target is lower, and the substrate must be further from the target.

The glow discharge sputtering set-up is shown in Figure 74. Here, the plasma is not contained in a separate ion gun, but is in the chamber with the source and substrate. The ions are accelerated out of the plasma towards the source due to the voltage difference between the plasma and the target. Note the ions are always hitting perpendicularly.

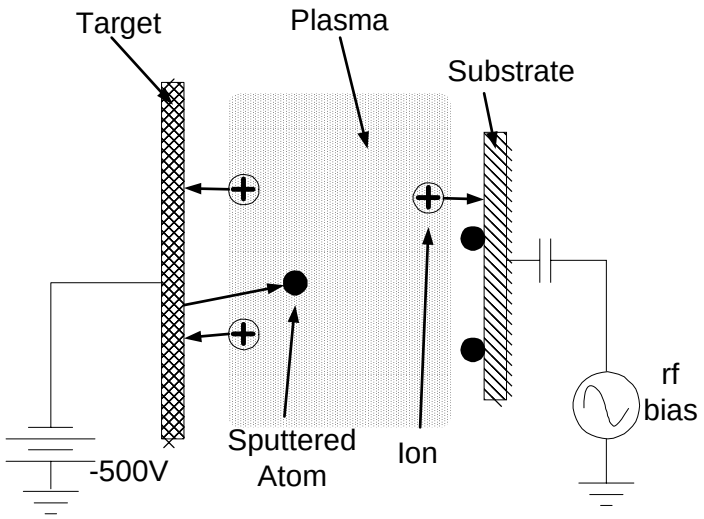

Figure 74 - Schematic for Glow Discharge Sputtering (Adapted from [16])

With glow discharge sputtering, the ion flux and ion energy are related by the electrical impedance of the plasma, since the target is in it. So these process parameters cannot be modified at will, and the angle the ions hit the source cannot be changed at all. This process makes up for it by having much higher deposition rate, so it is preferred for simple and routine depositions, or ones where the process parameters have already been worked out using the ion gun.

Because there are so many factors that determine sputter deposition rate, such as the ion flux, ion energy, target-substrate geometry, gas pressure, and various biasing, calculation will not be very accurate. Direct measurement is the best way, and then a constant sputtering rate should be obtained by keeping the process parameters constant. There is no change over time, as with some of the other PVD methods.

8.1.13 Conclusions

Physical Vapour Deposition, in all its forms, involves transferring energy to a solid or liquid source, which then vaporizes and is transported to the substrate. Thermal evaporation is the simplest of these methods. In thermal evaporation, Joule heat provides the energy source in the form of thermal energy. The twisted-wire coil is the simplest of these, however energy has to be transferred by conduction alone, which limits the applications. The dimpled boat transfers energy by both conduction and radiation, however rate control and monitoring is difficult. The heat-shielded crucible is the most advanced of these, providing predictable deposition and high throughput. All thermal evaporation techniques suffered from limited use, however – it cannot be used with any materials that might alloy or react with the container. Since the container is hotter than the actual source, contamination was a problem as well.

E-beam evaporation and laser ablation solve that problem by essentially evaporating that liquid in a crucible formed by the solid form of the source, so contamination is not an issue. With e-beam evaporation, a beam of high-energy electrons is directed at the source. Since the beam is very focused, the area gets extremely hot and evaporation happens by thermal means, but in a small area. Uniformity is more of a problem, so the beam must be scanned along the surface to get uniform deposition over a larger area. Laser ablation uses a high-

power short-pulse laser to transfer intense energy to the source material. The material is evaporated explosively, and travels to the substrate with very high energy. The laser must be scanned or the substrate rotated to get a uniform deposition. A laser with an extremely short, low energy pulse can transfer energy to the atom before it transfers heat, knocking off the molecules without heating up the source. This has been used successfully with high-temperature superconductors and other materials that should not be thermally vaporized.

Finally, sputtering uses ions from a plasma source to bombard the source, transferring momentum and vaporizing the source in that way. Since the ions hit a large area, uniformity is not as much of an issue. The ion gun sputtering allows for more process control, but the glow discharge sputtering allows for higher throughput.

8.2 Experimental Setup

The evaporator system consisted of a water-cooled hearth, which held the crucible containing the material. The phosphor was put, in powder form, in a graphite crucible, which was placed in the hearth. The entire system was enclosed in a bell jar, which was evacuated using a diffusion pump. A schematic diagram is shown in Figure 75.

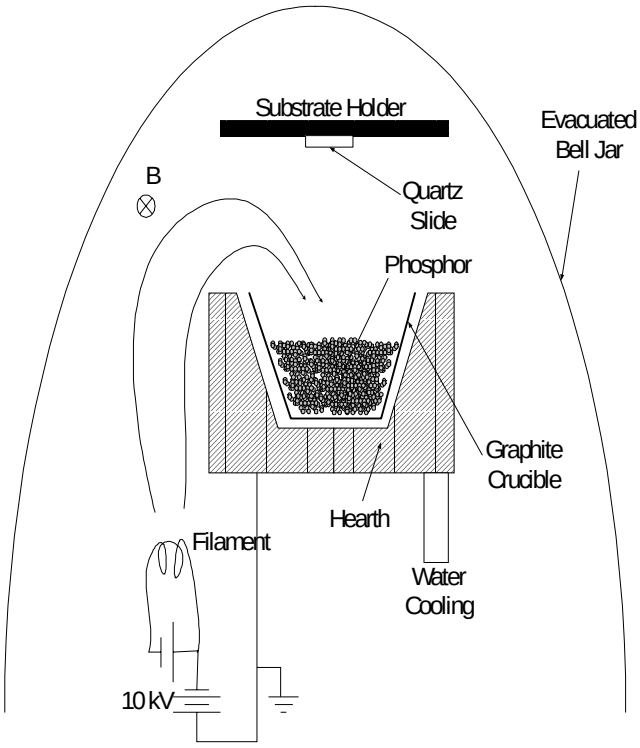

Figure 75 - Schematic Diagram of e-beam system used for evaporation of Osram Sylvania 2345 phosphor

The equipment used was a Varian E-Beam system. The electron beam was set to 6 kV, 150 mA and 900 watts.

When the system was started, the electron beam was aimed at the 2345 phosphor in the crucible. Immediately, some large clusters of phosphor (1-2mm in diameter) were ejected from the crucible, however they did not have enough energy to travel up to the susbstrate, and simply lay on the hearth. The phosphor, since it is an insulator, became negatively charged, and repelled the beam. It was not possible to focus the beam onto the phosphor after that. The phosphor was glowing red, showing that it was emitting photons, however the time constant for the phosphors is in the order of one millisecond [41], and this glowed for several seconds, even after the beam was turned off. This indicates

a charging effect, and it is likely this reduced the efficiency of the phosphor. There was no phosphor deposited onto the quartz slide.

8.3 Experimental Results and Discussion

Since no phosphor was able to be deposited, no results could be obtained. In order to make this technique work, the issue of the phosphor charging would have to be addressed. One possibility is to add a conductive material to the phosphor powder, so that the electrons from the beam would not build up in the material. However, this material would probably be deposited onto the substrate as well. Another option would be to get a more precise, highly focused electron beam, that could hit small areas (on the order of $1mm^2$) of phosphor powder individually. It could send a pulse over the surface area of the phosphor powder, never hitting the same area twice (since it would be charged) and applying small, controlled pulses which would deposit the phosphor on the substrate. However, such a system was not available for this research.

9 Summary

In this section results that have been presented in Chapters 5, 6, 7 and 8 will be discussed. Final remarks and conclusions will be made with respect to the four coating techniques used to obtain a UV-responsive CCD image sensor. Recommendations will be made for future research to improve the coating.

9.1 Summary of Experimental Results

Applied Scintillation Technologies coated two DALSA IA-D1-0256 sensors with inorganic phosphor; one with Osram Sylvania 2212 phosphor, and the other with Osram Sylvania 2345-phosphor. The proprietary deposition technique used could deposit the phosphor crystals in a coating 1 to 1 ½ crystals thick. The results are summarized in Table 17. While the AST coating using 2212 phosphor achieves a lower PRNU and CTF degradation compared to all other coating techniques, the QE is lower than the Settle-coat technique demonstrated previously by Franks et. al [1,2], but higher than all others. The AST coating using 2345 phosphor achieves a slightly lower CTF degradation but shows more degradation in the QE and PRNU compared to the 2212 coating. The thickness of the coating is a function only of the size of phosphor crystals, so for a given phosphor the thickness if not controllable.

A coating technique using a doctor blade was developed to coat DALSA IA-D1-0256 sensors with Osram Sylvania 2212 and 2345 phosphor. The technique involved the preparation of a slurry, consisting of an evaporating gel and phosphor crystals. The slurry was applied to the packaged sensor, then a high-precision blade was swept over the sensor, removing the excess slurry and

leaving a thin, uniform coating of slurry on top of the sensor. The slurry was left to evaporate, leaving behind the phosphor, and the solid residue from the gel (10-20% of the mass of the phosphor). The results are summarized in Table 17.

The coatings using 2345 phosphor were inferior in all tests, and therefore not presented here. The thinnest coating showed a higher QE than all other doctor-blade coatings, however this was lower than both the AST coating and the previous settle coating. However the thinnest coatings displayed the most degraded PRNU of all the doctor-blade coatings. The PRNU degradation of the thickest coatings were the lowest of all doctor-blade coatings, showing less degradation than the settle-coat but more than the AST-coating. The CTF results were inferior to the AST coatings as well. The thickness of the coating is fully controllable using this technique.

A UV excimer laser was used to deposit phosphor on DALSA IA-D1-0256 image sensors. This involved pressing the phosphor into a pellet. The pellet was put in a vacuum chamber, where the laser ablated particles onto the sensor. The results are presented in Table 17. In the case of 2212 phosphor, there was no coating on the sensor. There were individual particles that did stick to the surface, however these only covered approximately 20% of the surface. In the case of 2345 phosphor, the coating was composed of re-crystallized phosphor. Instead of depositing the particles intact on the sensor, the phosphor was vaporized and re-crystallized on the surface, rendering the phosphor inactive. This sensor showed poor PRNU and the QE was lower than the uncoated values. The CTF test assumes isotropic emission of photons in the phosphor – since the phosphor was inactive the CTF results are meaningless and are therefore not presented.

A coating was not achieved with the e-beam technique, therefore no results are presented here.

Table 17 - Summary of best results for all viable coating techniques performed with Osram Sylvania 2212 and 2345 phosphor, on DALSA IA-D1-0256 Sensors

	AST-Coated 2345	AST-Coated 2212	Doctor-Blade 2212			Laser Ablation 2345	Settle-Coat Thick
			Thin	Medium	Thick		
Estimated Thickness	7µm	10µm	15µm	20µm	30µm	13µm	>50µm
Peak QE Increase	74%	174%	158%	117%	67%	-58%	210%
PRNU Degradation @254nm	37%	-11% (decrease)	173%	119%	111%	400%	160%
CTF Degradation @254nm, ½ Nyquist	30.1%	37.1%	45%	54%	65%	n/a	n/a

Table 17 omits some of the results presented in Chapters 5, 6, 7 and 8. Specifically, the Doctor-Blade 2345 phosphor coating was omitted because all test results were inferior to the 2212 phosphor coating. The Laser Ablation 2212 coating was omitted because it could not form a complete coating. The e-beam method could not produce a coating, so no testing could be done.

9.2 Conclusions

The conclusions drawn from this research project are presented here in order of importance:

1. The AST coating presented here is a viable alternative to other UV-responsive image sensor design such as organic phosphor coatings and structural modifications.
2. The Doctor blade coating shows promise as a versatile, repeatable, and low-cost coating method, if issues with clustering can be resolved.

3. Deposition using energy methods (e-beam, laser ablation) pose problems for this type of phosphor. Many issues need to be resolved before these are viable techniques. Laser ablation damages the sensor with UV photons, and can vaporize the phosphor, rendering it inactive. The e-beam causes charge to build up in the phosphor, repelling the beam and preventing deposition.
4. The MATLAB coating simulation accurately predicted the trends (raising, lowering of QE, PRNU and CTF test results) that resulted from different coating parameters. The simulator loses accuracy if adjacent pixels have large differences in coating thickness.

9.2.1 Factors That Influence Final QE

The following factors were found to influence the QE of the sensors coated with inorganic phosphor in this research:

- Thickness of the coating and absorption coefficient. A thicker coating (and greater absorption coefficient) will allow more incident (UV) photons to be absorbed. The absorption coefficient is a measure of how many incident (UV) photons are absorbed in a given thickness of coating. It depends on the type of phosphor used, and the parameters of the deposition method. For a given coating thickness, there will be an absorption coefficient that yields a maximum QE. For a given coating absorption coefficient, there will be a thickness that yields a maximum QE. Making the coating thinner than the optimum thickness (or an absorption coefficient less than optimum) will allow more incident (UV) photons to penetrate the coating and be absorbed in the sensor's polysilicon gate material, lowering the QE. A coating thicker than the

optimum thickness (or absorption coefficient greater than the optimum) will allow more incident (UV) photons to be absorbed further from the sensor, increasing the distance they must travel (through the coating) to the sensor. Since the phosphor has 0% efficiency at visible wavelengths these photons will be lost, decreasing the QE.

- Contamination in the coating. Contamination will decrease the density of phosphor in the coating, causing fewer incident (UV) photons to be absorbed and re-emitted as visible photons.
- The absorption spectrum of the UV phosphor. The peak absorption of the phosphor should be well matched to the incident light, for maximum quantum efficiency.
- The efficiency for the down-conversion process. The internal efficiency of the phosphor is a limiting factor, however this is often 100%.
- The wavelength matching of the emission spectrum with the spectral response of the CCD. The QE will be higher is the peak emission is close to the maximum spectral response from the CCD.

9.2.2 Factors That Influence Final PRNU

The following factors were found to influence the PRNU of the sensors coated with inorganic phosphor in this research:

- Uniformity of coating thickness. The change in thickness over area of the coating directly influences the PRNU. Changes in the coating thickness across the sensor will increase the PRNU.
- Uniformity of phosphor in coating. If the coating is composed of phosphor and other impurities (such as a binder, or contaminant from the

coating method), there may be slight non-uniformities in the phosphor/impurity ratio from region to region.

- Thickness of the coating. With a thicker coating, more photons will be absorbed and re-emitted (isotropically) further from the surface of the sensor, so more spreading of the light will occur. As well the re-emitted photons travelling through the coating will tend to spread out, so a thicker coating will increase this effect. The spreading of light will reduce the effect of non-uniformities in coating thickness and phosphor density.
- Scattering coefficient of the coating. As explained above, incident (UV) photons and re-emitted (visible) photons spread out as they travel through the coating. The amount they spread out depends on the distance they must travel, and the scattering coefficient of the coating. For example, phosphor crystals with more angles and sharper edges will cause more scattering than round, smooth phosphor crystals. More spreading of the photons will decrease the PRNU.
- Absorption coefficient of the coating. A greater absorption coefficient will cause more incident (UV) photons to be absorbed further from the sensor. The isotropic emission and spreading due to scattering in the coating will cause the PRNU to decrease.

9.2.3 Factors that Influence Final CTF

The following factors were found to influence the CTF of the sensors coated with inorganic phosphor in this research:

- Thickness of the coating. There are two reasons a thicker coating gives a lower CTF. First, the phosphor re-emits photons isotropically. With a

thicker coating, more photons will be absorbed and re-emitted (isotropically) further from the surface of the sensor, so more spreading of the light will occur. Second, incident (UV) photons and re-emitted (visible) photons must travel through the phosphor coating, where they get scattered and spread out. More scattering occurs with a thicker coating. The more the light spreads out, the more the CTF will degrade.

- Scattering coefficient of the coating. As explained above, incident (UV) photons and re-emitted (visible) photons spread out as they travel through the coating. The amount they spread out depends on the distance they must travel, and the scattering coefficient of the coating. Increased spreading of the light yields lower CTF.
- Absorption coefficient of the coating. A greater absorption coefficient will cause more incident (UV) photons to be absorbed in the upper regions of the coating. The isotropic emission and spreading due to scattering in the coating will cause the CTF to degrade.
- Uniformity of thickness of the coating. Areas where the coating is thinner will allow re-emitted photons to travel to adjacent pixels with less attenuation. See Figure 57 for further explanation.

9.3 Recommendations for Further Research

Further work on the coating should focus on improving the present coating techniques. AST claims to have another coating technique that would allow a variable coating thickness. Sensors should be tested with this new coating. The

doctor-blade coating method should be improved by working on new techniques for slurry preparation, to reduce clustering of the phosphor.

The laser ablation coating method should be attempted again with different equipment. A more powerful excimer laser, with a shorter pulse, may ablate the phosphor without vaporizing it. Different types of phosphor could also be used. If the correct ambient gases were known, the phosphor could be vaporized and re-crystallized on the surface of the sensor, and still be active. As well, a method for protecting the sensor from scattered UV during deposition (such as a UV-blocking coating) should be examined.

The e-beam coating method would only be viable if the charge on the phosphor could be dissipated. Sending short, powerful e-beam pulses may be an option. Another option is mixing the phosphor with a material that would dissipate the charge.

Phosphor with a more uniform size distribution may yield a more uniform coating. At the time of this research, Osram Sylvania was experimenting with ways to produce phosphor with smaller size distributions.

The sensors should also be tested for UV degradation to properly characterise the lifetime. A 254nm UV laser would be necessary to properly examine the lifetime of the coated sensors.

The simulator predicts overly high PRNU values if adjacent pixels have large differences in coating thickness. Increasing the resolution of the simulation would help with these situations, although these type of coatings are not desirable so the usefulness would be limited. The simulation would be more accurate if the scattering and absorption coefficients were a function of wavelength. This would require calibrating the simulation to each wavelength, however.

10 Appendix A: MATLAB Code

The coating simulator was written in MATLAB v6.1. The main routine is coating_simulator.m, the other functions presented below (sa.m, absorbed.m, scattered.m) are subfunctions called by the main routine. The coating_simulator function is passed an incident light matrix, and a thickness matrix (must be the same size), and it outputs the light intensity at the surface of the sensor. Other parameters (pixel size, absorption/scattering coefficients, etc.) are set inside the function, but can easily be passed to the function is batch operation is needed.

10.1 Coating_Simulator.m

```
function [sensor] = coating_simulator(incident,thickness)

% ******************************************************
% *  Coating_Simulator.m : Inorganic Phosphor Coating   *
% *                        Simulator                    *
% * ---------------------------------------------------*
% *  Given:  incident: 256x256 matrix input light       *
% *          thickness: 256x256 coating thickness      *
% *                     matrix(in um)                  *
% *          absorption_coeff: Absorption coefficient  *
% *                            at Incident wavelength  *
% *          scattering_coeff: Scattering Coefficient  *
% *                            at Incident wavelength  *
% *          absorption_coeff_2: Absorption coefficient *
% *                              at emitted wavelength  *
% *          scattering_coeff_2: Scattering Coefficient *
% *                              at emitted wavelength  *
% *          pixel_size: Size of pixels (in um)        *
% *          phosphor_eff: QE of the phosphor          *
% *                                                    *
% *  Output: sensor: 256x256 matrix of light at sensor  *
% *                  surface                           *
% * ---------------------------------------------------*
% *  May 30/2002                      Stefan Alexander  *
% ******************************************************


[number_pixels,number_pixels]=size(incident);

phosphor_eff=0.95;
number_slices=100;  %Number of Slices to divide coating into
absorption_coeff=0.08;
scattering_coeff=0.001;
absorption_coeff_2=0.02;
```

```
scattering_coeff_2=0.02;
pixel_size=13;

sensor=zeros(number_pixels,number_pixels);  %Initialize output array

for x=1:number_pixels
    for y=1:number_pixels

        slice=thickness(x,y)/number_slices;  %The thickness of one slice (in um)

        for  z=number_slices:-1:1  %Steps  down  from  number_slices  to  1  in
        increments of -1

                height=z*slice;  %Height we're currently working at (in um)
                absorbed_1=absorbed(incident(x,y),slice,absorption_coeff);    %How
                    much %incident (UV) light is absorbed in one slice
                scattered_1=scattered(incident(x,y),slice,scattering_coeff);
                    %How much %incident (UV) light is scattered in one slice
                incident(x,y)=incident(x,y) - (absorbed_1 + scattered_1);  %Lower
                    the %light at the pixel due to absorption and scattering
                emitted=absorbed_1*phosphor_eff;    %How  much  UV  light  is  re-
                    emitted %(isotropically) by the phosphor as visible light

                x1_low=x-1;                             %  Set up
                x1_low=max(1,x1_low);                   %  boundaries
                x1_high=x+1;                            %  for next
                x1_high=min(number_pixels,x1_high);     %  "FOR" loop

                y1_low=y-1;                             %  Set up
                y1_low=max(1,y1_low);                   %  boundaries
                y1_high=y+1;                            %  for next
                y1_high=min(number_pixels,y1_high);     %  "FOR" loop

                for x1=x1_low:x1_high
                       for y1=y1_low:y1_high

                           sa_correction=sa(x,y,x1,y1,height,pixel_size);     %find
                              out solid %angle correction for the given pixel
                           emitted_2=emitted*sa_correction;   %how much re-emitted
                              light is %on its way to the given pixel
                           distance    =    sqrt(((x1-x)*pixel_size)^2    +    ((y1-
                              y)*pixel_size)^2 +… (height)^2);  %find out distance
                              from emission point to given %pixel
                           absorbed_2=absorbed(emitted_2,distance,absorption_coeff
                              _2);  %Re-%emitted light absorbed on the way to the
                              pixel
                           scattered_2=scattered(emitted_2,distance,scattering_coe
                              ff_2);   %Re-emitted  light  scattered  on  the  way  to
                              the pixel
                           arrived=emitted_2   -   (absorbed_2   +   scattered_2);
                              %Subtracting %the absorbed and scattered light
                           sensor(x1,y1)=sensor(x1,y1)  +  arrived;    %Adding  the
                              arrived %light into the sensor array

                      end
                end
        end

        sensor(x,y)=sensor(x,y)+0.05*incident(x,y);  %5 percent of any UV photons
        that %make it through the coating get into the sensor

    end
end
```

10.2 sa.m

```
function [sa] = sa(x,y,x1,y1,height,pixel_size)

% ******************************************************
% *  Given:  x,y: Coordinates of the emission point     *
% *          x1,y1: Coordinates of the pixel that the   *
% *                 is to be calculated for             *
% *          height: height of the emission point off   *
% *                  the sensor (in um)                 *
% *          pixel_size: Length of one side of a pixel  *
% *                      (assuming square pixels)       *

% *                                                     *
% *  Output: sa: The solid angle correction for the     *
% *              given pixel                            *
% * ----------------------------------------------------*
% *    Calculates the solid angle correction for a      *
% *    given pixel                                      *
% * ----------------------------------------------------*
% *  May 30/2002                      Stefan Alexander  *
% ******************************************************

theta_1=atan((0.5*pixel_size)/height);
theta_2=atan((pixel_size)/height) - theta_1;
theta_3=atan((1.5*pixel_size)/height) - (theta_1+theta_2);
theta_4=atan((2*pixel_size)/height) - (theta_1+theta_2+theta_3);


if (x==x1 & y==y1)
    sa=(2*theta_1)/(2*pi);  %Pixel type 1
elseif (x==x1 | y==y1)
    sa=(theta_2 + theta_3)/(2*pi);  %Pixel type 2
else
    sa=(theta_3 + theta_4)/(2*pi);  %Pixel type 3
end
```

10.3 scattered.m

```
function [scatt] = scattered(incident,thickness,scattering_coeff)


% ******************************************************
% *  Given:  incident: Incident Intensity of light      *
% *                    (Must be a single wavelength)    *
% *          thickness: Distance that light must go     *
% *                     through (in um)                 *
% *          scattering_coeff: Scattering coefficient   *
% *                            for given wavelength     *

% *                                                     *
% *  Output: I_t: Intensity after travelling through    *
% *               the given depth                       *
% * ----------------------------------------------------*
% *    Calculates the amount of light lost to scattering*
% *    while travelling through a medium                *
% * ----------------------------------------------------*
% *  May 30/2002                      Stefan Alexander  *
% ******************************************************
```

```
I_t = incident*exp(-scattering_coeff*thickness);
scatt=incident-I_t;
```

10.4 absorbed.m

```
function [absor] = absorbed(incident,thickness,absorption_coeff)

% ******************************************************
% *  Given:  incident: Incident Intensity of light      *
% *                    (Must be a single wavelength)    *
% *          thickness: Distance that light must go     *
% *                     through (in um)                 *
% *          absorption_coeff: Absorption coefficient   *
% *                            for given wavelength     *
% *                                                     *
% *  Output: I_t: Intensity after travelling through    *
% *               the given depth                       *
% * ----------------------------------------------------*
% *    Calculates the amount of light lost to absorption*
% *    while travelling through a medium                *
% * ----------------------------------------------------*
% *  May 30/2002                      Stefan Alexander  *
% ******************************************************
I_t=(incident)*(exp((-absorption_coeff)*thickness));
absor=incident-I_t;
```

11 References

[1] W.A.R. Franks, M. J. Kiik and A. Nathan, Proc. SPIE, vol. 3965, pp. 33-41 (2000).

[2] W.A.R. Franks, "Inorganic Phosphor Coatings for Ultraviolet Responsive Image Detectors", MASc Thesis, University of Waterloo, Canada, 2000.

[3] X.L. Mao, A.C. Ciocan, O.V. Borisov, R.E. Russo, "Laser ablation processes investigated using inductively coupled plasma-atomic emission spectroscopy", *Applied Surface Science*, 127-129 (1998) 262-268.

[4] Y. E. Lee, D. P. Norton, J. D. Budal, C. M. Rouleau, J. Park, "Epitaxial Growth and Luminescent Properties of Mn^{2+}-Activated $ZnGa_2O_4$ Films", *Journal of Electroceramics*, 4:2/3, 293-297, 2000.

[5] R. E. Russo, X. Mao, O. V. Borisov, "Laser Ablation Sampling", *Trends in Analytical Chemistry*, vol. 17, nos. 8+9, 1998.

[6] I. Koiwa and H. Sawai, "A Study of Binders for the Thick-Film Cathodes of DC-Type Plasma Display Panels", *IEEE Transactions of Electron Devices*, Vol. 41 No. 9, September 1994.

[7] G. Corso, S. L. Casto, A. Lombardo, S. Freni, "The influence of the tape-casting process parameters on the geometric characteristics of SiC tapes", *Materials Chemistry and Physics* 56 (1998) 125-133.

[8] Y. Lee, J. Park, "Reactions of (La,Ca)CrO_3 sealants in yttria-stabilized zirconia-(La,Ca)CrO_3 planar solid oxide fuel cell (SOFC) stacks", *Materials Chemistry and Physics* 45 (1996) 97-102.

[9] J. Cho, R. Kim, K. Lee, C. Son, "Low-voltage characteristics of MgO-CaO films as a protective layer for AC plasma display panels by e-beam evaporation", *Journal of Materials Science* 34 (1999) 5055-5059.

[10] M. H. M. Reddy, A.N. Chandorkar, "E-beam deposited SnO2, Pt-SnO2 and Pd-SnO_2 thin films for LPG detection", *Thin Solid Films* 349 (1999) 260-265.

[11] W. Park, K. Yasuda, B.K. Wagner, C.J. Sumers, Y.R. Do, H.G. Yang, "Uniform and continuous Y_2O_3 coating on ZnS phosphors", *Materials Science and Engineering* B76 (2000) 122-126.

[12] A.R. Faruqui, G.C. Tyrell, "Evaluation of gadolinium oxy-sulphide (P43) phosphor used in CCD detectors for electron microscopy", *Ultramicroscopy* 76 (1999) 69-75.

[13] J. M. Fitz-Gerald, A. Pique, and D. B. Chrisey, "Laser Direct Writing of phosphor screens for high-definition displays", *Applied Physics Letters,* Volume 76 Number 11.

[14] C. H. Seager, D. R. Tallant, and W. L. Warren, "Cathodoluminescence, reflectivity changes, and accumulation of graphite carbon during

electron beam aging of phosphors", *Journal of Applied Physics*, Volume 82 Issue 9, November 1997.

[15] R. Reitano, P. Baeri, N. Marino, "Excimer Laser induced thermal evaporation and ablation of silicon carbide", *Applied Surface Science* 96-98 (1996) 302-308.

[16] Smith, Donald L., "Thin-film deposition", McGraw-Hill Inc., USA, 1995.

[17] Katz, Murarka, Appelbaum, "Advanced Metallizations in Microelectronics", *Materials Research Society*, USA, 1990.

[18] S.M. Sze, "VLSI Technology", McGraw-Hill, USA, 1988.

[19] Metachrome II Datasheet, Roper Scientific.

[20] S.M Sze, C.Y. Chang, "ULSI Technology", McGraw-Hill, Singapore, 1996.

[21] University of Toronto Web Site: http://www.cs.toronto.edu/~roweis/notes/gaussid.pdf, Accessed on May 04, 2002.

[22] Private Discussions with Charles Chenot, PhD, Osram Sylvania.

[23] ACEPT Web Site: http://acept.la.asu.edu/PiN/rdg/visnxray/visnxray.shtml, Accessed on May 22, 2002.

[24] M. H. M. Reddy, A.N. Chandorkar, "E-beam deposited SnO_2, Pt-SnO_2 and Pd-SnO_2 thin films for LPG detection", *Thin Solid Films* 349 (1999) 260-265.

[25] Private Communication with Martin Kiik.

[26] M.P. Lesser. "Recent charge-coupled devices operation results at steward observatory", *SPIE*, 1242:164 – 169, 1990.

[27] M.P. Lesser. "CCD thinning, coating, and mounting research for astronomy", *Proceedings of CCDs in Astronomy*, 8:36 – 75, 1989.

[28] E. Meisanzahl et. al. "3.2 million pixel full-frame true 2-phase ccd image sensor incorporating transparent gate technology", *SPIE*, 3965-A:164 – 169, 2000.

[29] Kodak web site: www.kodak.com/go/ccd.

[30] Private communications by Wendy Franks with design engineers from Kodak while at the APIE/IS&T Imaging 2000 conference.

[31] W. Viehmann et. al. "Thin-film scintillators for extended untraviolet response silicon detectors", *Proc. SPIE*, 196:90 – 95, 1979.

[32] M. Cullum et al. "Spectroscopy to the atmospheric transmission limit with a coated gec ccd", *Astronomy and Astrophysics*, 153:L1-L3, 1985.

[33] L. B. Robioson et al. "Characteristics of large ford and reticon ccds", *SPIE*, 1235:315-326, 1990.

[34] G. Fabiola G. R. Sims. "Improvements in ccd quantum efficiency in the uv and near-ir", *SPIE*, 1071:31-42, 1989.

[35] M.M. Blouke et al. "Ultraviolet downconverting phosphor for use with silicon ccd imagers", *Applied Optics*, 19:3318-3321, 1980.

[36] R. A. Bredthauer et al. "Recent ccd technology developments", In L. B. Robinson, editor, *Instrumentation for Ground-Based Optical Astronomy*. Springer-Verlag, New York, 1987.

[37] Albert Theuwissen. "Solid-State Imaging with Charged-Coupled Devices", Kluwer Academic Publishers, Boston, 1991.

[38] SPIE's International Symposium on Intelligent Systems and Advanced Manufacturing. "MTF, CSF, and SQRI for Image Quality Analysis", 1995.

[39] H. L. Burrus. "Lamp Phosphors", Mills and Boon Ltd., London, 1972.

[40] Osram Sylvania, "Technical Information Bulletin for Type 2212 Phosphor Luminescent Material"

[41] Osram Sylvania, “Technical Information Bulletin for Type 2345 Phosphor Luminescent Material”